Resonanz Raman Mikro-Spektroskopie zur Analyse bakterieller Biofilme

Resonance Raman Micro-Spectroscopy for Analyzing Bacterial Biofilms

Von der Fakultät für Mathematik und Physik
der Gottfried Wilhelm Leibniz Universität Hannover
zur Erlangung des Grades
Doktorin der Naturwissenschaften
Dr. rer. nat.

genehmigte Dissertation von
Dipl.-Phys. Ann-Kathrin Kniggendorf
geboren am 27. 01.1972 in Hannover

(2011)

Referent: Prof. Dr. Uwe Morgner
Institut für Quantenoptik, Gottfried Wilhelm Leibniz Universität Hannover

Korreferent: Prof. Dr. Alexander Heisterkamp
Laser Zentrum Hannover e.V.

Tag der Promotion: 28. 6. 2011

Zusammenfassung

Dieses Dissertationsprojekt untersucht die Eignung konfokaler Resonanz-Raman Mikro-Spektroskopie zur schnellen, nicht-invasiven Analyse komplexer nativer Biofilme in wässrigem Milieu. Inspiriert durch die enorme Vielfalt dieser unschätzbaren natürlichen Resource, wird ein schnelles, zerstörungsfreies Abbildungsverfahren auf Resonanz Raman Basis entwickelt, dass nicht nur Information über Aufbau und Morphologie von Biofilmen als Gesamtheit liefert, sondern auch Aufschluss gibt über die in ihnen vergesellschafteten Spezies inklusive räumlicher Verteilung, Verwandschaftsbeziehungen und Identifizierung (Spezies und Stamm). Konfokale Raman Mikro-Spektroskopie verbindet die hohe räumliche Auflösung konfokaler Mikroskopie mit der Spezifizität von Raman Fingerprints. Durch die gezielte Anregung molekularer Resonanzen in allgegenwärtigen, aber dennoch spezies-spezifischen Chromophoren – insbesondere den Zytochrom-c – konnten die notwendigen Messzeiten von 100 s und mehr bei Normal Raman Spektroskopie auf 0,5 s (0,1 s bei Karotinoiden) gesenkt werden. Durch die gezielte Auswahl von Resonanzen wird gleichzeitig die in den Spektren kodierte Information auf solche über Moleküle mit bekannter Funktion und taxonomischer Relevanz in den anvisierten Bakterien konzentriert. Das ultimative Ziel dieses Dissertationsprojektes war die Etablierung dieses vielversprechenden Abbildungsverfahrens zur schnellen, zerstörungsfreien Analyse unbekannter Biofilmproben und die Bereitstellung präziser Handlungsanweisungen für seine Anwendung. Diese Ziele wurden erreicht. Es wird gezeigt, dass konfokale Resonanz-Raman Mikro-Spektroskopie, wie in dieser Dissertation vorgestellt, die nicht-invasive, optische Analyse lebender Biofilme von bis zu 80 μm Dicke in wässrigem Milieu ermöglicht, ohne dass die Probe dazu fixiert oder anderweitig präpariert werden muss. Bei solchen in situ Messungen wurden eine räumliche Auflösung in der Dimension einer Zelle in Verbindung mit Messzeiten zwischen 0,1 und 0,5 s je Spektrum erreicht. Da Ramanspektren im Nachhinein analysiert werden können, ist die Untersuchung auch völlig unbekannter Proben ohne a priori Annahmen grundsätzlich möglich. Desweiteren wird gezeigt, dass konfokale Resonanz-Raman Mikro-Spektroskopie nicht nur die Untersuchung biologischer Biofilmkomponenten gestattet, sondern dabei auch mineralische Komponenten erfasst werden. Extrazelluläre polymerische Sustanzen zeigen sich in der Ramananalyse als unspezifische Masse geringer Dichte. Der autofluoreszente Untergrund in den meisten, in Biofilmen aufgenommenen Spektren, ermöglicht über Breitbandfilter das Auffinden von Bakterien mit unbekannten Ramanspektren. Dies verhindert „false negatives“ wie sie häufig in der Bewertung mikrobiologischer Standardverfahren problematisiert werden und gewährt Einblicke in die Morphologie des Biofilms, selbst in dem seltenen Fall, dass keine Chromophore in der Messung erfasst worden sind. Weitere Experimente zeigten eine zum Teil gute Kompatibilität des Verfahrens mit „weichen Fixierungen“, wie sie für die Lagerung oder den Transport von Proben in einem definierten Zustand erforderlich sind. Die meisten mikrobiologischen Standardverfahren zur Biofilmanalyse beruhen auf dem Einsatz von fluoreszenten Markern und sind daher nicht mit konfokaler Resonanz-Raman Mikro-Spektroskopie kompatibel.

Schlüsselbegriffe: Resonanz Raman, konfokale Mikroskopie, Biofilm

Abstract

Motivated by the enormous complexity of biofilms and their amazing potential as an invaluable natural resource, this work examines the properties and feasibility of confocal resonance Raman micro-spectroscopy for the analysis of complex bacteria samples such as multi-species biofilms, beginning with pure cultures of known properties and ending with the analysis of biofilm samples from two fully characterized lab-scale sequencing batch reactors (SBR) for wastewater treatment.
Confocal Raman micro-spectroscopy combines the high spatial resolution of confocal microscopy with the specificity of Raman spectra. In employing molecular resonances of ubiquitous but specific chromophores, most notably cytochromes-c, the required measurement times are severely reduced in comparison to normal Raman spectroscopy (from 100 seconds and more down to 0.5 seconds (0.1 s in case of carotenoid chromophores)) and the spectral information is focused to molecules with known presence and function in the bacteria.
The aim of this work was to establish this promising technique as a fast, non-destructive imaging technique for blind measurements of microbial biofilms and to provide precise procedures for its application. This was accomplished:

It is shown that confocal resonance Raman micro-spectroscopy, as established in this work, allows the non-invasive optical analysis of living, undisturbed wet biofilms of up to 80 μm thickness, without requiring sample fixation or treatment with fluorescent probes, labels or stains. A spatial resolution at cell size is combined with excitation times between 0.1 and 0.5 s for a single spectrum. Since Raman spectra – and therefore the chromophores – can be identified after the measurement is completed, measuring fully unknown samples (blind measurements) is possible.
It is shown that confocal resonance Raman micro-spectroscopy does allow the analysis of biological as well as mineral components of the sample in the same measurement. Extracellular polymeric substance (EPS) is detected as unspecific „low density matter“. The autofluorescent background, seen in most spectra recorded from biofilms, is analyzed with broadband filters, allowing the discrimination of bacteria with unknown Raman spectra, thus preventing false negatives. Background analysis provides information about biofilm morphology even in the absence of resonant Raman chromophores.
Further experiments showed that this technique is partially compatible with soft fixation methods, required for storage or transport of samples in a known condition. However, it is incompatible with most standard techniques for biofilm analysis, which require fluorescent markers.

Keywords: resonance Raman, confocal microscopy, biofilm

Contents

Zusammenfassung iii

Abstract v

Introduction 1

0.1 Microbial Biofilms - the power of association 1

0.2 Biofilm Analysis – State of the Art 2

0.3 Biofilm Analysis in this Work 3

1 Basic Concepts 5

1.1 Raman scatterings 5

1.2 Confocal Microscopy 7

2 Materials and Methods 9

2.1 Confocal Resonance Raman Microscopy 9

2.1.1 Equipment 9

2.1.2 Data acquisition and measurement modes 13

2.2 Spectral Images: Spatially resolved Raman data 14

2.2.1 Software: WITec Project 14

2.2.2 Background Subtraction 14

2.2.3 Peak Analysis routines 15

2.2.4 Filtered Images 16

2.3 Analysis of individual Raman spectra 16

2.3.1 Software: OPUS 16

2.3.2 Raman Line Search and Comparative Spectrum Analysis 17

2.3.3 Spectrum Comparison 17
2.3.4 Hierarchical Cluster Analysis 18
2.4 Absorption spectroscopy 19
2.5 Biological materials and procedures 19
2.5.1 Biofilm granules 20
2.5.2 Bacteria cultures 21
2.5.3 Fixation 23

3 Resonance Raman spectra of bacteria 25

3.1 Properties of Raman spectra recorded from native samples 25
3.1.1 Description 26
3.1.2 Critical: spectrum quality 27
3.2 Characterization of native bacteria 27
3.2.1 Bacterial Reference spectra 28
3.2.2 Purple non-sulfur bacteria: carotenoids and cytochromes 29
3.2.3 *Nitrosomonae*: cytochrome-c 33
3.2.4 Bacteria fact sheet 37
3.3 Effects of Sample Preparation 38
3.3.1 Effects of Fixation 38
3.3.2 Effects of adhesive coatings 41

4 Spectral analysis with chromophore information 45

4.1 HCA algorithm assessment 45
4.1.1 Data preparation and test procedures 46
4.1.2 Reference spectra clustering 47
4.1.3 Single spectra clustering 50
4.2 Effects of spectrum quality on HCA 54
4.2.1 Test for spectrum quality influences 55
4.3 Native variability and spectral similarity 56
4.4 Manual for Spectrum Comparison and HCA 59

5 Mapping the biofilm: spatially resolved information 61
5.1 Spectral Imaging: Biofilm Filters 61
5.1.1 Broadband image filters 62
5.1.2 Fingerprint image filters 63
5.2 The acid test: analyzing microbial aggregates 64
5.2.1 Chromophore identification 64
5.2.2 Spatially resolved information: structure and content 66
5.2.3 Bacterial Tracking – who stays? 71
5.2.4 Bacterial Identification – who's who? 73
Conclusion and Outlook 75
List of Figures 79
Bibliography 83
Curriculum Vitae 91
Publications and Presentations 93

Introduction

0.1 Microbial Biofilms - the power of association

Biofilms are one of the most fascinating forms of microbial life on Earth (and probably elsewhere [Tung et al., 2005]) for at least 3.46 billion years [Virginia Museum of Natural History, 2008]. These dense, highly structured microbial communities form on almost every non-sterile humid interface and as self-carrying granules in aqueous liquid. Biofilms have distinctly different properties than individual species associated in them, allowing them to survive and even thrive under extreme conditions few unassociated species can handle on their own [Hall-Stoodley et al., 2004].
Bacteria associated in **biofilms may cause significant problems**, ranging from biocorrosion even of metals [Beech and Sunner, 2004], hydrogen sulfite pollution of raffined natural gas and oil [Schwermer et al., 2008], to medical emergencies arising from pathogenic biofilms with an unusual high tolerance to antibiotics and immune system responses [Drenkard and Ausubel, 2002, Jesaitis et al., 2003].
On the other hand, **biofilms are an invaluable natural resource** capable of performing extraordinary tasks such as the secure biological degradation of highly toxic chemicals and the removal of phosphate, nitrite, and ammonium from municipal and agricultural wastewater [Wuertz et al., 2004, Bitton, 2011].

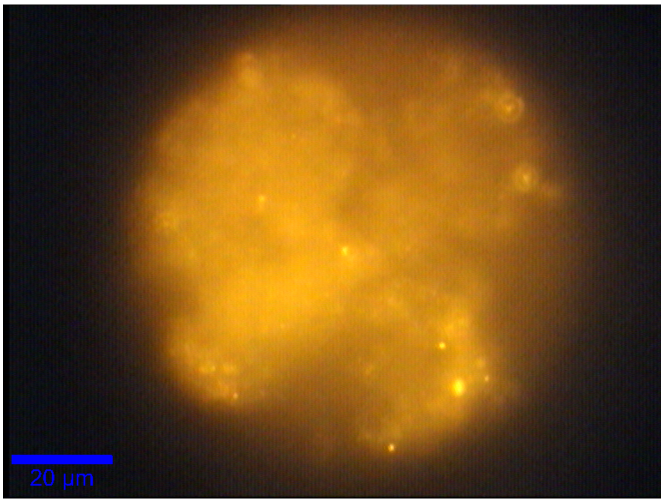

Figure 0.1: Surface of an anaerob ammonium oxidizing (ANAMMOX) biofilm granule. Light microscopic image taken with the CRM 200 (white light illumination; Nikon CFI Fluor water-immersion objective).

Biofilms are ubiquitous – one may say, almost unavoidable – and we have to address

the problems they create and should harness their useful abilities. For this, an indepth understanding of these complex and highly diverse microbial communities is essential.
However, **biofilms** in all their complexity **are challenging subjects for research**. They are formed of dense, highly hydrated, highly structured clusters of bacterial cells – so called microcolonies – bound together by extracellular polymeric substances (EPS; or „slime“). These microcolonies may differ in bacterial species or phenotype of the bacterial species clustered together, either with direct interfaces to other microcolonies or separated by channels filled with bulk water or EPS.
In addition, the majority of the bacteria – associated in biofilms or not – cannot be grown in a pure culture, deferring most standard techniques for bacterial identification [Amann et al., 1995]. Even those species for which pure cultivation is possible, often show distinctly different phenotypic traits in a biofilm than seen in their planctonic culture. Bacteria associating in a biofilm may undergo significant phenotypic changes, including the loss of motility organelles such as flagella and alterations in the production of polysaccharides leading to the formation of EPS, which is believed to be a crucial intermediate interface between the bacteria in a biofilm [Steward and Franklin, 2008, Flemming, 2010]. In fact, bacteria may undergo several such changes in phenotype during biofilm formation: Sauer et al. [2002] reported severe changes in the protein composition during formation and maturation of a mono-species biofilm of *Pseudomonas aeruginosa*.

0.2 Biofilm Analysis – State of the Art

The technique most widely used for obtaining spatially resolved information on the bacteria associated in biofilms, is **fluorescent in situ hybridization (FISH)**. In general, FISH analysis returns the distribution of specific DNA or RNA sequences in the sample via gene probes tagged with fluorescent dyes. These FISH probes can be made specific for a bacterial strain, a species, or a whole phylum, depending on the specificity of the gene sequence targeted [Manz et al., 1992, Jin and Lloyd, 1997]. These gene sequences for probes can be obtained either from cultured bacteria or via proteomic or metagenomic approaches working on the protein or gene composition of a biofilm as a whole even from uncultured bacteria [Santos Pontes et al., 2007]. However, the number of probes that can be applied in a single FISH analysis is limited by the number of distinguishable fluorescent dyes available. In addition, FISH **requires rigorous and destructive preparation** of the sample, including fixation with ethanol and/or paraformaldehyde solution [Jin and Lloyd, 1997], making it a strict end-point analysis in all its variations [Neu et al., 2010]. Therefore, the results of a FISH analysis are **dependent on prior knowledge** of – or educated expectations about – the sample regarding the gene sequences for which to probe. Unexpected components may well be missed. In addition, FISH does not return information on non-biological components such as microparticles that may well be present in the sample.

Clearly, a **non-destructive imaging** technique providing information on spatial structure and distribution of – as well as tracking and identification capabilities for – the microorganisms associated in biofilms, would be preferable for understanding these complex microbial communities.

Raman micro-spectroscopy – successfully used for the in vivo mapping of biofilms as well as identification and taxonomy of bacteria – is among the most promising techniques proposed for these tasks [Harz et al., 2008]. However, it suffers from long measurement times and a high sensitivity to environmental (or culture) conditions, making it difficult to apply on extended segments of biofilm and bacteria in various habitats. To overcome these limitations, Raman micro-spectroscopy has been **combined with several other methods**, such as confocal laser scanning microscopy (CLSM) [Wagner et al., 2009], environmental scanning electron microscopy (ESEM) [Schwartz et al., 2009], and even FISH (on cells labeled with ^{13}C) [Huang et al., 2007]. However, for doing so most – if not all – of the advantages of Raman micro-spectroscopy in regard of non-invasive measurements of native, undisturbed samples had to be traded.

0.3 Biofilm Analysis in this Work

The **ideal technique for biofilm analysis** should be fast, non-invasive (preparation-free; no labeling or tagging required), functional on native as well as fixed samples (to allow for transport and the use of stored samples), independent of prior knowledge (allowing for blind measurements of unknown samples), and allow for indepth analysis of the data after the measurements are completed. It should provide information on spatial structure and morphology of the biofilm and the bacteria associated in it, including their distribution, relative positions, phenotypes and identification as well as taxonomy (at least as far as bacterial taxonomy has been agreed upon [Staley, 2006]) and activity. Additional information on EPS and other, not necessarily biological components would be useful.

Raman micro-spectroscopy, save for its long measurement times and the sensitivity towards environmental (or culture) conditions, is still the technique matching most of these listed items. By employing molecular **resonances of chromophores intrinsic to most bacteria**, it is possible to overcome its limitations and achieve an in-depth analysis of the targeted microbial communities solely with this powerful technique.

This work examines the properties and feasibility of confocal resonance Raman micro-spectroscopy for the analysis of complex bacteria samples such as multi-species biofilms, beginning with pure cultures of known properties and ending with the analysis of biofilm samples from two fully characterized lab-scale sequencing batch reactors (SBR) for wastewater treatment.
The main target chromophore is cytochrome-c, a ubiquitous heme protein in the electron transport chain of prokaryotes and eucaryotes alike. Its gene sequences have been used for taxonomy of higher animals as well as bacteria [Moore and Pettigrew, 1990]. It is easily available in pure form from many different sources, water-soluble, and therefore very popular for testing spectroscopic techniques. The central heme molecule allows resonant excitation with 532 nm light from a frequency-doubled Nd:YAG laser [Scott and

Mauk, 1996]. Additional chromophores found for this wavelength are carotenoids of the spheroidene pathway (neurosporene, spheroidene, spirilloxanthin) and the cytochrome-cbb$_3$ complex seen in purple bacteria. These were analyzed as well.
The omnipresent autofluorescent background seen in biofilms at visible excitation wavelengths returns structural and morphological information even in the rare case of absent chromophores and is used in the spatially resolved measurements to prevent false negatives. In the presence of chromophores, information about structure, water content, bacteria (tracking, identification, and distribution), and non-biological components such as mineral microparticles is accessible on the scale of single cells (approx. 1 μm^3).

After a brief presentation of the main concepts (chapter 1) and the technical requirements (chapter 2), the question of whether or not the often stated claim that „fixation does not alter the Raman spectroscopic information from bacteria samples“ holds true (3.3) is answered in chapter 3, after defining and analyzing the general properties of bacterial Raman spectra (3.1 and 3.2).
Chapter 4 addresses the natural variability in bacterial Raman spectra and the significance of spectral distance as a means for identifying bacterial relationships based on resonance Raman spectra (4.3). This chapter also includes a performance analysis of the eight most common algorithms for hierarchical cluster analysis of bacterial (resonance) Raman spectra (4.1 and 4.2), falsifying even a claim in the manual of the standard software for spectroscopical analysis („Ward's Algorithm [...] eignet sich besonders zur Clusteranalyse von Bakterienspektren.“[1] [Bruker GmbH, 2004]).
In chapter 5 the procedures for displaying spatially resolved information are developed (5.1) and put to the test with the analysis of the outer layers of biofilm granules sampled from two identical SBRs, one with nominal anammox activity [Wesoly, 2009] and one showing a significant infestation with purple bacteria (5.2). The chapter closes with a comparison of how confocal resonance Raman micro-spectroscopy compares with other techniques recently proposed for non-invasive biofilm analysis (5.2.4).

Parts of this work have been previously published in Kniggendorf et al. [2011a], [Kniggendorf et al., 2011b] and Kniggendorf and Meinhardt-Wollweber [accepted for publication w.m.r.].

---

[1] Translation: „Ward's algorithm is especially suited for the cluster analysis of bacterial spectra.“

1 Basic Concepts

This chapter gives a concise overview about the basic concepts behind this work. For further information please refer to the standard literature given at the end of each section.

1.1 Raman scatterings

The **Raman effect** is an inelastic light-scattering process, experimentally observed by Sir Chandrasekhara Venkata Raman in 1928 [Long, 2002]. Raman scattering differs distinctly from fluorescence, which also returns frequency-shifted light, therein that no real excited state of the scattering molecule is involved (see Fig. 1.1 for an illustration of the differences between Raman scattering and fluorescence).

(Raman) scattering can be understood as follows: the electron cloud of a molecule is driven with the frequency ν_0 of an incident electromagnetic field (for example, the light of an excitation laser). This causes a displacement of the electron charge, resulting in an oscillating dipole moment, and – since the charge is accelerated – the emission of electromagnetic radiation of the same frequency (ν_0). This is **elastic scattering**, called Rayleigh scattering if the scatterer is small compared to the incident wavelength (such as atoms or molecules).

However, the induced oscillating dipole moment may be modulated by the dynamics of the scatterer: If a nuclear vibration induces an additional oscillation of frequency ν_v in the electron cloud, this vibrational oscillation will couple to the oscillation of frequency ν_0 caused by the incident light, giving rise to beat oscillations and the emission of (Raman) light of the sum and difference frequencies ($\nu_o \pm \nu_v$). This is **Raman scattering**, or – more precisely – **Stokes** Raman scattering in case of the difference frequency $\nu_o - \nu_v$ and **Anti-Stokes** Raman scattering in case of the sum frequency $\nu_o + \nu_v$. The corresponding energy-level diagrams are given in Fig. 1.1.

If the frequency of the incident light is close to a a natural vibration frequency of the electron cloud, the resulting oscillating charge displacement – and thus the induced dipole moment – becomes considerably larger. Therefore, a significantly higher percentage of the incident light is scattered inelastically into the beat frequencies. This is **resonance Raman scattering** (see Fig. 1.1 for an energy-level diagram of the process), which may increase the quantum yield of normal Raman scattering up to a factor of 10^8, comparable to that of fluorescence [Asher, 1993a].

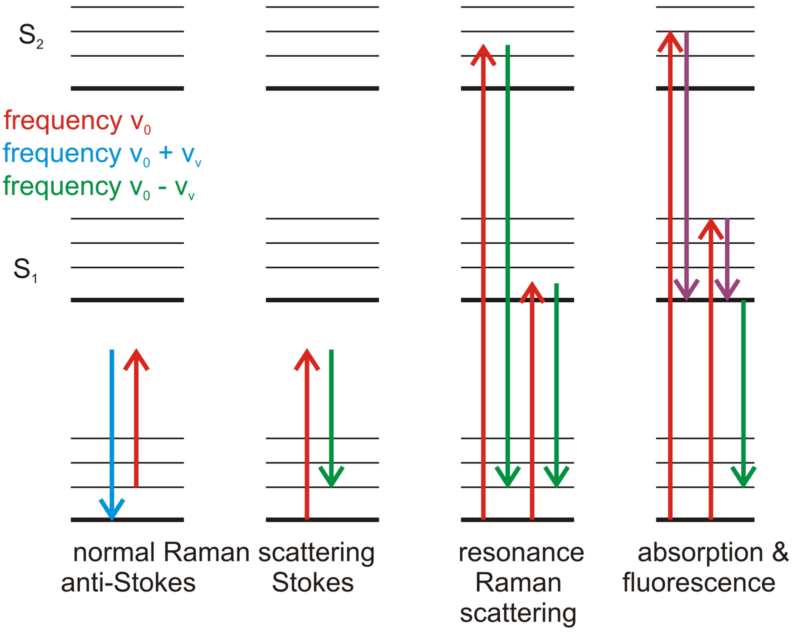

Figure 1.1: Energy-level diagrams of inelastic light scattering with positive frequency shift $\nu_0 \Rightarrow \nu_0 + \nu_v$ (Normal Raman (anti-Stokes)), inelastic scattering with negative frequency shift $\nu_0 \Rightarrow \nu_0 - \nu_v$ (Normal Raman (Stokes)), inelastic scattering with frequency shift $\nu_0 \Rightarrow \nu_0 - \nu_v$ and excitation within an electronic transition (Resonance Raman), and the non-scattering event of absorption with emission-free relaxation to the lowest vibrational level of the exited state (S_1) and subsequent emission of fluorescence. Ground state and two excited states (S_1 and S_2) are shown. Excitation is red, emission with positive (negative) frequency shift is blue (green), emission-free relaxation is purple.

For a specific excitation frequency, the **Raman line intensities** depend on the Raman polarizability $\alpha_R = (\partial_Q \alpha)_0 Q$ of the scatterer, which is associated with the Raman active vibration Q perturbing the static polarizability α. Most notably, for a Raman shift to occur, non-vanishing α and $\partial_Q \alpha$ are required.

Raman spectroscopy provides information about the structure and dynamics of the irradiated molecules by measuring the magnitudes and intensities of frequency shifts, ultimately illuminating the chemical composition of the scattering molecules.

In addition, **Resonance Raman spectroscopy**, specifically exciting natural vibration frequencies (absorption bands) of its target molecules (chromophores) is highly selective, since different absorption bands may derive from different components in the sample or even different chromophoric elements in the same macromolecule that can be studied independently. The selectivity is of the same order of magnitude as the increase in quantum yield due to the resonance.

Of course, this is only a very simplified description of the underlying principles in disregard of the complexity of the molecular response, which often involves multiple interacting modes. For a precise theoretical treatment of Raman scattering by molecules see Long [2002].

1.2 Confocal Microscopy

Confocal microscopy was developed in the 1950s to solve the issue of intense, unfocused background in wide-field fluorescence microscopy (International patent G02B21/00 by Marvin Minsky, 1961). Instead of illuminating the whole sample at once, a point light source is focused onto a sample with an objective. The illuminated spot is then focused via the same objective onto a pinhole before entering the detector. For a schematic view of a confocal microscope, see Fig. 2.2 in Chap. 2.

The wavelength of the illumination and the image formation of the microscope determine the size of the illuminated spot on the sample. The diameter of the pinhole is chosen so that only the light from the measurement volume (the focus spot within the focal plane) can reach the detector. A small diameter of the pinhole increases the contrast, because more light from adjacent areas of the sample is suppressed. However, a smaller pinhole admits also less light to the detector, decreasing effective quantum yield. Therefore, the size of the pinhole is a compromise between contrast improvement and detected intensity of the scattered light.

As a rastering technique, confocal microscopy creates two- and three-dimensional images by subsequent single measurements, which are then combined into an image with a defined resolution depending on the measurement settings and the spatial resolution of the system.

The determination of the spatial resolution is not trivial and depends on the optical components as well as the refraction properties of the sample. The system used in this work (compare 2.1.1) had a pinhole diameter of 50 μm. Therefore, the lateral resolution r_z can be calculated with the Rayleigh criterion:

$$r_z = \frac{0.61\lambda}{\text{NA}} \tag{1.1}$$

with NA being the numerical aperture of the objective and λ the wavelength of the illumination. The axial resolution r_{xy} is actually dependent on the refractive index n_s of the sample and given by

$$r_{xy} = \frac{1.4\lambda n_s}{\text{NA}^2} \tag{1.2}$$

Since the refractive index of bacteria and biofilms are not readily available, the axial resolution r_{xy} was calculated with the refractive index of water ($n_w \approx 1.33$).

For more information on confocal microscopy see Wilson [1990] and Pawley [2006].

2 Materials and Methods

Parts of this chapter were previously published in Kniggendorf et al. [2011a], Kniggendorf et al. [2011b], and Kniggendorf and Meinhardt-Wollweber [accepted for publication w.m.r.].

2.1 Confocal Resonance Raman Microscopy

Confocal Raman microscopy was established at the Institute of Biophysics as part of a project for the analysis of native anammox biofilm samples (DFG grant no. AN 712/5-1 „In situ Identifikation und Aktivitätsmessung von mikrobiellen Aggregaten in der biologischen Abwasserreinigung durch konfokale Resonanz-Raman-Mikroskopie“).

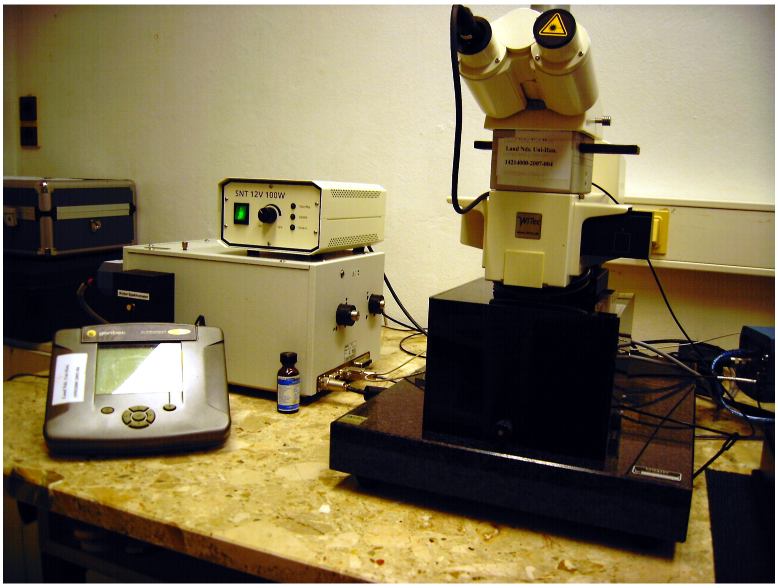

Figure 2.1: Confocal Raman microscopy workstation with the CRM 200 and SDU-1 at the institute of biophysics.

2.1.1 Equipment

The core components of the established setup is a confocal Raman microscope (CRM 200 by WITec, Ulm, Germany) (see Fig. 2.1 for a picture and Fig. 2.2 for the setup

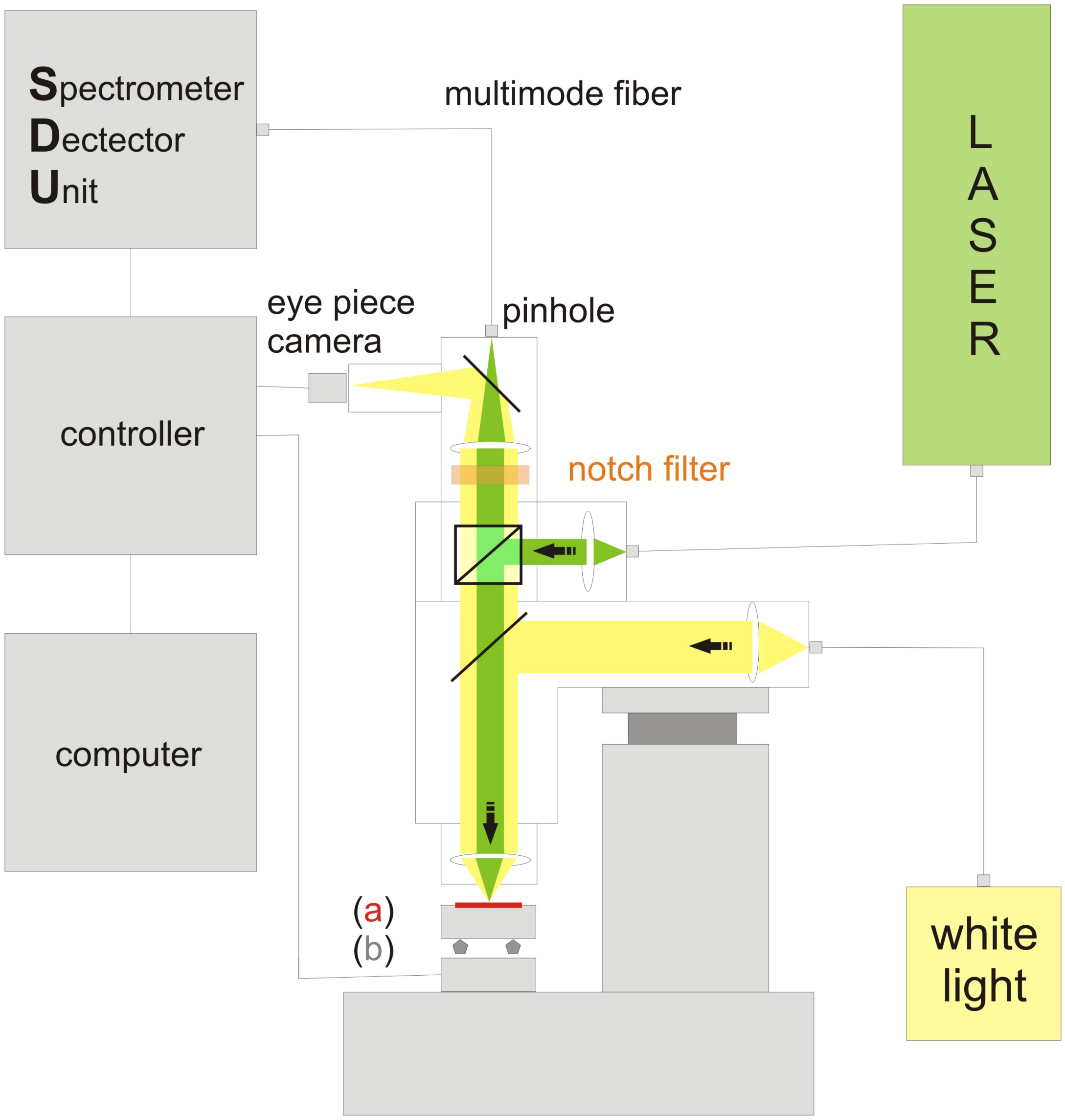
Spectrometer
Dectector
Unit
multimode fiber
LASER
eye piece
camera
pinhole
controller
notch filter
computer
(a)
(b)
white
light

Figure 2.2: Principal setup of the confocal Raman microscope CRM 200. A single mode fiber transports the laser beam into the microscope, where it is widened and directed via a holographic notch filter to the objective. The objective focuses the excitation beam into the sample plane (a) and collects the light scattering back from the sample. The back-scattered light passes through the holographic filter and a notch filter, blocking the majority of the Rayleigh light, before a lens focuses the remaining light onto the pinhole, defined by the diameter of the multimode fiber connecting the microscope with the spectrometer-detector-unit (SDU). The setup is computer controlled via a central control unit (controller), also operating the piezo-electric scan table (b) and the positioning of the sample plane via a step motor integrated in the microscope socket. For details on the SDU see Fig. 2.3. White light illumination serves for visual inspection of the sample via the eye piece camera prior and after Raman measurements.

scheme).

The **excitation wavelength** of 532 nm **is defined by the** target **chromophore** cytochrome-

c. Since cytochromes perform their metabolic function in the electron transport chain of bacteria by reversible changes in their redox state of the heme, both ferro- and ferricytochromes ought to be equally detected.
Ferrocytochrome-c (Fe^{2+}) and ferricytochrome-c (Fe^{3+}) show distinctly different absorption maxima. The steep main absorption band (soret), typically just above 400 nm, may shift up to 30 nm in the transition from ferrous to ferric state. However, the secondary absorption maxima (Q-band), despite being far less intense, are a lot more promising. Ferrocytochromes-c have a single, symmetric Q-band centered around 530 nm, while ferricytochromes-c show two sharp absorption maxima at 522 ± 2 and 553 ± 2 nm. Absorption intensities for the ferrous and the ferric state match near 532 nm [Pettigrew and Moore, 1987], allowing for excitation of both states with similar efficiency using **a frequency-doubled Nd:YAG laser**.

The numerical aperture (NA) of the objective in combination with the size of the pinhole (50 μm) defines the spatial resultion of the setup at a given excitation wavelength. It is defined as $NA = n \cdot \sin \Theta_{max}$ with n being the diffraction index of the medium between objective and sample and Θ_{max} being the acceptance angle of the objective. The aim of this work is the analysis of native biofilms on the **scale of bacterial cells** (1 - 5 μm^3). Two objectives with high numerical apertures were used for the results presented in this work: a water-immersion objective with a NA of 1.0 and an oil-immersion objective corrected for cover slips with an NA of 1.25. See Tab. 2.2 for specifications.

Specifications of the objectives

objective ID	type	N.A.	Mag.	axial†‡ [μm]	lateral† [μm]	comments
NIKON CFI Fluor	water-immersion	1.0	60	1.0	0.325	
NIKON CFI Achromat	oil-immersion	1.25	100	0.6	0.260	corrected for 0.17 mm cover slips

† resolution of the setup with 532 nm excitation and a 50 μm pinhole.

‡ in water ($n_s \approx 1.33$.

Table 2.2: Specifications of the objectives

The system was operated with two **spectrometer-detector-units (SDU)**, each consisting of a spectrometer and one or two detectors. While both SDUs were connected to the controller and software-controlled with ScanCTRL plus (CRM 200 operation software by WITec, Ulm, Germany), operation was mutually exclusive due to separate hardware configuration files being required. Camera calibration was software controlled with a Hg-Ar calibration lamp as reference.
SDU-1 (Andor) consists of an Acton 308-SP **diffraction spectrometer** with three differ-

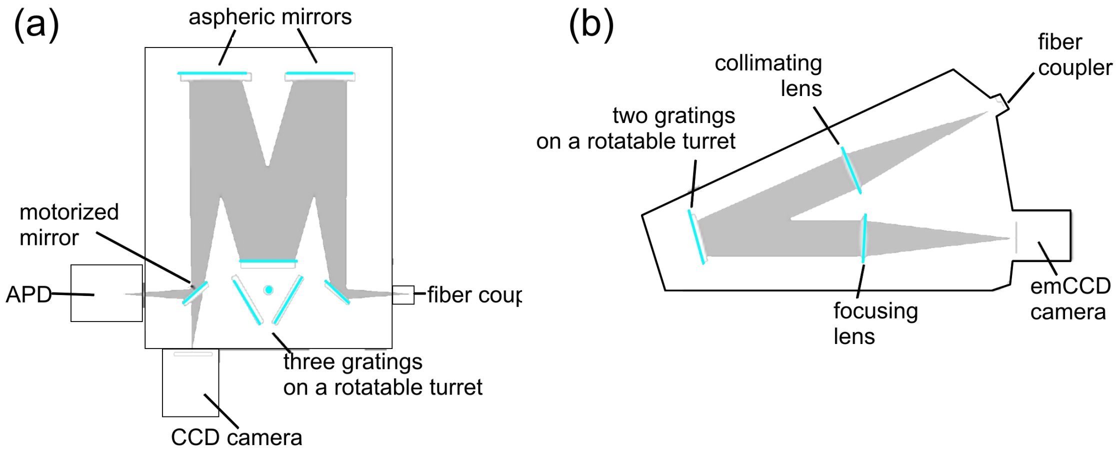
(a)
aspheric mirrors
motorized mirror
APD
fiber coup
three gratings on a rotatable turret
CCD camera
(b)
collimating lens
two gratings on a rotatable turret
fiber coupler
focusing lens
emCCD camera

Figure 2.3: SDU setups. (a): Acton-308-SP spectrometer with CCD camera (Andor DU401-BV) and Avalanche photodiode (SPCM-AQR). (b): UHTS 300 spectrometer with emCCD camera (Andor DU970N-BV-353). Schematic views ©WITec, Ulm, Germany.

ent gratings (150, 600, and 1,200 g/mm) on a rotatable turret. It is connected with two detectors: a **CCD camera** (ANDOR DU401-BV) with an 1,024 x 127 array of active pixels (size: 26 x 26 μm^2), electrically cooled to -70℃ the quantum efficiency is above 70 % between 500 and 820 nm; and a single-photon sensitive **avalanche photodiode** (SPCM-AQR) with a detection efficiency above 60 % between 540 and 800 nm. For a schematic view of the SDU see Fig. 2.3 (a). Experimental parameters are given in Tab. 2.4.

SDU-2 (Newton) consisted of a WITec UHTS 300 spectrometer, which was specifically constructed for Raman spectroscopy at visual wavelengths. Its transmission at 532 nm is above 60 %, limited mainly by the efficiency of the two gratings (600 and 1,800 g/mm; blaze wavelength: 500 nm). The single detector unit is an emCCD camera (ANDOR DU970N-BV-353), electrically cooled to -69℃ it has a similar quantum efficiency as the DU401-BV, but a neglible dark current. The CCD chip consisted of 16 x 16 μm^2 pixels in a 1,600 x 200 array. For a schematic view of the SDU see Fig. 2.3 (b). Experimental parameters are given in Tab. 2.4.

Specifications of the SDUs

component	spectral range[†] [rel. cm^{-1}]	spectral resolution [cm^{-1}]	spectral accuracy [cm^{-1}]
SDU-1 (CCD)	-125 – 3,694	4	2
SDU-1 (APD)	n.a.[‡]	n.a.[‡]	2
SDU-2 (emCCD)	-125 – 3,694	2	1

† with the 600 g/mm gratings available in both SDUs; position as used for results

‡ recorded spectral range around chosen center frequency: 4 cm^{-1}

Table 2.4: Specifications of the SDUs

2.1.2 Data acquisition and measurement modes

The control software of the CRM 200 (ScanCTRL plus by WITec, Ulm, Germany) allows several measurement modes, ranging from a single spectrum recorded at a specific coordinate, over point or time lines of recorded spectra, to rastered planes of full spectral information (spectral imaging). These modes are available with SDU-1 (CCD) and SDU-2 alike. Additionally, non-spectrally resolved three-dimensional image stacks can be automatically recorded with SDU-1 (APD). However, not all of these measurement modes are useful for analyzing bacterial samples or biofilms. The following two measurement modes were regularly used for the results presented in this work:

Spectral Imaging (also called „chemical imaging“ in literature):
a full spectrum is recorded on each measurement spot of a pre-defined raster plane, giving spatially resolved full spectral information on the plane. This mode with partially different parameters was used for measuring biofilm and samples of bacteria cultures (see 2.5.2):
Biofilm samples were measured with the water-immersion objective and SDU-1 (CCD) with the 600 g/mm grating. Recorded images consisted of 140 x 80 spectra, screening an area of 70 μm horizontally and 80 μm vertically (into the biofilm). The laser intensity was adjusted to 9 mW, giving 1.8 MW/cm^2 on the sample within the measurement volume. Measurement time per spectrum (or recorded pixel) was set to 1.0 s, sufficient for high-contrast resonance Raman spectra of cytochrome-c.
Bacteria samples were measured with the oil-immersion objective and SDU-2 (emCCD) with the 600 g/mm grating. Recorded images consisted of 100 x 100 spectra in a horizontal x-y plane, positioned 2 μm above the surface of the microscope slide. Measurement spots were distanced at least 3 μm to avoid thermal damage or photobleaching of neighboring cells. Laser intensity was adjusted to 25 mW, giving up to 4.7 MW/cm^2 on the sample within the measurement volume. Measurement time per spectrum was set to 0.5 s for bacteria producing cytochromes and to 0.1 s for carotenoid holding bacteria.

3D Imaging:
this mode is only possible with SDU-1 (APD) and does not provide spectrally resolved information. Therefore, it does not allow to differentiate between autofluorescence or a strong (targeted) resonance Raman line. However, it does allow for automatic recordings of image stacks, providing three-dimensional intensity information of approx. 4 cm^{-1} around a chosen center wavelength.
3D Imaging was used to gain insight into the three-dimensional structure of biofilms by recording the intensity distribution at 749 rel. cm^{-1}, the most stable line in the spectra of bacterial cytochromes-c (compare 3.2.3). Recorded image stacks consisted of 80 images distanced 1 μm along the z-axis (vertically into the granule). Each image consisted of 300 $\times$ 300 spectra, covering an area of 100 $\times$ 100 μm^2 in the xy-plane. Laser intensity was adjusted to 9 mW, giving 1.8 MW/cm^2 on the sample within the measurement volume. Measurement time was set to 0.1 s.

2.2 Spectral Images: Spatially resolved Raman data

The CRM 200 (see 2.1.1) operated with WITec ScanCTRL plus records rastered images with full spectral information for each recorded pixel. The controlling software stores these data in a project file (suffix: WIP), including the complete settings (hardware and software) with which the data were recorded. These data were digitally analyzed directly in the spatially resolved form as spectral images with WITec Project (see 2.2.1) or the individual spectra were exported for further analysis with OPUS spectroscopical software (see 2.3.1).

2.2.1 Software: WITec Project

WITec Project™ (version 1.94 by WITec, Ulm, Germany) is the analysis software for the data recorded with the CRM 200. It handles individual spectra as well as spectral images and allows the extraction of specific spectra from spectral images for individual handling, either directly in WITec Project or via spectrum export with other software.
Spectra are exported as two-dimensional ASCII arrays (spectral position k [cm^{-1}], intensity y at k [counts]). Spectral images prepared in WITec Project are exported as bitmaps.
WITec Project **does not alter the data records**. Rather than manipulating the stored data directly, its analysis routines provide specifications for the visual display of the data, which – after completion of the analysis – are saved as new data objects. Important: **all objects are linked to the original data records**.
The software provides many analysis features for individual spectra as well as spectral images, including spectral, spatial, and time interpretation, multiple smoothing routines, background substraction (by polynomial fit) (see 2.2.2), the distribution of specific Raman lines throughout the sample (see 2.2.3), and the analysis of basic components (see 2.2.4). However, it does not include a routine for peak analysis in a full spectrum (compare 2.3.2). It gives precise control over the **graphical properties of displayed images**, including color scheme, intensity per pixel, and contrast (minimum and maximum intensity settings) for full spectral as well as filtered images, and allows the **superposition of multiple images** with adjustable contrast settings and color schemes [WITec GmbH, 2005].

2.2.2 Background Subtraction

The unavoidable background in the Raman spectra was addressed in two ways:

1. **by subtracting a dark spectrum** recorded prior to the actual measurement with the same settings. This was done unequivocally to all recorded spectrally resolved data, spectral images as well as exported individual spectra.

2. **by polynomial fit**. This was done only for the creation of filtered images (see 2.2.4). Spectral region (the fingerprint area) and the order of the polynomial fit (9^{th} order) were user defined and performed independently on each pixel of the spectral image, using the Background Subtraction routine in WITec Project (see 2.2.1).

In addition, several analysis routines of WITec Project perform an **automated localized background subtraction**. For this, the background B_i is computed from the intensity values I_i' and the spectral positions x_i left and right of the filtered spectral region [WITec GmbH, 2005].

2.2.3 Peak Analysis routines

WITec Project (see 2.2.1) incorporates several routines for filtering information from spectral images, ranging from displaying the intensity within a user-defined range (Sum Filter) over displaying the distribution of extreme values (Min Max Filter) or the width of a specific Raman line (Width Filter) to returning the position of a Raman line determined with a parabolic fit (Parabolic Filter) [WITec GmbH, 2005]. All these routines perform an automated background subtraction (see 2.2.2).
In the following equations $k = n_1...n_2$ is the user-defined spectral range and I_k the background corrected intensity value at the k^{th} pixel.

Sum plainly sums the CCD counts recorded within the user-defined spectral range:

$$\text{Sum} = \sum_{k=n_1}^{n_2} I_k \tag{2.1}$$

Min and Max returns the extreme values and their positions in the user-defined spectral range:

$$\begin{aligned} \text{Minimum} &= \min\left(I_k : n_1 \leq k \leq n_2\right) && (2.2)\\ \text{Position of Minimum} &= min(x_k : I_k = \text{Minimum}, n_1 \leq kn_2) && (2.3)\\ \text{Maximum} &= \max\left(I_k : n_1 \leq k \leq n_2\right) && (2.4)\\ \text{Position of Minimum} &= min(x_k : I_k = \text{Maximum}, n_1 \leq kn_2) && (2.5) \end{aligned}$$

Width displays straightforward the width of a selected Raman line, measured at a user-defined height of the peak.

Parabolic is one of the more computation-intensive routines. It returns the distribution of a specific Raman line in a spectral image based on a parabolic fit for the selected peak. The routine returns the curvature of the fit, the detected center of the Raman line, its intensity, and an error.

2.2.4 Filtered Images

The distribution of specific Raman spectra within a recorded spectral image can be determined with the Basis Analysis routine of WITec Project (see 2.2.1). Background subtraction (2.2.2) by polynomial fit is required for this procedure to work. The spectral region used in the analysis can be specified.

The Basis Analysis routine returns the quantity of pure components in a mixed sample under the assumption that the Raman spectrum of the sample is a linear superposition $\vec{S}$ of the Raman spectra $\vec{B}$ of N pure basis components:

$$\vec{S} = \sum_{m=1}^{N} a_m \vec{B}_m \tag{2.6}$$

In case of known $\vec{B}_m$, the weighting factor a_m is estimated with a least-square-fit and returned as an image linked with the full spectral data [WITec GmbH, 2005].

2.3 Analysis of individual Raman spectra

Individual Raman spectra can be exported for further analysis as two-dimensional ASCII arrays (spectral position k [cm^{-1}], intensity y at k [counts]) from the spectral images recorded with the CRM 200 using either the controller software (ScanCTRL plus) or WITec Project (see 2.2.1).

2.3.1 Software: OPUS

OPUS™ by Bruker Optik GmbH, Ettlingen, Germany (used in version 5.5 with the IDENT routine for hierarchical cluster analysis) is an extremely popular and very widely used proprietary software suite for the analysis of spectroscopic data. It allows far-reaching, even extreme data manipulation, and is one of the quasi-standards worldwide when it comes to spectra comparison, hierarchical cluster analysis, and the professional presentation of spectra. It also includes an interface for hardware controlling. However, OPUS handles only individual spectra – not spectral images – and the CRM 200 is not in its list of directly supported hardware. Therefore, individual or averaged spectra were exported as ASCII files from WITec Project (2.2.1) and imported to OPUS for further analysis and presentation.

OPUS keeps a precise history of the manipulations performed on the data, but does not retain the unaltered data. Unfortunately, its documentation lacks significant detail and even basic references regarding its extensive data manipulation capabilities and analysis features. This includes even critical procedures such as „spectrum quality check“ and „signal-to-noise calculation“, which are only shown for absorption spectra [Bruker GmbH, 2004]. Since these properties are critical for the subsequent analyses, and the reliability of the OPUS routines could not be confirmed for bacterial Raman spectra, the signal-to-noise ratio as a measure for spectrum quality was determined and quantified manually as described in 3.1.2.

However, the documentation of the routines for „peak search“ (see 2.3.2), „spectrum comparison“ (see 2.3.3), and „hierarchical cluster analysis“ (see 2.3.4), despite their appalling lack of verifiable references, was sufficient for the use of these features.

2.3.2 Raman Line Search and Comparative Spectrum Analysis

Raman spectra recorded with the CRM 200 are naturally vectors of data points in the space of relative wavenumbers. The peak search routine of OPUS software (see 2.3.1) interpolates the discrete values of the vector to a smooth curve matching the recorded data points and determines the **peak positions** in this interpolated curve straightforward (standard method) by finding the positions of the local maxima. **Relative intensity** is determined with respect to a locally defined baseline. The localized baseline is found as follows: search of the next Raman line of at least equal intensity (or the end of the recorded spectrum) to the analyzed peak. The lowest point between these two peaks is defined as a local minimum. The nearest so defined minima left and right of the analyzed peak give the localized baseline [Bruker GmbH, 2004].

For Raman spectra with significant background, such as the spectra of bacteria containing cytochrome-c, it is recommendable to do the peak search in intervals of only moderate change in the respective background intensity, otherwise the routine often miscalculates what constitutes a „nearest minimum“ and thus miscalculates or omits especially weaker lines.

For a **comparative spectrum analysis** (CSA), the sensitivity settings for OPUS peak search finding exactly the Raman lines which can be clearly identified by the naked eye in the spectrum of the native sample were applied without variance to treated samples. In addition, it was determined which Raman lines could be identified with optimal settings for the spectrum of the treated samples without causing false positives. This gives a fast and easily reproducible test for changes in Raman spectra recorded from differently treated samples.

2.3.3 Spectrum Comparison

Spectrum comparison works straightforward with the spectrum vectors $y_i(k)$ with k being the number of recorded data points within the spectral range over which the i spectra are to be compared. It calculates the correlation coefficient r_{corr} as

$$r_{corr} = \frac{Cov(y_i(k), y_j(k))}{\sigma_i \sigma_j} \tag{2.7}$$

with $Cov(y_i(k), y_j(k))$ being the covariance between the vectors y_i and y_j and σ_i being the standard deviation of spectral vector y_i. The correlation coefficient r_{corr} can have values between -1 (inverse spectra) and 1 (identical spectra).

Spectrum comparison is implemented as a standard routine in the OPUS software (see 2.3.1), giving r_{corr} in per cent as follows: $-1 \leq r_{corr} < 0$ gives 0 % correlation and $0 < r_{corr} \leq 1$ is converted linearly to 0 – 100 % correlation of the compared spectra [Bruker GmbH, 2004].

2.3.4 Hierarchical Cluster Analysis

Hierarchical Cluster Analysis (HCA) is a means of structuring a complex set of observations into unique, mutually exclusive groups (clusters) of subjects similar to each other with respect to certain characteristics, which may not be known prior clustering. Thus, it has become a widely used tool for the unsupervised structuring of complex experimental data, because – in contrast to other clustering techniques such as K-means clustering or support vector machines – it does not require a priori knowledge of the data and is not limited to the starting conditions. The required data preparation is fairly moderate, requiring primarily the exclusion of freak values [Sharma, 2006].
Hierarchical cluster analyses in this work were performed with the additional software module OPUS IDENT for OPUS (see 2.3.1).

Algorithms for HCA

The most widely used algorithms for HCA are Single-Linkage, Complete-Linkage, Average-Linkage, Weighted-Average-Linkage, Centroid, Median, and – most notably – the Ward algorithm, which is extremely popular for clustering biological data [Ward, jr., 1963][Primpas et al., 2008]. All of these algorithms choose or calculate a representative for each cluster from the data clustered together. Subsequently, the distance between the clusters is calculated with a specified distance (or similarity measure) such as Euclidian Distance (see 2.3.4) or Factorization [Sharma, 2006].

The algorithms are defined as follows:

Single-Linkage
$$D(r,i) = min[D(p,i), D(q,i)] \tag{2.8}$$

Complete-Linkage
$$D(r,i) = min[D(p,i), D(q,i)] \tag{2.9}$$

Average-Linkage
$$D(r,i) = \frac{D(p,i) + D(q,i)}{2} \tag{2.10}$$

Weighted-Average-Linkage
$$D(r,i) = \frac{n(p)D(p,i) + n(q)D(q,i)}{n(p) + n(q)} \tag{2.11}$$

Centroid
$$D(r,i) = \frac{n(p)D(p,i) + n(q)D(q,i)}{n} + \frac{n(p) + n(q)D(q,p)}{n^2} \tag{2.12}$$

$$\text{Median} \quad D(r,i) = \frac{D(p,i)+D(q,i)}{2} - \frac{D(q,p)}{4} \tag{2.13}$$

$$\text{Ward} \quad D(r,i) = \frac{[n(p)+n(i)]H(p,i)+[n(i)+n(q)]H(q,i)-n(i)H(q,i)}{n+n(i)} \tag{2.14}$$

with r being the cluster formed out of the clusters p and q, $D(r,i)$ being the spectral distance between the clusters r and i, $H(r,i)$ being the Heterogeneity between the clusters r and i, $n(i)$ being the number of spectra included in cluster i, and n being the number of spectra included in the clustering. The variables $H(p,i)$, $H(q,i)$, $D(p,i)$, $D(q,i)$, $D(q,p)$, $n(p)$ and $n(q)$ are defined analogously.
The above listed algorithms are incorporated in the additional software module OPUS IDENT for OPUS (see 2.3.1)

Distance measure

Spectral distances were calculated with the Euclidean distance:

$$D(i,j) = \left[\sum_k (y_{jk} - y_{ik})^2\right]^{\frac{1}{2}} \tag{2.15}$$

with the spectral distance $D(i,j)$ between the spectra y_i and y_j and k going over all recorded data points within the spectral region of interest (600 - 1,800 cm^{-1} throughout this work).

2.4 Absorption spectroscopy

The available scientific spectrometer (Kontron UVIKON 932 by Kontron Electronics, Switzerland) allowed the recording of absorption spectra between 190 and 900 nm. Spectral resolution was 1 nm. Measurement time per nm was 1 s.
The analysis of the recorded absorption spectra was done with Origin™ 5.5 by OriginLab Corporation, Northampton, USA.

2.5 Biological materials and procedures

Resonance Raman micro-spectroscopy at 532 nm is not compatible with most standard methods for bacteria and biofilm analysis, such as FISH, requiring the application of fluorescent dyes. Therefore it is essential to test it on fully characterized bacteria (see 2.5.2) and biofilm samples (2.5.1) with known properties.

2.5.1 Biofilm granules

Biofilm granules were sampled from two lab-scale sequencing batch reactors (SBR), operated and monitored at the Institute of Biophysics (see Fig. 2.4). An SBR is a discontinuously loaded tank for the biological treatment of industrial or municipal wastewater. Its operation depends on the properties of the microbial biofilms it contains. The SBRs at the Institute of Biophysics had a tank volume of 12.8 l, of which 10 l were used in operation. The details of the operation procedures are described by Wesoly [2009].

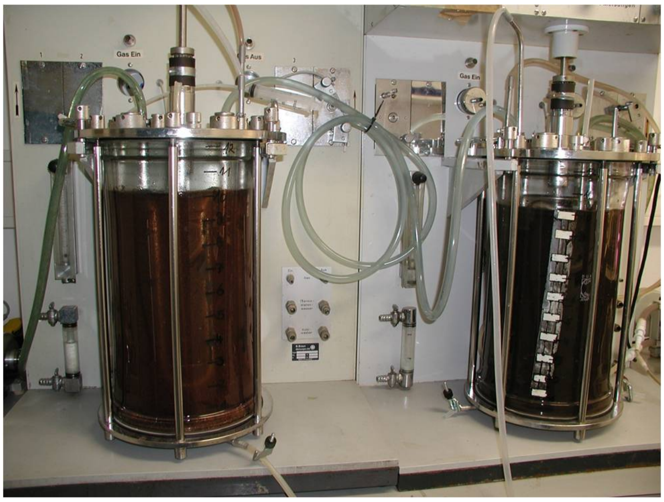

Figure 2.4: Sequencing batch reactors (SBR) for anaerobic ammonium oxidization at the Institute of Biophysics. Photo kindly provided by Dr. I. Wesoly.

SBR-1 was started with seeding sludge from an operational anammox-IC in Rotterdam [van der Star et al., 2008] and showed steady anammox activity after a startup phase of approx. two weeks. The main anammox organism present was *candidatus Brocadia anammoxidans*, tested with the FISH probe Ban162 [Wesoly, 2009]. SBR-1 was kept in continuous operation, showing steady anammox activity.

SBR-0 was identical to SBR-1 in construction and operation, but started without seeding sludge. Three weeks after the beginning of operation, an increasing population of not otherwise specified purple bacteria was observed in SBR-0. SBR-0's operation was discontinued after three months when no deammonification occured.

Granules Sampling and Preparation

Samples for subsequent resonance Raman measurements were taken from the SBRs always at the same phase of the operation cycle (during stirring). 50 ml of reactor water including microbial granules were sampled with a wide syringe at half-height from each SBR immediately prior to measurements.
A single granule of average size (diameter: 1 mm) was taken from the sampled volume and placed free-floating in ample bulk liquid on an uncoated 1.2 mm indentation slide. The cover slip was sealed with acrylic lacquer to the slide to avoid dehydration of the sample. Measurements were started 2 min after sealing (to allow for drying of the sealing lacquer).

2.5.2 Bacteria cultures

Bacterial cultures were chosen with respect to their expressed chromophores (purple non-sulfur bacteria) and relevance to the waste water environment providing the sample granules (*Nitrosomonas*).

Purple non-sulfur (PNS) bacteria

Purple non-sulfur (PNS) bacteria belong to the Alphaproteobacteria (with few exceptions being grouped into the Betaproteobacteria) and are generally physiologically flexible: Under anaerobic conditions, PNS-bacteria are able to grow photoheterotrophically, expressing bacteriochlorophyll and strain-specific carotenoids, thus providing useful chromophores for resonant Raman excitation [Imhoff, 2006].
PNS-bacteria were chosen as sample organisms, because they are comparatively well understood and of widespread use in many fields of research, especially anoxic bacteriophotosynthesis [Cogdell et al., 2006, Mackenzie et al., 2007]. Their carotenoid synthesis occurs – with few exceptions – along the spheroidene pathway [Takaichi, 2008a], starting with neurosporene (9 conjugated C=C bonds) towards spheroidene (10) or spirilloxanthin (13) which has the longest conjugated chain seen in PNS bacteria [Koyama, 1995]. However, photosynthesis and respiration of PNS bacteria share a common electron transfer chain, with oxygen exposure affecting the carotenoid synthesis as well as the expression of bacteriochlorophylls and several cytochromes, including bc$_1$ and c$_2$ (both functional under aerobic conditions) and cbb$_3$ (functional under low oxygen conditions) [Imhoff, 2006, Mackenzie et al., 2007].

Four strains of photosynthetic Alphaproteobacteria were chosen for this work:

- ***Rhodobacter sphaeroides*** **DSM 158^T** with a cell size of approx. 1 μm is one of the crucial organisms for research in bacteriophotosynthesis. Its photosynthetic apparatus contains primarily the carotenoid spheroidene.
- ***Rhodobacter sphaeroides*** **DSM 2340^T** is a carotenoids-free mutant of DSM 158.
- ***Rhodopseudomonas palustris*** **DSM 123^T** is a taxonomically close relative to *Rhodobacter* with a slightly larger cell size of 1.2 μm, growing under similar conditions. It contains primarily the carotenoid spirilloxanthin.
- ***Rhodospirillum rubrum*** **DSM 467^T** is a spiral-shaped bacterium with a cell size of up to 5 μm. Like *Rhodopseudomonas*, it holds primarily the carotenoid spirilloxanthin.

The respective bacterial type strains were obtained as freeze-dried cultures from German Collection of Microorganisms and Cell Cultures (Deutsche Sammlung von Mikroorganismen und Zellkulturen [DSMZ]), Braunschweig, Germany. The freeze-dried pellets were

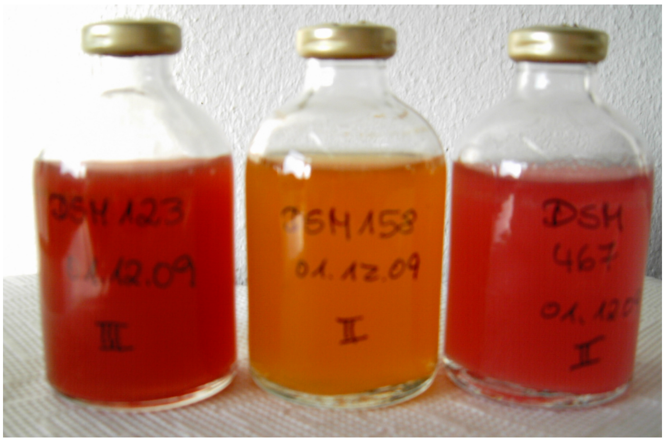

Figure 2.5: Flasks with cultures of *Rhodopseudomonas palustris 123*, *Rhodobacter sphaeroides 158*, and *Rhodospirillum rubrum 467* in harvesting condition.

activated as recommended by DSMZ and cultured anaerobically in medium DSM 27 modified for oxygen sensitive species. All cultures were incubated at 25 °C in an illuminated climate chamber on a rotary shaker at 200 rpm. Growing cultures were regularly inoculated in fresh medium as soon as the photometrically determined optical density at 578 nm (OD_{578}) exceeded 2.0 compared with sterile medium as control (spectrophotometer Cadas 200 by Hach Lange GmbH, Berlin, Germany; standard single-use cuvettes). Fig. 2.5 shows (from left to right): *Rhodopseudomonas palustris*, *Rhodobacter sphaeroides*, and *Rhodospirillum rubrum* cultures in their inoculation flasks.

Nitrosomonae

Nitrosomonas bacteria are crucial organisms for the biological treatment of industrial and municipal wastewater. *Nitrosomonae* are also found in the outer layers of anammox biofilms, thriving in the not fully anaerobic habitat [Tsushima et al., 2007]. Their sole source of energy is aerobic ammonium oxidization, a process for which several different cytochromes-c are required [Pettigrew and Moore, 1987].
Four strains of *Nitrosomonae* expressing cytochrome-c were provided as liquid cultures by Dr. Pommerening-Röser of the Biozentrum Klein Flottbek, Hamburg, Germany:

- ***Nitrosomonas communis*** strain Nm-02 was originally discovered in soil on isle of Corfu.
- ***Nitrosomonas europaea*** strains Nm-50, Nm-53. Nm-50 was originally discovered in soil (USA).
- ***Nitrosomonas eutropha*** strain Nm-57, originally discovered in municipal sewage (Chicago, USA).

All strains were cultured using media and conditions as described by Koops et al. [1991].

Bacteria Sampling and Preparation

The **purity of cultures** was checked microscopically prior to sampling (phase contrast, 100-fold magnification, Zeiss GmbH, Oberkochen, Germany).

For **absorption measurements**, a standard cuvette (optical path = 1 cm) was filled with bacteria solution and measured against a cuvette filled with the growth medium as reference. The solutions of DSM 123, DSM 158, and DSM 467 (and the respective medium reference) were thinned to 10 % with phosphate buffered saline (PBS; pH 7.2) to remain within the sensitivity range of the spectrometer (see 2.4). DSM 2340 was measured in growth density.

For **Raman measurements**, a volume of 1 ml of cell suspension was sampled from the actively growing cultures of purple non-sulfur bacteria at a cell density of 10^6 to 2×10^6 cells per milliliter (as estimated from OD_{578}), centrifuged for 5 min at 14,500 g at 4℃, washed with PBS, and pelletized again. For the *Nitrosomonas* cultures, a volume of 15 ml of cell suspension was sampled, which was centrifuged for 30 min at 8,000 g, washed with PBS, and pelletized.

If not stated otherwise, washed cell pellets were mounted on standard microscope slides (ISO Norm 8037/1 microscope slides by Menzel-Gläser, Braunschweig, Germany), covered with a 0.17 mm cover slip, and measured immediately.

For analyzing the effect of adhesive surface coatings, slides with a poly-L-lysine coating (Polysine™ by Menzel- Gläser) were used.

2.5.3 Fixation

Three of the least invasive fixation protocols widely used in many biological and medical applications are ethanol, PFA, and Gentle Heat fixation.

Ethanol (EtOH)

Ethanol solution is assumed to displace intracellular water, thus reducing the water activity (a_w) of the cells and ultimately causing their proteins to coagulate [Denyer, 1995, Denyer and Steward, 1998, Rutala, 1989]. Since the coagulation effect is pronounced more strongly with some residual water present, EtOH is generally considered to be most effective as bactericidal agent when used in a final concentration of 60 to 70 % vol/vol [Larson and Morton, 1991]. Additionally, exposure to EtOH solution at lower concentration is associated with the solubilization of the phospholipids as integral elements of the bacterial membrane [Ballesteros et al., 1993].

EtOH fixation protocol: Cells were resuspended in 300 μl of analytical grade ethanol to a final volumetric concentration of ethanol of 70% and stored at room temperature.

Formaldehyde (PFA)

Formaldehyde solution, which has been used as a fixative for cells and tissues in the biological, medical, and pathological sciences for more than a century [Fox et al., 1985], causes substantial chemical changes in peptides, most notably stable methylene bridges linking primary amino (including lysine) and thiol groups irreversibly with several other amino acid residues [Metz et al., 2004].

PFA fixation protocol: Cells were resuspended in 1 ml of 4% paraformaldehyde (PFA) solution (4% wt/vol in PBS, pH 7.2) and stored at room temperature.

Gentle Heat (Heat)

Although moist heat under overpressure (autoclavation; at least 121 °C in hot steam) is known to effectively kill bacteria as well as their even more resistant spores for most hygienic applications, the mechanisms of action at temperatures well below 100 °C still lack full understanding. Heating suspended bacterial specimen to temperatures in the range of 60 to 90 °C generally results in an inactivation, i.e., loss of capability to reproduce. Other specific cell properties, such as the antigenic identity, may remain intact. Among the reported heat-related effects are protein coagulation, breakdown of nucleic acids, and leakage of molecules of low-molecular weight through the cell membrane. There are, however, effective mechanisms known how several bacterial species can cope with short-time heat exposure [Russel, 1991].

Gentle Heat fixation protocol: The harvested cell pellet was resuspended in 1 ml sterile PBS and heated to 70 °C in a thermostatted shaker (Thermomixer 5436, Eppendorf AG, Hamburg, Germany).

Preparation of fixed samples

Harvested, PBS-washed, and pelletized bacteria cells (see 2.5.2) were subjected to the respective fixation protocol for EtOH, PFA, or Gentle Heat fixation (see 2.5.3).
Upon completion, the fixatives were thoroughly removed from the sample by centrifuging and washing with PBS, as described in 2.5.2. This step was applied twice. The heat fixed samples were treated identically.
Efficiency of fixation (i.e. cultured bacteria were no longer viable, but cells morphologically intact) was checked for by inoculating three bottles of sterile medium with 200 μm of the fixed sample (by EtOH, PFA, and heat respectively). The control flasks were incubated under conditions identical to the culture flasks. If no visible growth occured after two weeks, the fixation was considered complete.

3 Resonance Raman spectra of bacteria

Bacteria are very ingenious lifeforms, capable of complex metabolical functions and changes, even without association in biofilms. Therefore, the living (a.k.a „native“) bacterial cultures used in this study were carefully analyzed for the chromophores contributing to their (resonant) Raman spectra (see 3.2).
In addition, the effects of standardized practices for bacteria preservation such as fixation on subsequent Raman measurements were examined (see 3.3). Fixation allows the transport and storage of bacteria samples in a given condition and sending fixed samples is therefore the method of choice for delivering bacteria intended for analysis elsewhere. In addition, fixation is a necessary step in many standard methods in microbiology and medical applications. However, fixation undoubtedly causes significant biochemical – i.e. molecular – changes in the cells (compare 2.5.3), giving rise to wonder whether the Raman spectral information of bacteria is really unaltered by fixation as is generally claimed.

Parts of this chapter were previously published in Kniggendorf et al. [2011a], Kniggendorf et al. [2011b], and Kniggendorf and Meinhardt-Wollweber [accepted for publication w.m.r.].

3.1 Properties of Raman spectra recorded from native samples

Raman spectroscopy is a technique used in many different fields of research, ranging from experimental physics and analytical chemistry over material sciences to medical and biological analyses, fields in which manners and customs differ traditionally. With respect to the interdisciplinary topic of this work, this section will start with a concise list of how the various variables are defined and used.

Please note: According to the International Union of Pure and Applied Chemistry (IUPAC), Raman spectra are to be given with the Stokes lines to the left. However, the overwhelming majority of Raman spectra in biological and medical publications are presented in the reverse direction. In order to achieve greater comparability with the majority of published spectra and to follow the convention in the publications of the fields for which this work may be of interest, the Raman spectra presented throughout this work are also given in reverse direction.

3.1.1 Description

Figure 3.1 shows a typical resonance Raman spectrum of a bacterium. The spectrum, described as a vector $\vec{y}$ of intensity values y_k recorded at pixel k, can be divided into the following components:

$$\vec{y} = \vec{s} + \vec{b} + \vec{n} \tag{3.1}$$

Signal $[\vec{s}]$ is the summary term for the Raman lines, including the resonantly enhanced lines of the main (or target) chromophore (and in case of strong resonances also higher orders of them), but also Raman lines originating from other chromophores.

Likewise, **background** $[\vec{b}]$, often called „determinate noise", holds many components, such as fluorescence, phosphorescence, remnants of the laboratory illumination, a characteristic dark spectrum caused by the experimental setup, etc. In this work, background summarizes the non-Raman components of a spectrum that cannot be influenced by statistical means such as averaging.

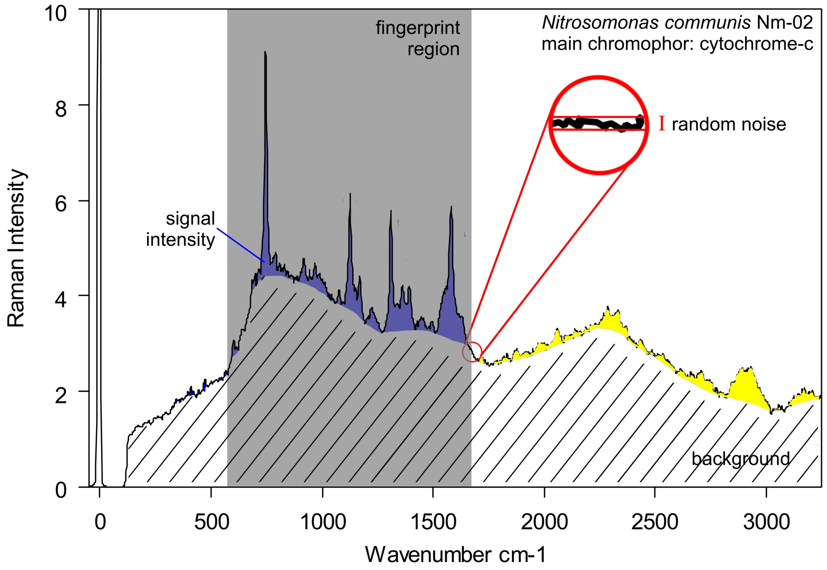

Figure 3.1: Main features of a typical bacterial resonance Raman spectrum: signal intensity (first order of the main chromophore: blue; higher orders and non-related Raman bands: yellow), background or „determinate noise" (hatched), random noise (magnifier), and the fingerprint region (shaded). [bacterium: *Nitrosomonas communis* Nm-02; main chromophore: cytochrome-c; excitation: 531.9 nm for 0.5 s]

Random noise $[\vec{n}]$ strictly describes the statistical noise component caused by the Shot effect, the detector array, etc. that can be reduced by averaging multiple spectra.

3.1.2 Critical: spectrum quality

Spectrum quality is a critical variable esp. for spectrum comparison and hierarchical cluster analysis (HCA). For its reliable quantification, the following definitions for the terms in eq. 3.1 were used:

Signal $[\vec{s}]$ was measured as intensity exceeding the underlying fluorescent background $[\vec{b}]$ and random noise $[\vec{n}]$.

The **random noise** $[\vec{n}]$ was determined as the maximal amplitude about the mean intensity between 40 and 90 cm^{-1}, since the Notch filter blocks radiation below 115 cm^{-1}. To verify the appropriateness of this definition, the random noise in the respective dark spectra was determined in intervals of 50 cm^{-1} around the positions of the four most prominent signal peaks of each chromophore spectrum. The results differed less than 5% from the noise level determined in the filtered area of the actual spectra records. This definition of random noise returns a higher value than the more common standard deviation or mean square error (MSE) definitions and explicitly does not cover in-spectrum noise due to fluorescence, but it can be determined directly in each recorded spectrum without relying on additional software (compare 2.3.1).

In-spectrum components of noise were deliberately not taken into account, since the decision between tiny Raman lines and high random noise amplitudes caused by fluorescence is inherently unreliable due to the complexity and delicacy of the resonant chromophore spectra of cytochrome c and carotenoids, esp. given different bacterial (or unknown) samples with possibly unknown Raman features.

The **signal-to-noise ratio** was determined straightforward as s/n for the four most prominent Raman lines of each spectrum within the interval of interest and averaged to give a single signal-to-noise ratio (S/N), reflecting the quality of the whole spectrum within the interval of interest (typically the fingerprint region).

3.2 Characterization of native bacteria

While Raman spectra allow the direct identification of present chromophores, the restriction of the measurements to a single wavelength does not allow for a direct determination of the (pre)-resonance condition for the respective chromophore(s) (except by literature) if tunable excitation is not available. Therefore – and to test for possible chromophores not expected in the bacteria – all bacteria cultures used in this study were additionally characterized either directly by absorption spectroscopy performed on the cultures (purple non-sulfur bacteria) or by comparison with the pure substance of the chromophores identified in the respective Raman spectra (*Nitrosomonae*).

3.2.1 Bacterial Reference spectra

Living bacteria have a natural variability that cannot be completely controlled even with strictly controlled culture conditions. Cell growth and subsequent cell division are always present in a native culture.

In order to avoid this natural variability to cause a bias in the results of the experiments, **bacterial reference spectra** were created for every culture by averaging at least 100 Raman spectra recorded from single cells. The Raman spectra used to create the references had an S/N $\geq$ 10 (with the exception of DSM 2340 (see 3.2.2), the spectra of which seldom had an S/N > 4) and were recorded from the same respective sample each.

The **validity of the references** was tested by comparison with additional references made from spectra recorded from different cells of the same sample, recorded from a different sample on the same day of cultivation, and recorded from a sample taken on a different day of cultivation. All references showed less than 0.5 % variation in spectrum comparison (see 2.3.3), giving a spectral distance of 0.11 or less when subjected to HCA (see 2.3.4).

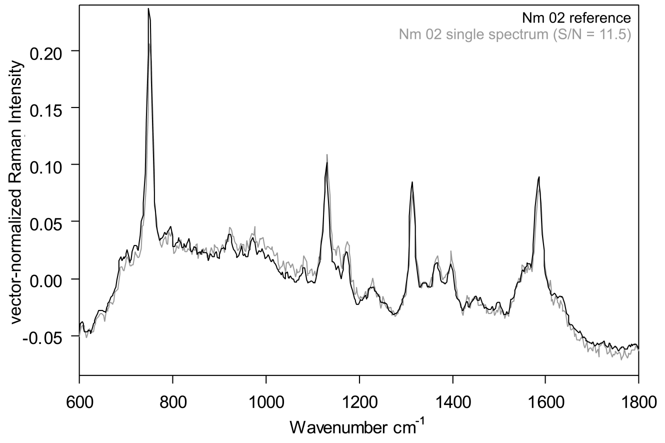

Figure 3.2: Reference spectrum (average of 100 single spectra of S/N $\geq$ 10) and single spectrum (S/N = 11.5) of *Nitrosomonas communis* Nm-02 in vector normalization. (Figure first published in Kniggendorf et al. [2011a].)

With the exception of DSM 2340, all **references** used in further analysis **had a S/N of approx. 100** as defined in 3.1.2. The reference for DSM 2340 had a S/N of 11 placing it in the same range as single spectra recorded from individual cells of the other bacteria. DSM 2340 was therefore not used when comparing references. Figure 3.2 gives a vector normalized single spectrum of *Nitrosomonas communis* with an S/N of 11.5 in comparison to the corresponding reference spectrum to illustrate the differences in spectrum quality between single and reference spectra.

The culture of *Nitrosomonas eutropha* Nm-57 (see 3.2.3) contained a significant amount of carbonate crystals (full size as well as microparticulates in direct contact to the bacteria cells; see Fig. 3.3). This was traced back to a precipitation event of carbonate in the culture medium. The culture did not yield enough Nm-57 cells without carbonate traces in their Raman spectrum to create a reference spectrum with an S/N ≥ 100. A second

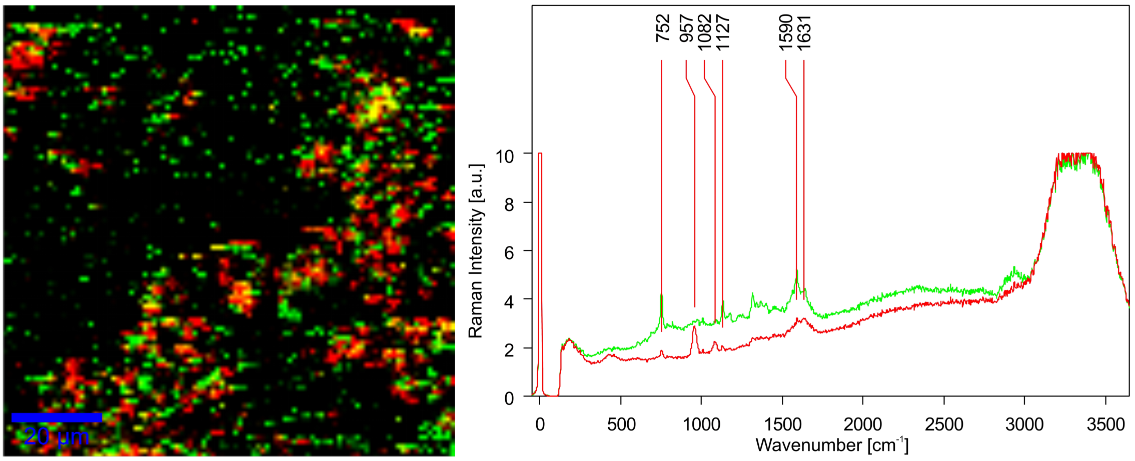

Figure 3.3: Distribution of carbonate particulates (red) in the native culture of *Nitrosomonas eutropha* Nm-57 (green). Yellow signifies carbonate and *Nitrosomonas* being equally present within the measurement volume of 1 μm^2. Sample was resuspended in PBS for the measurement. For details on the construction of the spectral image (left) see 5.1.

attempt to cultivate Nm-57 with fresh medium was not successful. The best possible reference spectrum for Nm-57 had an S/N of 20, but left no unused single spectra of Nm-57 for comparisons and/or an additional reference spectrum to test its natural variability in HCA. Therefore, *Nitrosomonas eutropha* Nm-57 was excluded from experiments beyond the plain analysis of its spectrum in 3.2.3.

The subsequent analyses of bacteria Raman spectra were done on the respective reference spectra if not stated otherwise.

3.2.2 Purple non-sulfur bacteria: carotenoids and cytochromes

Purple non-sulfur bacteria (PNS) are physiologically very flexible bacteria (see 2.5.2), thus requiring careful characterization with respect to the chromophores present in the cultures used in the study.

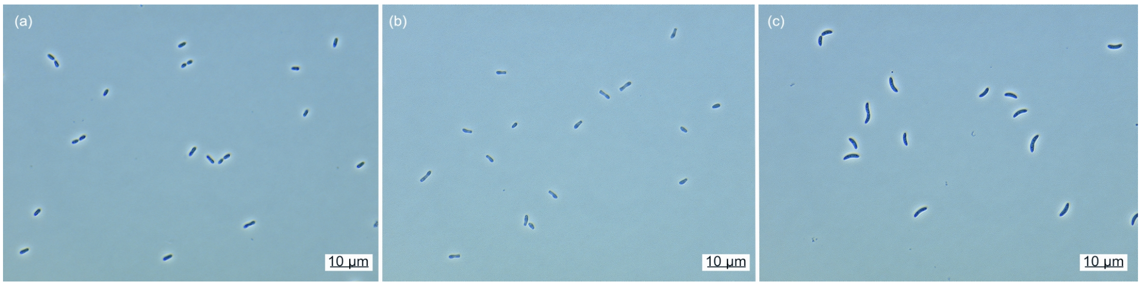

Figure 3.4: Phase-contrast micrographs of growing PNS type strain cultures showing different cell shape and size: *Rhodobacter sphaeroides 158* (a), *Rhodopseudomonas palustris 123* (b), and *Rhodospirillum rubrum 467* (c). (Figure first published in Kniggendorf et al. [2011b])

Since the carotenoids expected in *Rhodobacter sphaeroides* DSM 158^T, *Rhodopseudomonas palustris* DSM 123^T, and *Rhodospirillum rubrum* DSM 467^T are not available as pure substances (except via extraction from the bacteria and subsequent high-perfomance liquid chromatography (HPLC)), the absorption spectra of the native (i.e. living) bacteria in planctonic culture were analyzed. Phase-contrast micrographs of native DSM 123, 158, and 467 are given in Fig. 3.4. The culture of the carotenoids-free *Rhodobacter sphaeroides* DSM 2340^T did not reach a cell density (or culture volume) to allow for direct absorption spectroscopy on the native culture. Therefore its Raman spectrum was analyzed and compared to literature to determine the main chromophores and confirm the absence of carotenoids.

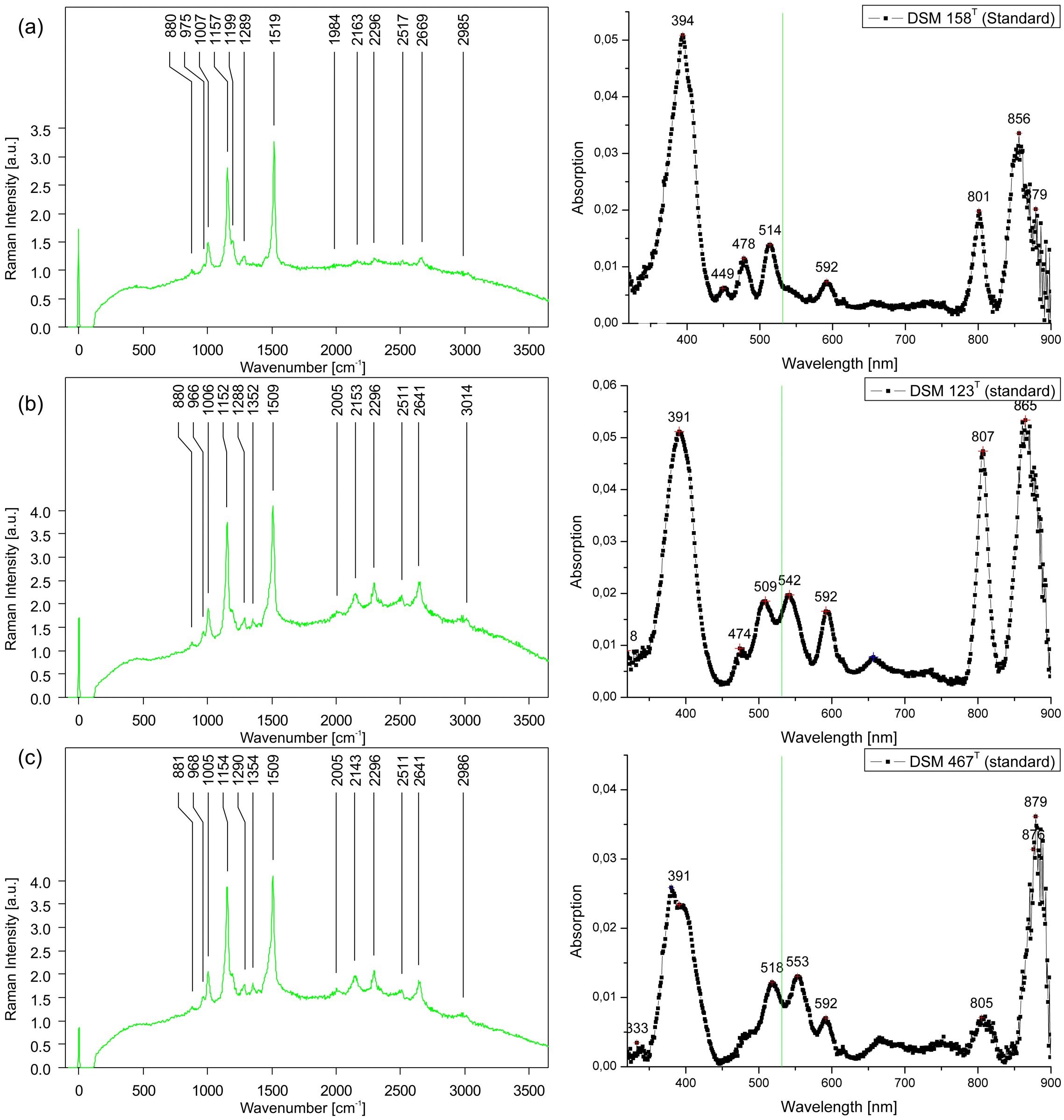

Figure 3.5: Raman spectrum at 532 nm excitation, normalized to [1501, 1542] (DSM 158) or [1491, 1532] (DSM 123, DSM 467) respectively (left), and absorption spectrum (right) of native *Rhodobacter sphaeroides* DSM 158^T (a), *Rhodopseudomonas palustris* DSM 123^T (b), and *Rhodospirillum rubrum* DSM 467^T (c). The Raman excitation wavelength is marked green in the absorption spectra. Raman excitation: 532 nm at 2.8 MW/cm^2 for 0.1 s.

The Raman and absorption spectra of the native cultures of *Rhodobacter sphaeroides* DSM 158, *Rhodopseudomonas palustris* DSM 123, and *Rhodospirillum rubrum* DSM 467 are given in Fig. 3.5. As can be seen, the absorption spectra of all three cultures show characteristic maxima of **bacteriochlorophyll-a** (Bchla) and **carotenoids**. The absorption bands at 392 ± 2, 592 ± 2, as well the maxima centered around 804 and 865 nm are all associated with Bchla and its associated bacteriopheophytins. An additional weak absorption band at 537 cm^{-1} reported by Eads et al. [2000] is likely masked by the intense absorption of the carotenoids in the same region. The separation of the two absorption maxima above 800 nm is known to be species sensitive and stems from the two main locations of Bchla within the light harvesting complexes: the absorption maxima near 800 nm is caused by the Bchla on the cytoplasma side, whereas the molecules associated parallel to the transmembrane helices of the light harvesting antenna absorb above 850 nm [Cogdell et al., 2006].

In addition, all three cultures show absorption maxima between 450 and 570 nm, associated with specific carotenoids. The absorption spectrum of *Rhodobacter sphaeroides* **DSM 158** (Fig. 3.5(a)) has maxima at 449, 478, and 514 nm, associated with spheroidenone. Whereas the culture of *Rhodopseudomonas palustris* **DSM 123** (Fig. 3.5(b)) shows absorption maxima at 474, 509, and 542 nm, indicative of a mixture of spirilloxanthin and 2-keto-spirilloxanthin. The absorption spectrum of *Rhodospirillum rubrum* **DSM 467** (Fig. 3.5(c)) showed only two distinct bands at 518 and 553 nm, identified as a 2-keto-spirilloxanthin. All absorption spectra above were associated according to Britton [1995].

The presence of **spheroidenone** and **2-keto-spirilloxanthin** in the cultures of *Rhodobacter* and *Rhodospirillum* instead of spheroidene and spirilloxanthin (see 2.5.2) is expected. Shneour [1962] showed that a rapid change from the main carotenoid spheroidene to its 2-keto derivative spheroidenone takes place within 30 min after cultures of previously anoxic growing *Rhodobacter* are exposed to oxygen. The same can be expected in cultures of *Rhodospirillum* with 2-keto-spirilloxanthin instead of spirilloxanthin being seen in its absorption spectrum. DSM 123 was the first culture measured after filling the cuvettes with bacterial solution. This may explain why spirilloxanthin was detected along its 2-keto derivative in *Rhodopseudomonas*. The rapid change of the main carotenoid was not completed yet.

Resonance Raman spectroscopy provides primarily information about the conjugated backbone of a carotenoid, but not about its non-conjugated end groups [Koyama, 1995]. Therefore, it is not necessary for the scope of this work to distinguish between the derivatives seen in oxygenated bacterial cultures and the main carotenoids expressed in undisturbed cultures and listed in literature. From here on the **carotenoids expressed by the bacteria** will be listed by their main form **as found in the undisturbed culture**:

- **spheroidene** in *Rhodobacter sphaeroides* DSM 158
- **spirilloxanthin** in *Rhodopseudomonas palustris* DSM 123 and *Rhodospirillum rubrum* DSM 467.

All carotenoids seen in the cultures of DSM 158, DSM 123, and DSM 467 are at least pre-resonant chromophores for an excitation with 532 nm. Bchla and its associated pheophytins are confirmed. However, its relevant absorption band at 537 cm^{-1} is not visible within the recorded absorption spectra.

The Raman spectra of all three cultures validate these results. The short recording time – 0.1 s per spectrum for bacteria expressing carotenoids – further suppressed Bchla and heme signals, typically recorded with 0.5 seconds and more.

The **resonant Raman spectrum** of *Rhodobacter sphaeroides* **DSM 158** (Fig. 3.5(a)) shows the strongest lines at 1,519, 1,157 and 1,007 cm^{-1} (order by intensity) and additional, but considerably weaker lines at 880, 975, 1,199, and 1,289 cm^{-1} all associated with spheroidene. Additional Raman lines at 1,984, 2,163, 2,296, 2,517, 2,669, and 2985 cm^{-1} are due to higher order processes.
The resonant Raman spectrum of *Rhodopseudomonas palustris* **DSM 123** has dominant lines at 1,509, 1,152, and 1,006 cm^{-1} (order by intensity) and weaker lines at 880, 966, 1,152, 1,288, and 1,352 cm^{-1}. Broadened lines due to higher order processes are seen at 2,005, 2,153, 2,296, 2,511, 2,641, and 3,014 cm^{-1}.
The spectrum of *Rhodospirillum rubrum* **DSM 467** with its dominant lines at 1,509, 1,154, and 1,005 cm^{-1}(order by intensity) and additional lines at 881, 968, 1,154, 1,290, and 1,354 cm^{-1}is within the spectral accuracy of the setup (± 1 cm^{-1}) identical to that of *Rhodopseudomonas*. A larger discrepancy is only seen in a single broadened band at 2,153 cm^{-1} (2,143 respectively).

The (resonant) **Raman spectrum of the mutant *Rhodobacter sphaeroides* DSM 2340** is given in Fig. 3.6 in comparison to that of its unchanged relative DSM 158 expressing spheroidene. The recognizable lines in the Raman spectrum of DSM 2340 are at 606†, 697 752†, 925†, 1,001, 1,130‡, 1,177‡, 1,233*, 1,312*‡, 1,340†, 1,458, and 1,588‡ cm^{-1} within the fingerprint region of 600 - 1800 cm^{-1}. The four strongest lines within the fingerprint region are (in descending order of intensity): 752†, 1,130‡, 1,588‡, and 1,312‡ cm^{-1}. The characteristic „shark fin" at 2,942 cm^{-1} belongs to unresolved CH-stretching modes seen in most cytochrome-c based Raman spectra of bacteria.

As expected, the Raman spectrum of DSM 2340 contains multiple components. The Raman lines marked with a (†) are within the spectral accuracy range of the spectrum of **cytochrome-c** at 530.9 nm excitation as reported and analysed by Hu et al. [1993]. Lines marked with (‡) are associated specifically with the **cytochrome-cbb**$_3$ complex of *Rhodobacter* by Varotsis et al. [1995], whose work covers the range of 1,100 to 1,850 cm^{-1}. Lines marked with a (*) are within the spectral accuracy of the spectrum recorded of 98 % pure cytochrome-c from bovine heart (see 3.2.3). The weak lines at 1,458 and 1,233 cm^{-1} are also associated with **bacteriopheophytins** [Eads et al., 2000]. In addition, the direct comparison to DSM 2340s unmutated relative DSM 158 (see Fig. 3.6) also **confirms the absence of the respective carotenoids in DSM 2340**.

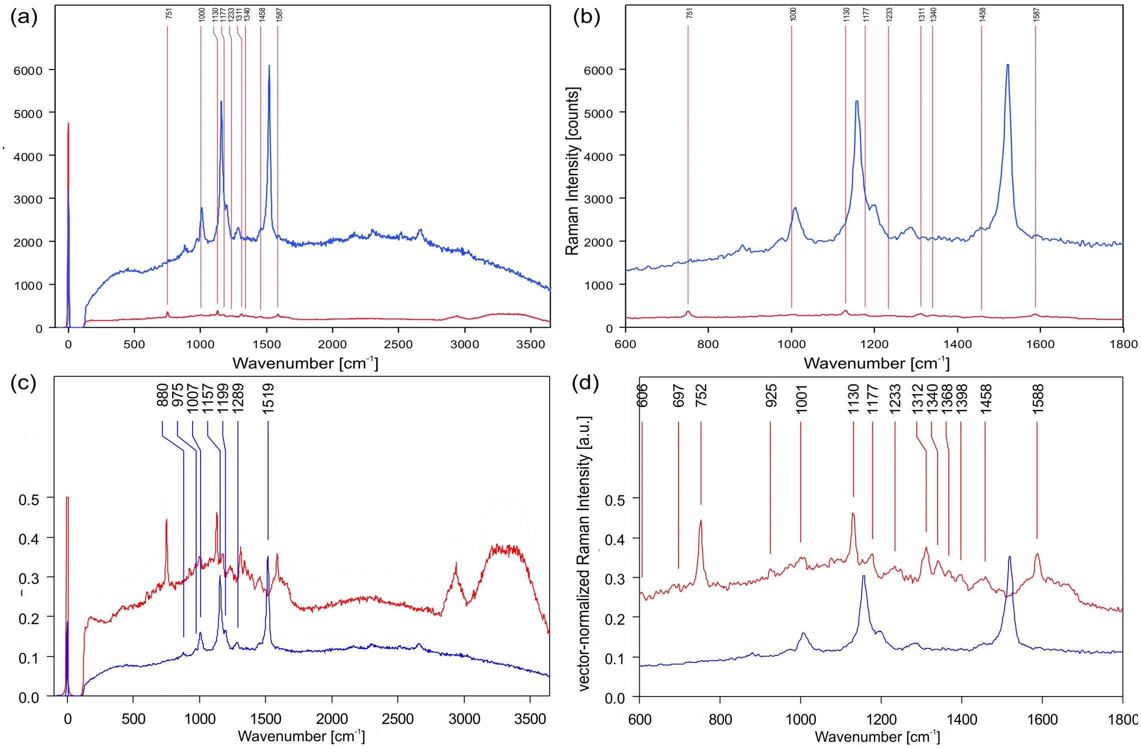

Figure 3.6: Resonant Raman spectrum of native *Rhodobacter sphaeroides* DSM 158^T (blue) and its carotenoids-free mutant DSM 2340^T (red): full spectra as recorded (a), fingerprint as recorded (b), vector-normalized full spectra (c) and vector-normalized fingerprint (d). Raman excitation: 532 nm at 2.8 MW/cm^2 for 0.5 s (DSM 2340) or 0.1 s (DSM 158).

3.2.3 *Nitrosomonae*: cytochrome-c

The cultures of *Nitrosomonas* used in this work – *Nitrosomonas communis* Nm-02, *Nitrosomonas europaea* Nm-50 and Nm-53, and *Nitrosomonas eutropha* Nm-57 – did not reach cell densities sufficient for absorption spectroscopy in vivo. However, the sole energy source for autotrophic nitrifying bacteria such as *Nitrosomonas* is aerobic ammonia oxidization, the electron transport of which relies heavily on cytochromes-c [Pettigrew and Moore, 1987]. Therefore, the Raman spectra of *Nitrosomonas* were analyzed and compared to the Raman spectrum of the pure chromophore obtained from two different sources: cytochrome-c from *Saccharomyces cerevisiae* with a purity of over 85 % and from bovine heart with the highest available purity of over 98 %. The resonance condition was confirmed with the protein from *S. cerevisiae* (Fig. 3.7).

The **absorption spectrum of cytochrome-c** recorded from cytochrome-c of *S. cerevisiae* in neutral aqueous solution (pH = 7) is given in Fig. 3.7. As can be seen, the most intense absorption band lies at 410 nm and a much weaker band is centered around 530 nm, both bands result primarily from the porphyrin in the heme-group [Moore and Pettigrew, 1990]. It is noteworthy, that the cytochromes-c expressed by Nitrosomonas are reported to have soret bands between 407 and 410 nm and a Q-band centered around 530 nm in their ferrous state. The latter resolves to 523 ± 1 nm and 552 ± 2 nm absorption bands in the ferric state, and absorption intensities for the ferrous and the ferric state

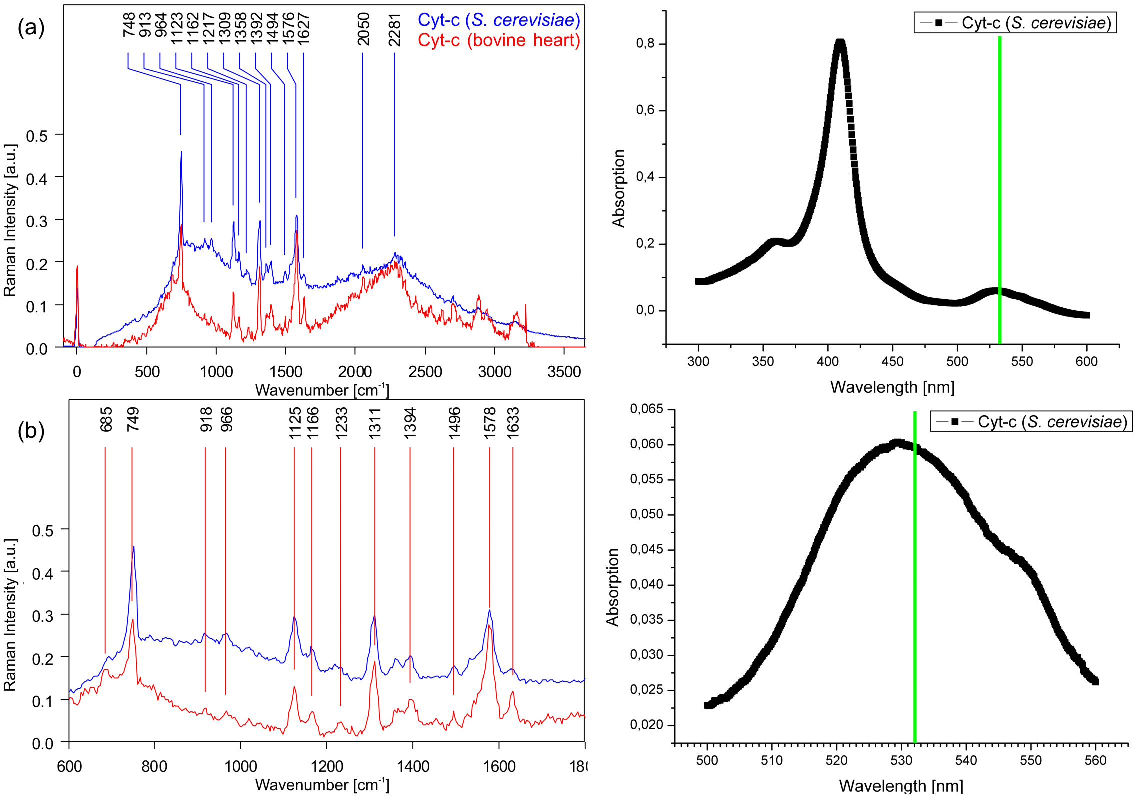

Figure 3.7: Raman spectrum at 532 nm excitation (left), and absorption spectrum (right) of cytochrome-c of *Saccharomyces cerevisiae* (purity ≥ 85 %) and of bovine heart (purity ≥ 98 %). The Raman excitation wavelength is marked green in the absorption spectrum. Raman excitation: 532 nm at 0.5 MW/cm^2 for 0.5 s.

match near 532 nm, allowing for excitation of both states with similar efficiency [Pettigrew and Moore, 1987, Hu et al., 1993].

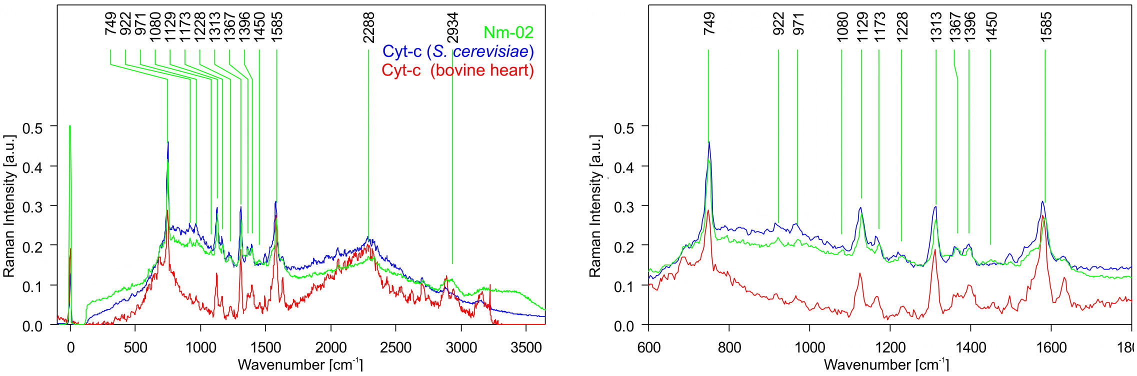

Figure 3.8: Raman spectra of native *Nitrosomonas communis* Nm-02 and cytochrome-c from *Saccharomyces cerevisiae* (purity ≥ 85 %) and from bovine heart (purity ≥ 98 %). Full spectra (left), fingerprint region (right). Excitation: 532 nm.

The **Raman spectrum of cytochrome-c** (Fig. 3.7) originating from *S. cerevisiae* (purity: ≥ 85 %) contains the following lines in the fingerprint region: 748, 913, 964, 1,123, 1,162, 1,217, 1,309, 1,358, 1,392, 1,494, 1,576, and 1,627 cm^{-1}. The Raman lines seen in the spectrum of cytochrome-c from bovine heart (purity: ≥ 98 %) are at 685, 749, 918, 966, 1,125, 1,166, 1,233, 1,311, 1,394, 1,496, 1,578, and 1,633 cm^{-1}. These spectra are identical within the spectral accuracy of the setup in all lines save the additional line at 684 cm^{-1} seen in the spectrum of bovine cyt-c and the line at 1,358 cm^{-1} in the spectrum recorded from cyt-c of *S. cerevisiae*. The seemingly large shift of the weak lines at 913 and 1,162 cm^{-1} are caused by the OPUS band search routine. The spectra are virtually superposable in these lines (compare Fig. 3.8 (right)).

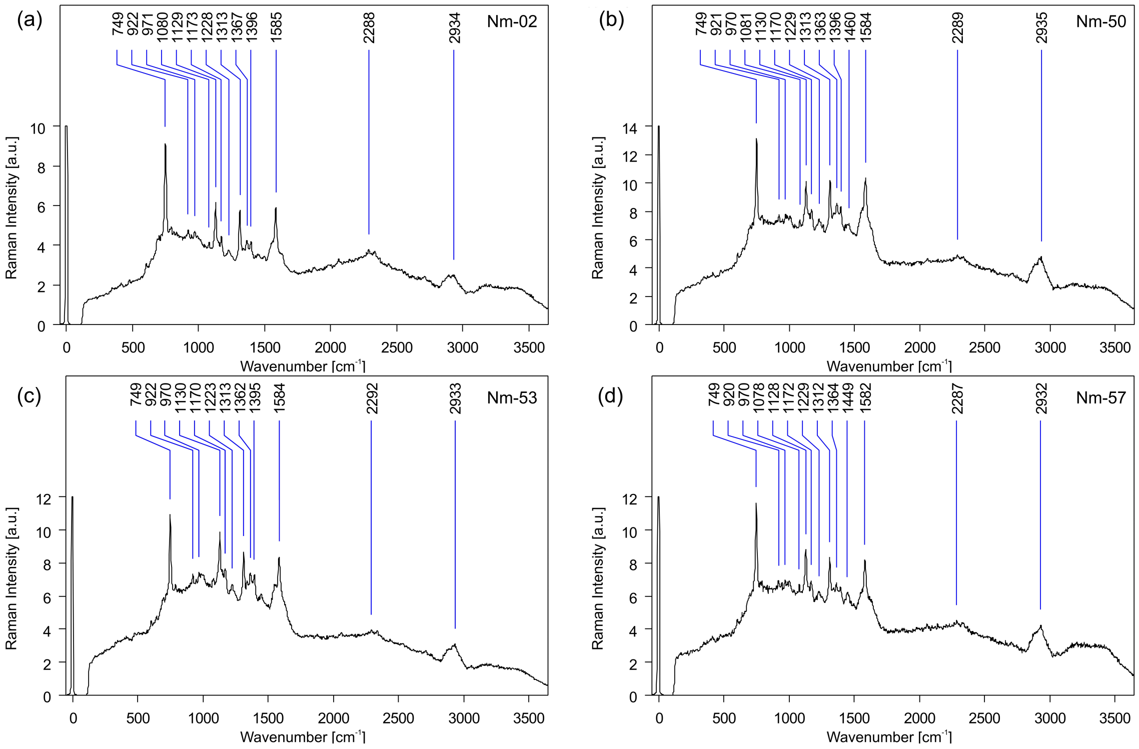

Figure 3.9: Raman spectra of native *Nitrosomonas communis* Nm-02 (a), *Nitrosomonas europaea* Nm-50 (b) and Nm-53 (c), and *Nitrosomonas eutropha* Nm-57 (d). Raman excitation: 532 nm at 2.8 MW/cm^2 for 0.5 s.

As expected the **Raman spectra recorded from native samples of *Nitrosomonas*** (*N. communis* Nm-02, *N. europaea* Nm-50 and Nm-53, *N. eutropha* Nm-57)(Fig. 3.9) are very similar. The Raman frequencies and relative intensities of the lines within the fingerprint region are given in Tab. 3.1.

The spectra of the *Nitrosomonas* strains are notably **shifted by up to 7 cm^{-1}** to higher wavenumbers when compared to the Raman spectrum of pure cytochrome-c from bovine heart (Fig. 3.8), with the line at 1,233 cm^{-1} being the exception with a downshift of 5 cm^{-1} on average. Shifts of this size were already reported by Shelnutt et al. [1979] for the resonance Raman spectra of cyt-c extracted from different sources.

The **most intense and stable line** seen in all spectra is the pyrrole breathing mode ν_{15}, which is fixed at **749 cm^{-1}** in all *Nitrosomonas* spectra and shifts only by -1 cm^{-1} in cyt-c from bovine heart. The Raman intensities in Tab.3.1 are given in relation to this line.

Variations in the Raman frequencies exceeding the spectral accuracy in the spectra of different *Nitrosomonas* strains are only seen in four lines: ν_{30} (1,172 ± 3 cm^{-1}; rel. intensity: ≤ 0.1), ν_{23} (1,079 ± 3 cm^{-1}; 0.1 (0.2 in case of Nm-50)), ν_{13} (1,233 ± 6 cm^{-1}; $\leq$ 0.1 (0.2 in case of Nm-50)), and ν_{19} (1,584 ± 3 cm^{-1}; 0.6). Of these, only ν_{19} at 1,584 cm^{-1}

Raman spectra of *Nitrosomonas*									
	Raman frequencies [cm^{-1}]					relative intensities			
mode†	bovine heart	Nm-02	Nm-50	Nm-53	Nm-57	Nm-02	Nm-50	Nm-53	Nm-57
ν_{15}	749	749	749	749	749	1.00	1.00	1.00	1.00
ν_{46}	918	922	921	922	920	0.09	0.10	0.12	0.09
$\nu_{C_c-C_d}$	966	971	970	970	970	0.08	0.07	0.08	0.07
ν_{23}	–	1,080	1,081	–	1,078	0.06	0.10	–	0.09
ν_{22}	1,125	1,129	1,130	1,130	1,128	0.50	0.49	0.60	0.50
ν_{30}	1,166	1,173	1,170	1,170	1,172	0.11	0.17	0.12	0.13
ν_{13}	1,233	1,228	1,229	1,223	1,229	0.05	0.18	0.09	0.08
ν_{21}	1,311	1,313	1,313	1,313	1,312	0.46	0.45	0.49	0.40
ν_{20}	1,394	1,396	1,396	1,395	–	0.08	0.09	0.10	–
‡	–	–	1,460	–	1,449	–	0.10	–	0.13
ν_{19}	1,578	1,585	1,584	1,584	1,582	0.59	0.77	0.69	0.58

† assignments according to Hu et al. [1993].

‡ line observed in Ferri-cytc (Fe^{3+}) but not discussed (Fig. 17 in Hu et al. [1993]).

Table 3.1: Raman lines and intensities in relation to the most stable line at 749 cm^{-1}in the spectra of *Nitrosomonas* Nm-02, Nm-50, Nm-53, and Nm-57 given in Fig. 3.9.

belongs to the four strongest lines in the spectrum. The comparatively large variation of 6 cm^{-1} seen in the line at 1,233 cm^{-1} breaks down to 1 cm^{-1}, if the extreme value found in the spectrum of Nm-53 is excluded. In addition, ν_{19} varies only by 1 cm^{-1} (within spectral accuracy) among *Nitrosomonas communis* and *N. europaea*, the variation exceeding the spectral accuracy is between these and *N. eutropha*.

The line at 1,080 cm^{-1}, visible in the *Nitrosomonas* spectra (it did not exceed the noise in the spectrum of Nm-53), is not visible in the spectrum of cyt-c from bovine heart. However, it is reported by Hu et al. [1993] in their assignment of the resonance Raman spectrum of cytochrome-c in natural abundance at 530.9 nm excitation.

Interestingly, the line at 1,460 cm^{-1} reported only in the spectra of ferric cytochromes-c (‡ in Tab.3.1) was detected in the reference spectra of *Nitrosomonas eutropha* and *N. europaea* Nm-50. It is visible by comparison in the spectra of Nm-02 and Nm-53 as well, but did not exceed the overall noise threshold to be marked. The existence of cytochromes-c in ferric state (Fe^{3+}) is a strong **indication of the active metabolism** of the bacteria at the time of the measurement [Pettigrew and Moore, 1987].

Notable **differences** are seen **in the relative intensities** of the Raman lines within the spectrum. The four strongest lines in order of intensity in the Nitrosomonas spectra are ν_{15}, ν_{19}, ν_{22}, and ν_{21} (see Tab.3.2). While this order does not change in either of the spectra recorded from the various strains, the actual relation varies with the largest change seen in $\nu19$ in the spectrum of Nm-50 with almost 80 % of the intensity of the reference ν_{15} (instead of the 60 % seen in the other spectra) and ν_{22} being 10 % less intense in Nm-57 than in the spectra of the other strains. However, none of these differences are

Raman line intensities of *Nitrosomonas*				
mode†	Nm-02	Nm-50	Nm-53	Nm-57
ν_{15}	1.00	1.00	1.00	1.00
ν_{19}	0.59	0.77	0.69	0.58
ν_{22}	0.50	0.49	0.60	0.50
ν_{21}	0.46	0.45	0.49	0.40

† assignments according to Hu et al. [1993].

Table 3.2: Relative intensity comparison of the four strongest Raman lines in the spectra of *Nitrosomonas* Nm-02, Nm-50, Nm-53, and Nm-57 given in Fig. 3.9. Marked intensities differ by at least 5 % from those seen in Nm-02.

large enough to be recognized by the naked eye without either a direct comparison or a precise analysis of the spectra.

3.2.4 Bacteria fact sheet

bacterial strain	confirmed chromophores	spectra	comments
Purple non-sulfur bacteria			
DSM 123	spirilloxanthin$^{\dagger\Diamond\Box}$ cyt-cbb$_3^{\Box}$	Fig. 3.5(b)	*Rhodopseudomonas palustris* cell size: 1.2 μm $^{\Box}$
DSM 158	spheroidene$^{\dagger\Diamond\Box}$ cyt-cbb$_3^{\Box}$	Fig. 3.5(a)	*Rhodobacter sphaeroides* cell size: 1.0 μm $^{\Box}$
DSM 467	spirilloxanthin$^{\dagger\Diamond\Box}$ cyt-cbb$_3^{\Box}$	Fig. 3.5(c)	*Rhodospirillum rubrum* cell size: up to 5 μm $^{\Box}$
DSM 2340	cyt-cbb$_3^{\Diamond\Box}$	Fig. 3.6	*Rhodobacter sphaeroides* (mutant of DSM 158) reference with S/N = 11
Nitrifiers			
Nm-02	cyt-c$^{\ddagger\Diamond\Box}$	Fig. 3.9(a)	*Nitrosomonas communis*
Nm-50	cyt-c$^{\ddagger\Diamond\Box}$	Fig. 3.9(b)	*Nitrosomonas europaea* active metabolism confirmed (ferri-cytochrome-c detected)(Fig. 3.9 and Tab.3.1)

Nm-53	cyt-c$^{\ddagger\Diamond\Box}$	Fig. 3.9(c)	*Nitrosomonas europaea*
Nm-57	cyt-c$^{\ddagger\Diamond\Box}$	Fig. 3.9(d)	*Nitrosomonas eutropha* active metabolism confirmed (ferri-cytochrome-c detected) (Fig. 3.9 and Tab.3.1) carbonate particulates in the culture$^{\Diamond}$ (see Fig. 3.3)

confirmed with

◊ Raman spectroscopy † absorption spectroscopy on native culture

‡ compared to pure chromophore □ literature

3.3 Effects of Sample Preparation

Preparation is a necessary step for most measurements of biological and other samples. It starts at taking samples from their initial environment and placing it under the microscope or may include extended chemical and physical treatment. When measuring native, i.e. living, bacteria grown in liquid culture flasks, the bacteria already face a change in living conditions by being taken from the large volume of the culture flask to the very limited volume under a cover slip. Gaseous metabolism products accumulate faster, nutrient levels are decreasing, and the larger surface area compared to the volume of the medium may increase adhered populations rather than free floating single cells. All this in addition to the fact that native samples, their metabolism, growth, and overall motility already have a large, inherent variability.

3.3.1 Effects of Fixation

Fixation is one of the most common procedures in biological and related sciences to address the problem of handling native cells. It allows biological aggregates such as tissues or bacterial communities – no matter if obtained from natural habitats or cultured from clinical samples – to be stored over extended periods of time while remaining unaltered regarding the respective properties under study. In addition, many analytical methods regularly applied to biological samples require fixation. Considering the vast number of analytical methods available, ranging from the extraction of specific molecules or organelles from single cells to the preservation of the spatial structure of complex cell aggregates, it is unsurprising that a multitude of fixation procedures has been developed. Many of these fixation procedures are highly invasive, leaving little to no doubt of severely affecting subsequent Raman measurements by rendering the spectra of fixed samples incomparable to those of native samples.

Among the least invasive fixation methods widely employed in many biological and medical procedures are ethanol fixation (EtOH), (para)formaldehyde fixation (PFA), and gentle heat fixation as described in 2.5.3. These were examined for compatibility with subsequent resonant Raman measurements.

In order to differentiate between effects of the preparation onto the cells themselves and effects due to changed adsorption or cell dimensions, three different fast growing species of purple non-sulfur bacteria with similar chromophores but different cell sizes were used: *Rhodobacter sphaeroides* DSM 158^T, *Rhodopseudomonas palustris* DSM 123^T, and *Rhodospirillum rubrum* DSM 467^T, all of which were cultured as described in 2.5.2. Chromophores (as confirmed in 3.2) and cell sizes are given in Table 3.4.

Bacteria used for Fixation Analysis

species	cell size [μm]	main chromophore
Rhodobacter sphaeroides	1.0	spheroidene
Rhodopseudomonas palustris	1.2	spirilloxanthin
Rhodospirillum rubrum	5.0	spirilloxanthin

Table 3.4: Purple non-sulfur bacteria cultures: cell sizes and chromophores.

Figure 3.10 shows the resonant Raman spectrum of *Rhodopseudomonas palustris* (a) and *Rhodospirillum rubrum* (b) native and fixed with ethanol, formaldehyde, or heat (70 °C) respectively, recorded from samples mounted on uncoated microscope slides. For comparability, all spectra were normalized to [1,419, 1,532] cm^{-1}, holding the dominant peak of spirilloxanthin at 1,509 cm^{-1}. A similar comparison for *Rhodobacter sphaeroides* DSM 158^T is part of subsection 3.3.2.

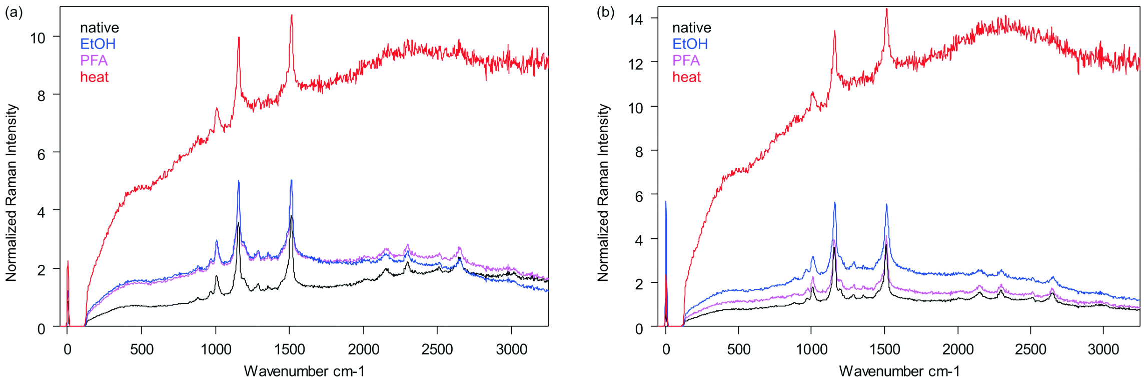

Figure 3.10: Resonant Raman spectrum of *Rhodopseudomonas palustris* 123 (a) and *Rhodospirillum rubrum* 467 (b) native or fixed with ethanol, paraformaldehyde, or heat (70 °C), respectively, and mounted on uncoated microscope slides. (Figure first published in Kniggendorf et al. [2011b].)

As can be seen, even **gentle heat fixation** is clearly detrimental to subsequent Raman measurements. It causes the Raman spectrum to deteriorate with a strongly increased background and a complete loss of the weaker Raman lines in the background noise independent of bacteria sample. Only the three dominant Raman lines of spirilloxanthin are clearly visible, of which only the two strongest lines were allocated correctly. The third strongest line at 1,004 cm^{-1} is broadened and shifted by 10 cm^{-1} to 1,014 cm^{-1}.

In contrast, the fixatives **EtOH** and **PFA** both preserve the Raman spectrum of the bacteria well. Shape, spectral position, and relative intensity of the Raman lines are unchanged in comparison to the spectrum of native samples. However, signal as well as background intensity is diminished by 25 to 50 % in PFA fixation compared with when the sample was native or fixed with EtOH. Although, this overall reduction in intensity has no influence on the quality of the spectrum itself, it may prove a problem in case of weak Raman spectra or less sensitive detectors.

Also of importance is the time a sample is exposed to the fixative. Fig. 3.11 shows **the effects of extended fixation** on the resonant Raman spectrum of *Rhodobacter sphaeroides* DSM 158^T. As can be seen, EtOH fixation causes additional fluorescent background in the spectrum, the intensity of which is increasing with the time the sample is exposed to the fixative. The overall signal intensity and the spectral position of the Raman lines is not affected within the first 24 h. However, the peaks of the intense Raman lines at 1,007, 1,157, and 1,519 cm^{-1}, associated with the carotenoid spheroidene, are slightly broadening with time. The Raman line at 1,157 cm^{-1} shows this most clearly. This may be due to EtOH being a solvent to spheroidene. Since EtOH gradually replaces intercellular water, the spheroidene molecules as part of the bacterial light harvesting complexes come into increasing contact with their solvent.

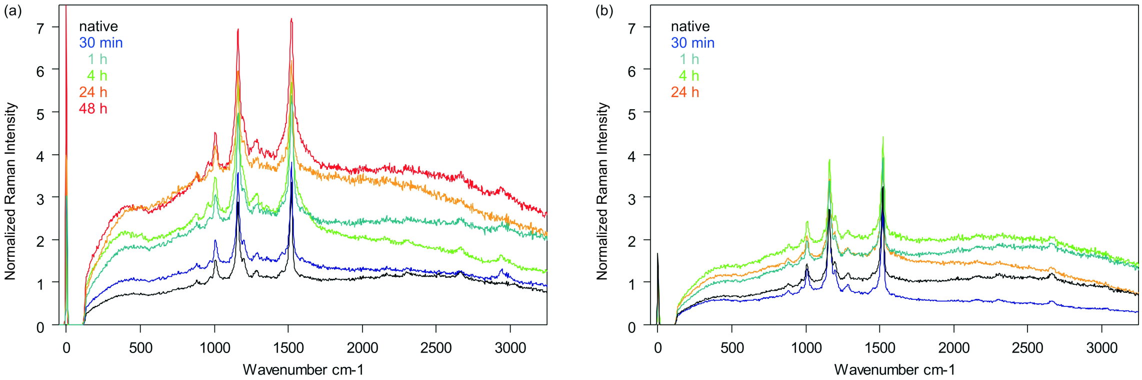

Figure 3.11: Effects of extended ethanol (a) and paraformaldehyde (b) exposure on the resonant Raman spectrum of *Rhodobacter sphaeroides* 158 mounted on uncoated microscope slides. The spectra of *Rhodobacter* fixed with ethanol for 4 and 24 hours show a different course above 1,600 cm^{-1} due to a different culture of the bacteria being used. The comparison with the spectrum of the corresponding native sample confirmed the variant course to be caused by the bacteria not the applied fixative. (Figure first published in Kniggendorf et al. [2011b].)

The resonant Raman spectrum of bacteria fixed with PFA for an extended period of time also shows an increased fluorescent background. However, this is due to a reduction in signal intensity rather than an increase in background intensity, which causes weaker Raman lines to be lost in the noise or below the detection threshold. In addition, the background intensity was fairly constant after 4 h. Since formaldehyde solution forms stable methylene bridges irreversibly linking primary amino and thiol groups with several other amino acid residues [Metz et al., 2004], it can be strongly assumed that the formation of all possible methylen bridges within the protein matrix of the cells is completed after 4 h and additional fixative exposure has no further effect on the samples.

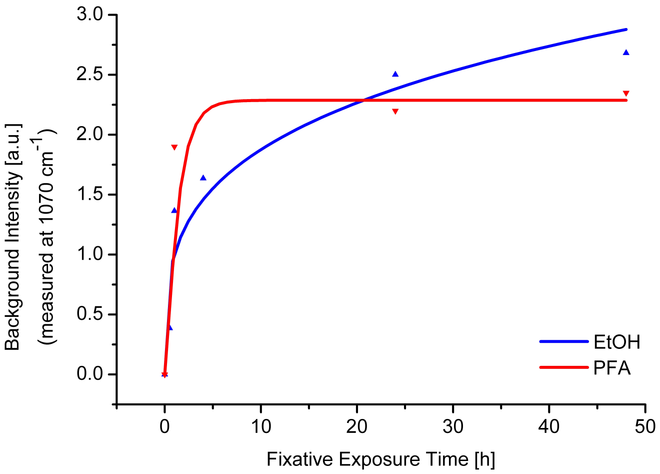

Figure 3.12: Development of fluorescent background intensity in the Raman spectrum of *Rhodobacter sphaeroides* 158 measured at 1,070 cm^{-1} as a function of the time the sample was exposed to the fixative. (Figure first published in Kniggendorf et al. [2011b].)

Figure 3.12 illustrates the effects of both fixatives by showing the additional background intensity at 1,070 cm^{-1} in the normalized spectra as a function of the fixation time. As can be seen, the additional background caused by EtOH fixation follows a root function, whereas the background from PFA resembles a hyperbolic tangent. This indicates clearly that for short time fixation of less than a day, EtOH may be a preferable fixative, whereas in case of required longer exposure times, the results obtained with PFA are superior.

3.3.2 Effects of adhesive coatings

Cell adhesive coatings are an important aid for preparing samples of cells with little surface affinity of their own. Poly-L-lysine has been used as a highly adhesive coating on microscope slides and other laboratory equipment for more than thirty years. Its polycationic molecules adsorb strongly to various carrier materials such as glass, quartz, or various plastics, providing cationic surface sites to combine with the anionic sites on outer cell membranes. Cells attached to a poly-L-lysine coating spread and flatten along the surface. It has been shown that the adhesion is strong enough to withstand most fixation baths, though an ethanol acetate solution of three to one was reported to cause partial cell detachment [Mazia et al., 1975]. A poly-L-lysine coating is a standard feature of many readily available high-quality microscope slides these days. However, especially in combination with PFA fixation (see 2.5.3) it has significant influence on subsequent resonant Raman measurements.

As can be seen in Figure 3.13, the use of poly-L-lysine coated microscope slides in comparison to uncoated slides has little to no discernable effect on the Raman spectrum of native samples or samples fixed with EtOH or heat, but it is clearly detrimental to the Raman spectrum of samples fixed with PFA.

All spectra of PFA fixed samples recorded on poly-L-lysine coated slides show a distinct loss of signal and background intensity with increasing wavenumbers. The weaker Raman lines above 1,800 cm^{-1} are typically lost entirely, while the Raman lines at 880 and 1,289 cm^{-1} are still clearly visible. A comparative spectrum analysis (see 2.3.2) with the

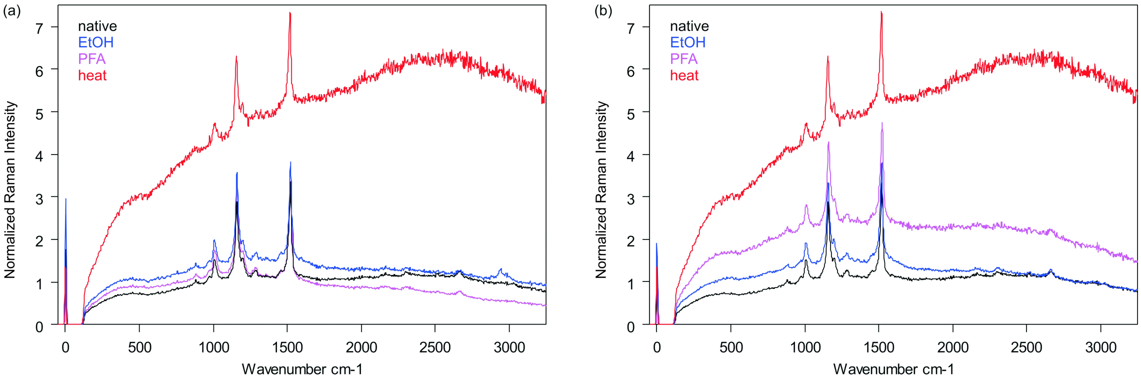

Figure 3.13: Resonant Raman spectrum of *Rhodobacter sphaeroides* 158 native and fixed with ethanol, paraformaldehyde, or heat (70 ℃) respectively. Samples were mounted on an uncoated microscope slide (a) or a microscope slide coated with poly-L-lysine (b). (Figure first published in Kniggendorf et al. [2011b]).

analysis software settings suitable for the Raman spectrum of a native sample caused an average of 20 or more false positives throughout the spectrum. The same happened with the software settings suitable for a PFA-fixed sample mounted on an uncoated microscope slide.

In addition, for PFA-fixed *Rhodobacter* 158, the signal intensity throughout the spectrum is 50 % or less of that typically detected on uncoated slides. In the normalized spectra, this shows as an increase in background and noise compared with the measurement on uncoated slides. The same can be seen to a lesser extent in the Raman spectrum of PFA-fixed *Rhodopseudomonas*, which yields 20 % loss on poly-L-lysine coated slides, whereas no such effect is seen in the Raman spectrum of *Rhodospirillum* (see Fig. 3.14 for *Rhodobacter* 158 and Fig. 3.15 for *Rhodopseudomonas* (a) and *Rhodospirillum* (b)).

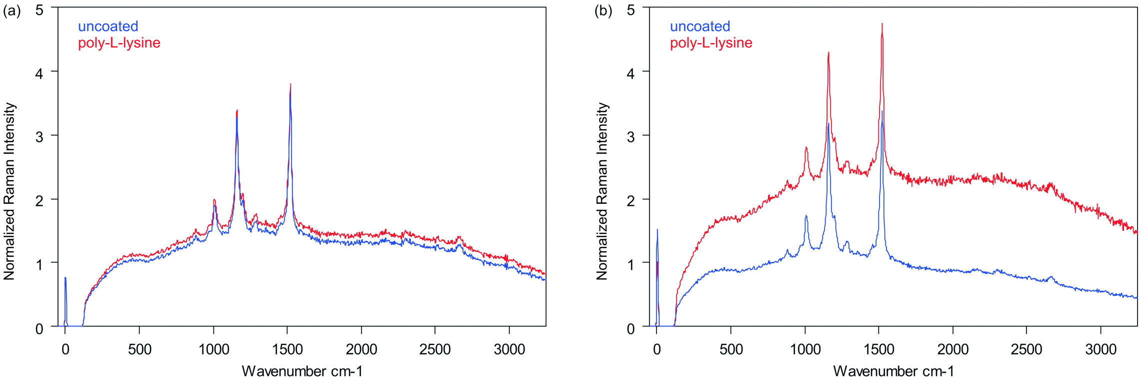

Figure 3.14: Resonant Raman spectra of native and PFA fixed *Rhodobacter sphaeroides* 158 mounted on uncoated (a) and poly-L-lysine coated (b) microscope slides. (Figure first published in Kniggendorf et al. [2011b])

At this point in time, I may only speculate about the reason for this interesting effect restricted to the combination of PFA fixation and poly-L-lysine coated slides. An increased interaction of the polycationic poly-L-lysine coating with anionic sites on the surface of PFA-fixed cells might be responsible. This increased interaction may be caused either by

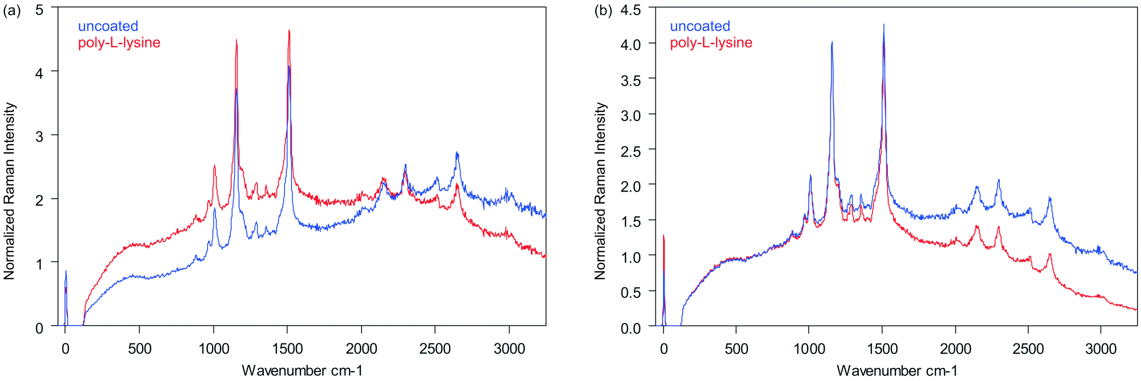

Figure 3.15: Resonant Raman spectrum of PFA-fixed *Rhodopseudomonas palustris* 123 (a) and *Rhodospirillum rubrum* 467 (b) mounted on uncoated and poly-L-lysine coated microscope slides. (Figure first published in Kniggendorf et al. [2011b]).

a decrease in cationic sites on the cell surface due to methylene bridges formed in the bacterial protein matrix, or by a higher affinity of methylene bridged proteins to L-lysine as reported for model peptides by Metz et al. [2004]. The latter may also be responsible for the loss in intensity specifically at higher wavenumbers independent of cell size.

In any case, the uneven loss of signal intensity from PFA fixed samples mounted on poly-L-lysine coated microscope slides causes a distortion of the recorded Raman spectrum that will severely affect subsequent analyses, especially in lieu of comparisons with native samples or samples treated with a different fixation protocol.

4 Spectral analysis with chromophore information

Normal Raman spectra may literally drown the analyst in information about the physical condition of the individual cell, its health, reproduction plans, and likely its last meal, making reliable identification of the cells difficult if not impossible. In contrast, resonance Raman spectra reduce the source of information from the whole bacterial cell to a specific chromophore component of the cell, which (in case of cytochrome-c) may give answers about identity, activity and even taxonomy (as far as it has been decided [Staley, 2006]) [Pettigrew and Moore, 1987].
However, one has to be aware that **bacteria often contain multiple chromophores**. For example, *Nitrosomonas europaea* is known to produce several cytochromes-c just for performing the oxidization of ammonia (one of which (c-554) even contains four heme-c instead of the common single heme). All these chromophores are subject to evolutionary change between strains [Pettigrew and Moore, 1987]. Differentiation and identification of bacteria strains based on purified specific types of cytochromes-c extracted from the bacteria was successfully demonstrated [Moore and Pettigrew, 1990]. However, whether or not this is possible with the resonance Raman spectra recorded from native cells containing all their chromophores was to be tested.
Therefore, the **variability of the spectra** recorded from native cells of the same bacterial strain was assessed and the spectral distances between spectra recorded from cells of different strains were determined (see 4.3). For this, the usability of hierarchical cluster analysis (HCA) as a means for determining the **spectral distances between individual (resonance) Raman spectra** was evaluated (see 4.1 and 4.2).

Parts of this chapter were previously published in Kniggendorf et al. [2011a] and Kniggendorf and Meinhardt-Wollweber [accepted for publication w.m.r.].

4.1 HCA algorithm assessment

Resonance Raman spectra are primarily chromophore spectra (compare section 3.1), which may be affected by different host environments. Therefore hierarchical clustering of biological samples based on resonance Raman spectra requires algorithms sensitive enough to handle spectra with a high intrinsic similarity due to a common chromophore in the presence of highly dissimilar spectra originating from other chromophores.

In order to test the available HCA algorithms for their ability to reliably handle resonant Raman spectra with various levels of intrinsic similarity, a set of six different bacterial strains producing three different main chromophores resonant to 532 nm excitation was used. Table 4.1 gives an overview of the used bacteria, including family, species and main chromophore. Spheroidene and spirilloxanthin were chosen as similar but not identical chromophores, because these carotenoids have the same function in the photoreaction centers and are specific to the respective bacteria [Britton, 1998].

Bacteria used for HCA Algorithm assessment			
family	species	strain	main chromophore
purple non-sulfur bacteria	*Rhodobacter sphaeroides*	DSM 158	spheroidene
	Rhodopseudomonas palustris	DSM 123	spirilloxanthin
	Rhodospirillum rubrum	DSM 467	spirilloxanthin
Nitrosomonae	*Nitrosomonas communis*	Nm-02	cytochrome-c
	Nitrosomonas europaea	Nm-50	cytochrome-c
		Nm-53	cytochrome-c

Table 4.1: Bacteria strains used for assessing HCA algorithms: family, strain, and main chromophore.

While cyt-cbb$_3$ is also present in purple non-sulfur bacteria (see 3.2.4), it requires significantly longer excitation times for recording resonant Raman spectra of similar intensity than the aforementioned carotenoids and thus does not affect the resonant Raman spectra of carotenoids recorded from purple non-sulfur bacteria. See 3.2 for details of the spectra and confirmation of the chromophores.

4.1.1 Data preparation and test procedures

In typical measurements of biological samples, only a single spectrum can be obtained from an individual cell, therefore each algorithm was used on a set of single spectra contributing to the respective reference spectra (see 3.2.1). In addition, a set of six high-quality spectra was clustered with each algorithm for reference.

Hierarchical cluster analyses were performed with the additional software module OPUS IDENT for OPUS version 5.5 (see section 2.3.1) incorporating the algorithms in eqs. (2.8) – (2.14). The clustering results were analyzed on the level of four clusters with respect to the spectral distance between clusters and the spectral relation of the examined bacteria species grouped into the clusters. For example: *Rhodobacter* holding spheroidene forming cluster (1) and *Rhodopseudomonas* and *Rhodospirillum*, both with spirilloxanthin, together being grouped into cluster (2). In addition, the number of spectra being assigned to a wrong cluster was taken into account, independent of spectral distance or spectral relation of the clusters.

In contrast to the algorithms in eqs. (2.8) – (2.13), the Ward algorithm (eq. 2.14) does not compute the spectral distance between clusters. Instead it calculates the within cluster sum of squares (also called the error sum of squares) of every possible cluster [Ward, jr., 1963]. Clusters are then chosen so that this sum of squares within all clusters is minimized [Sharma, 2006]. Therefore, the so-called Heterogeneity H relates to the spectral distance D as used by the algorithms in eqs. (2.8) – (2.13) like

$$H(r,i) \sim D(r,i)^2 n(r+i) \tag{4.1}$$

with $n(r+i)$ being the number of spectra included in the clusters r and i. Therefore the dendrogram calculated by the Ward algorithm is proportional to the weighted square of the spectral distances, rather than the spectral distances themselves. In order to achieve quantitative comparability between the results of the Ward algorithm and the algorithms in eqs. (2.8) – (2.13), the spectral distance D was calculated from the Heterogeneity H.

All spectra were prepared for HCA as follows: The spectral region below 600 cm^{-1} was excluded, because it does not hold any of the prominent Raman peaks of the interesting chromophores. The spectral region above 1800 cm^{-1} was excluded, because it does not add to the information about the investigated chromophores (compare section 3.1). Spectra were then vector normalized to the remaining fingerprint region of 600 – 1800cm^{-1} and subjected to HCA.

Resonance Raman spectra of single bacterial cells (single spectra) with an S/N between 10 and 20 were used for hierarchical cluster analysis. Single spectra of lower or higher S/N were excluded to prevent spectrum quality becoming a clustering criterion superior to the spectral differences caused by the chromophores (see 4.2).

Reference spectra for each bacterial type strain were formed as described in 3.2.1 and had an S/N of approx. 100. Reference spectra taken from the same sample but from different cells showed less than 0.5% variance when compared with OPUS IDENT routine for spectral identity, giving a spectral distance of 0.11 or less when subjected to HCA.

The clustering results were analyzed on the level of four clusters with respect to the **spectral distance** between clusters and the **spectral relation** of the examined bacteria species grouped into clusters. In addition, the number of spectra assigned to a wrong cluster was taken into account, independent of spectral distance or spectral relation of the clusters.

4.1.2 Reference spectra clustering

Reference spectra as described in 3.2.1 were constructed for all six bacterial strains used in this analysis (see Tab.4.1). Figure 4.1 shows the carotenoid (a) and cytochrome-c (b)

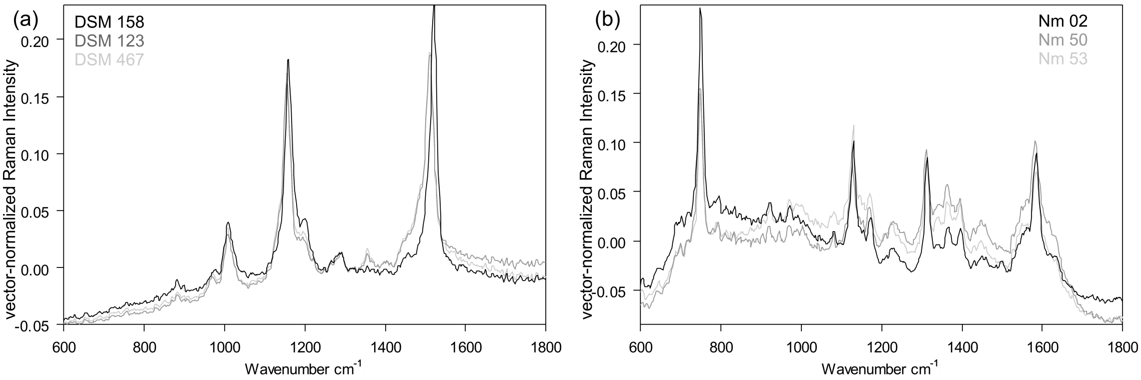

Figure 4.1: Reference spectra (averages of 100 single spectra of S/N ? 10 each) of (a) *Rhodobacter sphaeroides* DSM 158^T, *Rhodopseudomonas palustris* DSM 123^T, and *Rhodospirillum rubrum* DSM 467^T, and (b) *Nitrosomonas communis* Nm-02 and two strands of *Nitrosomonas europaea* (Nm-50 and Nm-53).(Figure first published in Kniggendorf et al. [2011a].)

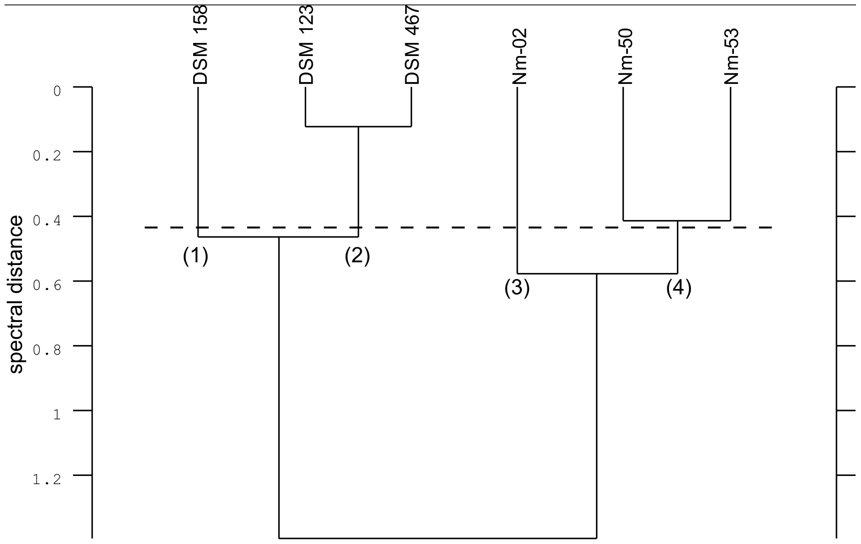

Figure 4.2: Reference dendrogram. All examined algorithms clustered the reference spectra as shown here. For the exact distances between clusters (1) and (2) – and (3) and (4), respectively – see table 4.2.(Figure first published in Kniggendorf et al. [2011a].)

based reference spectra as they were used for HCA. The dendrogram resulting from the hierarchical cluster analysis of the six reference spectra is given in Figure 4.2.

All applied HCA algorithms returned the same spectral relation between the tested bacteria: one branch of purple non-sulfur bacteria with *Rhodobacter* DSM 158^T in one cluster (1) and *Rhodopseudomonas* DSM 123^T and *Rhodospirillum* DSM 467^T grouped together in a second cluster (2), while the *Nitrosomonae* were collected in a second branch with *Nitrosomonas communis* Nm-02 separated in cluster (3) and the two strains of *Nitrosomonas europaea* Nm-50 and Nm-53 collected together in another cluster (4). The cluster labels (1) to (4) were assigned solely with respect to the bacteria primarily allocated to the clusters. The spectral distances found by the investigated algorithms are given in Table 4.2.

Reference spectra clustering				
algorithm	cluster	spectral distance	species	chromophore
Single-Linkage	1	0.451	DSM 158	spheroidene
	2		DSM 123, DSM 467	spirilloxanthin
	3	0.518	Nm 02	cytochrome c
	4		Nm-50, Nm-53	cytochrome c
Complete-Linkage	1	0.474	DSM 158	spheroidene
	2		DSM 123, DSM 467	spirilloxanthin
	3	0.631	Nm 02	cytochrome c
	4		Nm-50, Nm-53	cytochrome c
Average-Linkage	1	0.463	DSM 158	spheroidene
	2		DSM 123, DSM 467	spirilloxanthin
	3	0.575	Nm 02	cytochrome c
	4		Nm-50, Nm-53	cytochrome c
Weighted-Average-Linkage	1	0.463	DSM 158	spheroidene
	2		DSM 123, DSM 467	spirilloxanthin
	3	0.575	Nm 02	cytochrome c
	4		Nm-50, Nm-53	cytochrome c
Centroid	1	0.431	DSM 158	spheroidene
	2		DSM 123, DSM 467	spirilloxanthin
	3	0.471	Nm 02	cytochrome c
	4		Nm-50, Nm-53	cytochrome c
Median	1	0.431	DSM 158	spheroidene
	2		DSM 123, DSM 467	spirilloxanthin
	3	0.471	Nm 02	cytochrome c
	4		Nm-50, Nm-53	cytochrome c
Ward*	1	0.438	DSM 158	spheroidene
	2	[0.575]	DSM 123, DSM 467	spirilloxanthin
	3	0.458	Nm 02	cytochrome c
	4	[0.629]	Nm-50, Nm-53	cytochrome c

Table 4.2: * The spectral distance D given for the Ward algorithm was calculated from the Heterogeneity H (given in square brackets) based on Eq. 4.1 with $H(r,i) = n(r+i)D(r,i)^2$.

As can be seen, the resonant Raman spectra from different chromophores can be easily separated. Cluster (1) and (2) have a spectral distance of 0.45 $\pm$ 0.02 depending on the applied algorithm. The Ward algorithm calculated a spectral Heterogeneity of 0.58, which gives a spectral distance of 0.44. The chromophore of all spectra sorted into the clusters (3) and (4) is cytochrome c. The spectral distance found between these clusters is given as 0.50 $\pm$ 0.09 by all tested algorithms. The spectra in Figure 4.1 give an impression of how the spectral distances relate to visible differences in the spectra. Please note that the largest spectral distance between reference spectra of the same bacterial culture was found to be 0.11 or less by all tested algorithms.

The spectral distance found between the clusters holding purple non-sulfur bacteria (1 and 2) and the clusters holding *Nitrosomonae* (3 and 4) is given as 1.4 by all algorithms save Ward. The Heterogeneity calculated by the Ward algorithm was 22.3, corresponding to a spectral distance of 1.9.

It is noteworthy, that in comparison to the algorithms in eqs. 2.8-2.13, the Ward algorithm (eq. 2.14) computes larger spectral distances between clusters of spectra originating from the same (cytochrome c) or from distinctly different chromophores (cytochrome c vs. carotenoids), but the spectral distances computed between clusters of spectra originating from similar – but not identical – chromophores (spheroidene, spirilloxanthin) are smaller than those determined by the algorithms in eqs. 2.8-2.13.

4.1.3 Single spectra clustering

A total of 44 single spectra previously contributing to the reference spectra was chosen for the clustering: 8 spectra of *Rhodobacter sphaeroides*, 9 spectra of *Rhodopseudomonas palustris*, 10 spectra of *Rhodospirillum rubrum*, 4 spectra of *Nitromonas communis*, and 13 spectra of *Nitrosomonas europaea* (7 spectra of Nm-50 and 6 spectra of Nm-53). The size of the individual sample batches was varied to simulate realistic conditions when clustering data of unknown mixed samples. Figure 4.3 gives a vector normalized single spectrum of *Nitrosomonas communis* with an S/N of 11.5 in comparison to the corresponding reference spectrum to illustrate the differences in spectrum quality between single and reference spectra.

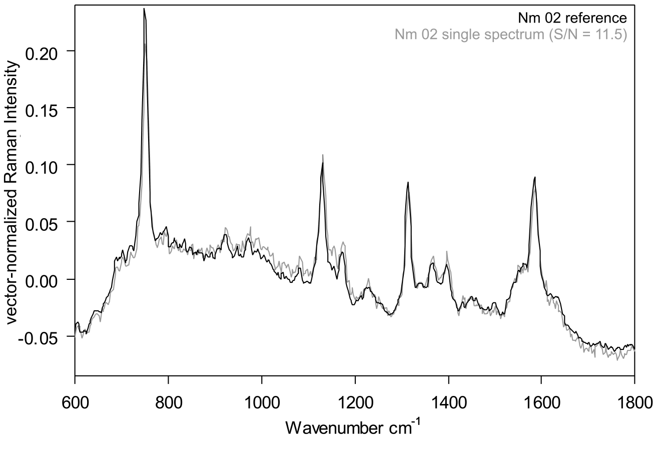

Figure 4.3: Reference spectrum (average of 100 single spectra of S/N $\geq$ 10) and single spectrum (S/N = 11.5) of *Nitrosomonas communis* Nm-02 in vector normalization. (Figure first published in Kniggendorf et al. [2011a].)

As can be seen from the data given in table 4.3, the clustering algorithms performed very differently when used on non-averaged resonance Raman spectra (single spectra) with an S/N between 10 and 20.

Distinctly different chromophores (carotenoids and cytochrome c) were separated by all of the seven tested algorithms also when applied to single spectra.

Single spectra clustering					
algorithm	cluster	spectral distance	deviation from ref. [%]	spectral relation maintained?	assignment errors
Single-Linkage	1	0.377	16	+	
	2				2
	3	0.222	57	-	
	4				
Complete-Linkage	1	0.666	41	+	
	2				6
	3	0.931	48	-	
	4				2
Average-Linkage	1	n.a.	n.a.	-	19
	3				2
	4	n.a.	n.a.	-	
	4’				
Weighted-Average-Linkage	1	0.493	7	+	
	2				1
	3	0.581	1	+	
	4				2
Centroid	1	0.363	25	+	
	2				7
	3	0.353	25	+	
	4				2
Median	1	0.334	23	+	
	2				6
	3	0.389	17	+	
	4				2
Ward*	1	0.389 [4.090]	13	+	
	2				2
	3	0.356 [2.152]	29	-	
	4				2

Table 4.3: * The spectral distance D given for the Ward algorithm was calculated from the Heterogeneity H (given in square brackets) based on Eq. 4.1 with $H(r,i) = n(r+i)D(r,i)^2$.

Slightly different chromophores (the carotenoids spheroidene and spirilloxanthin) were separated by all algorithms except Average-Linkage (2.10), which placed all carotenoid spectra in one group. The spectral relation between the three types of purple non-sulfur bacteria, i.e. *Rhodopseudomonas* and *Rhodospirillum* being grouped into one cluster separate from *Rhodobacter*, as established in the clustering of the reference spectra (see 4.1.2) was also maintained by all algorithms except Average-Linkage.

Reliability in the clustering of individual single spectra ranged from above 97% (Weighted-Average-Linkage (2.11)), over 95% (Single-Linkage (2.8) and Ward (2.14)) and 90% (Median (2.13) and Centroid (2.12)), down to 85% (Complete-Linkage (2.9)).

Spectra originating from the same chromophore (cytochrome c) were grouped with a reliability of 90% or better by all algorithms, excluding Average-Linkage. However, only two algorithms – Weighted-Average-Linkage (2.11) (the dendrogram is given in Figure 4.4) and Centroid (2.12) – maintained the spectral relation of *Nitrosomonas communis* Nm-02 being separated (cluster 3) from the two stands of *Nitrosomonas europaea* (Nm-50 and Nm-53 grouped in cluster 4) found when clustering the reference spectra.

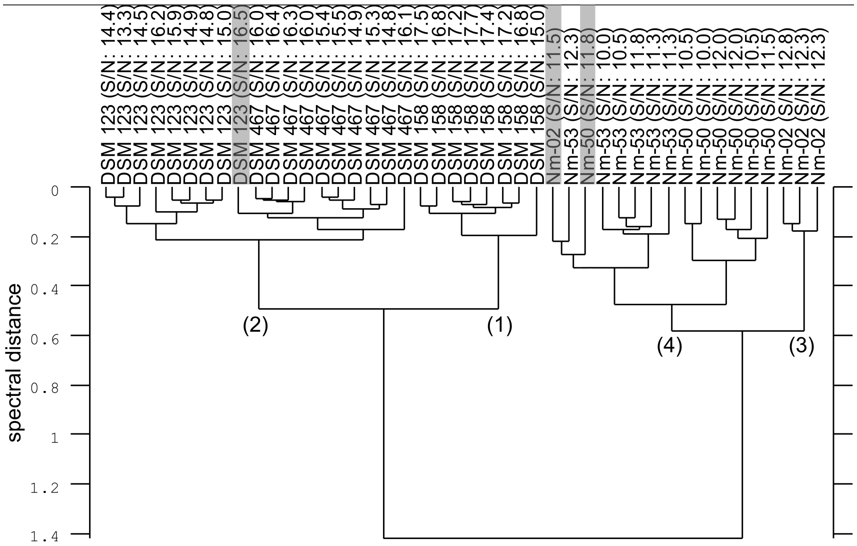

Figure 4.4: Resonance Raman spectra of single cells (S/N ≥ 10) clustered with the Weighted-Average-Linkage algorithm. Grayed spectra were assigned to the wrong cluster. For the exact distances found between clusters (1) and (2) – and (3) and (4), respectively – see Table 4.3.(Figure first published in Kniggendorf et al. [2011a].)

These differences in performance when clustering resonance Raman spectra of single cells can be understood from the perspective of the respective clustering procedures used by the algorithms. The best algorithm, Weighted-Average-Linkage (2.11), determines the spectral distance between clusters by forming the weighted average of their components. In terms of Raman spectra this amounts to calculating the average spectrum of the respective cluster. Thus the S/N-ratio of the spectra representing the clusters improves with each clustering step, resulting in almost perfect agreement (1% deviation from the reference clustering) in case of spectra originating from the same chromophore (cytochrome c in *Nitrosomonas*) and still a very good agreement (7% deviation) in case of slightly different chromophores (carotenoids in purple non-sulfur bacteria).

In contrast, the second algorithm maintaining the spectral relation between the bacteria, Centroid (2.12), shows better agreement only in later stages of the clustering when the clusters hold a larger number of spectra, resulting in the centroid being more representative of the weighted spectral average. Thus the spectral relation determined by the reference spectra is reproduced, but a comparatively high number of single spectra is assigned to wrong sub-clusters.

In comparison, the spectral distances calculated by algorithms failing to reproduce the spectral relation between the bacteria deviated from the results obtained by clustering reference spectra between 20% (Median algorithm (2.13) with eight erroneously assigned single spectra) and 45% (Complete-Linkage (2.9) also with eight erroneously assigned single spectra). Median, choosing the spectrum closest to the centroid of the cluster as representative of the cluster, shows an amount of erroneously assigned single spectra comparable to that of the Centroid algorithm.

Average-Linkage (2.10) was not considered in this part of the analysis, because its result showed no similarity to that of the reference clustering at all.

The widely used Ward algorithm (2.14) as well as Single-Linkage (2.8) reproduced the spectral distance between clusters of spectra from slightly different chromophores (carotenoids in purple non-sulfur bacteria) with only 13% (16% in case of Single-Linkage) deviation in the spectral distance between clusters (1) and (2) (and two erroneously assigned single spectra), but failed to maintain the spectral relation between the *Nitrosomonae* (common chromophore: cytochrome c) with a deviation of 29% (57% respectively) in the spectral distance found between clusters (3) and (4). Figure 4.5 shows the Heterogeneity dendrogram as calculated by the Ward algorithm. This similarity in results in unsurprising when considering that the Single-Linkage algorithm (2.8) determines the spectral distance between clusters as the minimum of the spectral distances between the components of said clusters, while the Ward algorithm (2.14) does essentially the same with a weighted square of the spectral distances, giving it a slight advantage when handling spectra of the same chromophore (cytochrome c in *Nitrosomonas*).

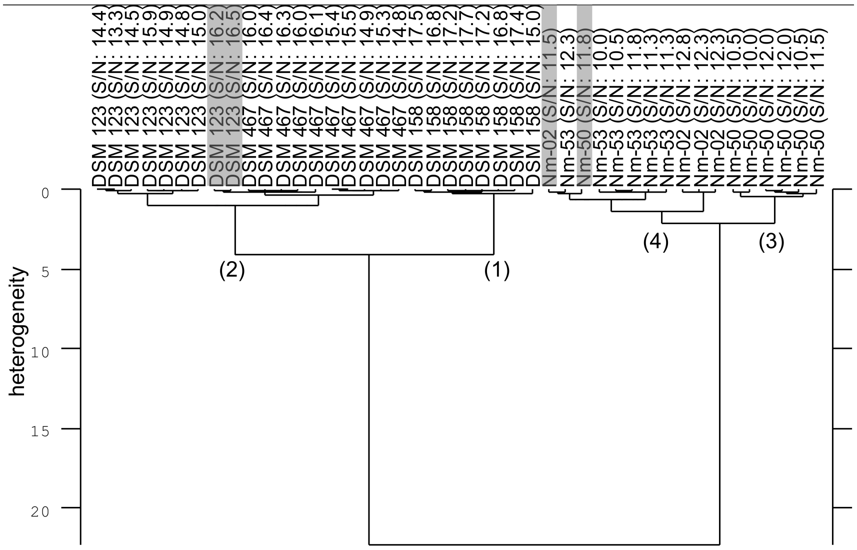

Figure 4.5: Single spectra of S/N $\geq$ 10 clustered using the Ward algorithm. Grayed spectra were assigned to the wrong cluster. Please note that the Ward algorithm computes the Heterogeneity H, which is proportional to the square of the spectral distance rather than the spectral distance itself. For the exact Heterogeneity found between clusters (1) and (2) – and (3) and (4), respectively – see table 4.3.(Figure first published in Kniggendorf et al. [2011a].)

To the best of my knowledge, there has not been a performance evaluation of HCA algorithms for (resonant) Raman spectra so far, but several studies have been conducted for other types of data, such as the concentrations of chemical compounds used as markers for eutrophic levels in coastal waters [Primpas et al., 2008], most of which show a clear advantage for the Ward algorithm. However, the data subjected to clustering in these studies are scalars, whereas Raman spectra are vectors. These vectors describe intensity over pixel, which is composed of signal intensity, unavoidable background intensity (determinate noise) and random noise. Weighted-Average-Linkage (and to a lesser degree Centroid) reduce random noise when calculating the representative spectra of clusters, whereas the procedures of the other algorithms do not affect the random noise component of the spectra.

4.2 Effects of spectrum quality on HCA

Large differences in the spectrum quality, quantified by the S/N-ratio (compare section 3.1.2), may have severe effects on the results of clustering Raman spectra obtained from single cells. While spectra of distinctly different chromophores (carotenoids vs. cytochrome c) are still separated properly, the differences in the S/N-ratios may well exceed signal variations caused by different host organisms in spectra originating from the same chromophore (cytochrome c or spirilloxanthin), as can be seen in Figure 4.6 with the grouping of DSM 123 and DSM 467, both of which carry spirilloxanthin as main chromophore. This agrees with the findings of Bonifacio et al. [2008], who observed that HCA (Ward algorithm) – for them unexpectedly – distinguished also between intense and weak resonant Raman spectra of intra-cellular heme molecules. In addition, spectra of comparatively low quality may result in early separation from the main bulk and the creation of additional clusters. An automated analysis of the dendrogram given in Figure 4.6 returns

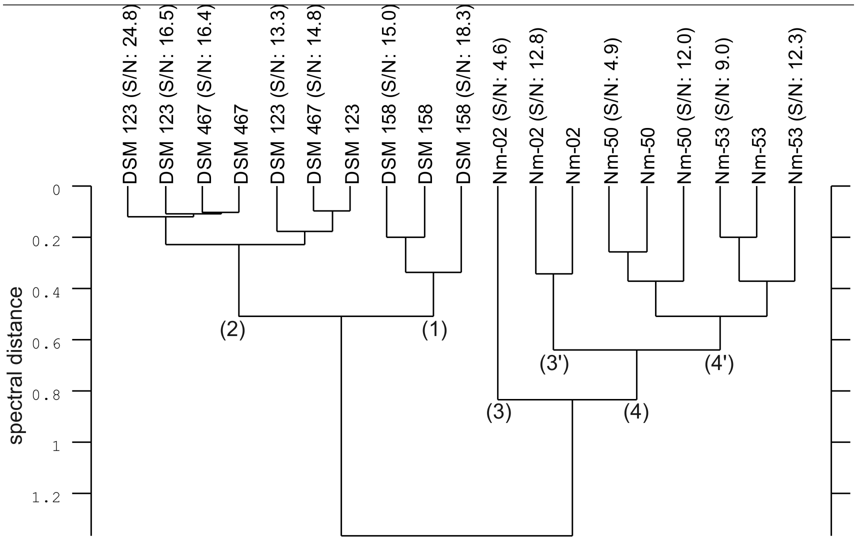

Figure 4.6: Effects of low signal-to-noise ratios in hierarchical cluster analysis of resonance Raman spectra. The dendrogram was calculated with the Weighted-Average-Linkage algorithm, which performed best among the tested algorithms. Single spectra are indicated by their S/N ratio given in brackets.(Figure first published in Kniggendorf et al. [2011a].)

the marked clusters (3) and (4), whereas the important species separation happens in the marked clusters (3') and (4'), both grouped together in (4). This also agrees with Bonifacio et al. [2008].

4.2.1 Test for spectrum quality influences

The results of a HCA can be severely influenced by spectrum quality as shown in 4.2. In order to avoid results biased by variation in spectrum quality, it is imperative to **subject only spectra within a certain range of spectrum quality to the HCA**, thus excluding spectra of the lowest quality as well as spectra well above average quality. This corresponds with the requirement of excluding extremes from the data intended for clustering [Sharma, 2006].

However, the width of the range of spectrum quality acceptable for a HCA depends on the average spectrum quality of the data set and – most notably – the variance of the spectra to be clustered. If the spectra are distinctly different, only extreme quality variations will outweigh that as a clustering criterion. However, if the spectra differ only ever so slightly, the quality of the spectra may well become critical fast and the results of a hierarchical cluster analysis will have to be analyzed attentively for influences of spectrum quality.

Therefore, only the results of a HCA performed on Raman spectra with known spectrum quality can be trusted. In order to **check the results of a HCA for influences of spectrum quality**, it should be repeated on a subset of the Raman spectra with the least variation in spectrum quality possible. If the spectral distances and spectral relations found in clustering this subset of Raman spectra alone differ from when it is part of the full data set, it is very likely that spectrum quality may at least partially affect the results. In this case, the full data set may be divided into subsets according to range of spectrum quality. These subsets need not be mutually exclusive.

For example, if a set of Raman spectra intended for HCA has S/N between 10 and 14, but the above mentioned test confirms that only Raman spectra with a difference of 2 in spectrum quality are clustered for their spectrum variations rather than their quality differences. The whole set can be divided into subsets with S/N $\in$ [10, 12], [12, 14], or [11, 13]. The results of the HCAs performed on the subsets can then be compiled into a result for the whole set, even if a dendrogram of the whole set is not possible in this case (see 2.3.1).

If the results between the validated subsets differ, the results of subsets with higher spectrum quality are more reliable, because the Raman information contained in the spectra of lower quality may be insufficient in comparison to spectra of better quality.

The afore described test has been performed on all HCA results and dendrograms presented in this work, including the dendrogram given in Fig. 4.6 intended to illustrate the effects an omission of this test may cause.

4.3 Native variability and spectral similarity

In order to gauge the natural variability seen in the resonant Raman spectra of bacteria expressing cytochrome-c, Raman spectra recorded from individual cells of *Nitrosomonas communis* Nm-02, two strains of *Nitrosomonas europaea* (Nm-50, Nm-53), and *Rhodobacter sphaeroides* DSM 158^T expressing cytochrome-cbb$_3$ and spheroidene as well as its carotenoids-free mutant DSM 2340^T were spectrally compared with their references (see 3.2.1) by OPUS IDENT (see 2.3.3). All spectra had an S/N between 10 and 13. In case of DSM 2340^T, the „single spectrum“ was mimicked by averaging 25 spectra of individual cells to eliminate effects of severely variant S/N within the study (see 4.2).

Spectral similarity [%]

	Reference spectrum				
single spectrum	DSM 158	DSM 2340	Nm-02	Nm-50	Nm-53
DSM 2340	🟪 48.61	🟦 96.55	🟧 -	🟧 56.31	🟧 59.65
Nm-02 006 004	🟥 0.00	🟧 20.85	🟦 94.13	🟨 58.04	🟨 73.62
Nm-02 008 000	🟥 0.00	🟧 21.64	🟦 94.82	🟨 60.98	🟨 75.51
Nm-02 013 001	🟥 0.00	🟧 30.21	🟦 97.30	🟨 69.43	🟨 82.51
Nm-50 016 022	🟥 10.45	🟧 50.23	🟨 91.91	🟦 92.84	🟩 92.10
Nm-50 029 031	🟥 16.50	🟧 56.06	🟨 87.81	🟦 94.95	🟩 93.98
Nm-50 032 014	🟥 14.80	🟧 53.90	🟨 85.93	🟦 95.40	🟩 89.82
Nm-50 044 023	🟥 10.55	🟧 51.01	🟨 92.52	🟦 92.33	🟩 92.87
Nm-53 011 030	🟥 17.85	🟧 63.41	🟨 84.96	🟩 78.81	🟦 95.72
Nm-53 011 041	🟥 16.28	🟧 63.84	🟨 87.67	🟩 81.54	🟦 96.03
Nm-53 012 029	🟥 12.89	🟧 60.63	🟨 90.32	🟩 80.18	🟦 94.73
Nm-53 020 045	🟥 19.89	🟧 66.55	🟨 87.19	🟩 86.35	🟦 96.95
Nm-53 025 017	🟥 17.80	🟧 67.18	🟨 87.20	🟩 83.20	🟦 96.38

Color key

identification inconclusive (multiple reference matches)

🟦 same chromophore, same genus, same species, same strain

🟩 same chromophore, same genus, same species, different strain

🟨 same chromophore, same genus, different species

🟧 slightly variant chromophore, different genus

🟥 different chromophore, different genus

🟪 different chromophore, same genus, same species, different strain

Table 4.4: Spectrum comparison of Raman spectra recorded from single cells to reference spectra

Table 4.4 gives the results of spectrum comparisons between resonant Raman spectra recorded from single cells and the respective reference spectra with respect to expressed chromophore and taxonomic relation of the bacteria.

Resonant Raman spectra recorded from individual cells of a pure culture are identified with 96 ± 4 % certainty when compared to spectra of the same strain and with 84 ± 5 % certainty when compared to spectra of a different strain of the same species, given that the two strains express the same chromophore. The spectral similarity of bacteria expressing cyt-cbb$_3$ instead of cyt-c (*Rhodobacter sphaeroides* DSM 2340^T compared to the *Nitrosomonae*) was typically 60 % or less. These numbers do not include results not clearly matched to a single reference (i.e. the spectral similarity to one or more other references was within a 5 % range from the best match).

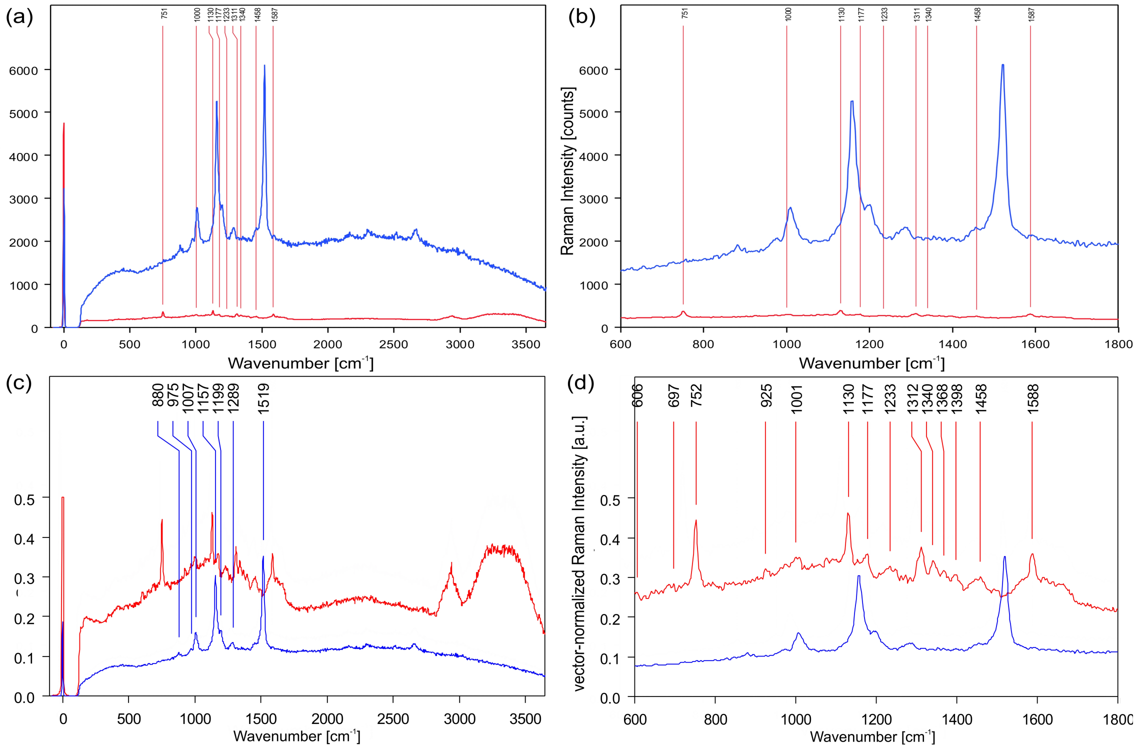

Figure 4.7: Resonant Raman spectrum of *Rhodobacter sphaeroides* DSM 158^T (blue) and its carotenoids-free mutant DSM 2340^T (red): full spectra as recorded (a), fingerprint as recorded (b), vector-normalized full spectra (c) and vector-normalized fingerprint (d).

The spectral distance from *Rhodobacter sphaeroides* DSM 158^T to its carotenoids-free mutant DSM 2340^T seems comparable to the spectral distances seen between bacteria expressing slightly different chromophores. However, one has to keep in mind that the definition of random noise used for quantifying the spectrum quality (see 3.1.2) does not cover noise components due to in-spectrum fluorescence. This does not affect „cytochromes-only comparisons“, but may well be important in this special case. The characteristic fluorescent background seen in cytochromes at Q-Band excitation [Friedman and Rousseau, 1978] may well provide the additional similarity between DSM 158 and DSM 2340, despite the presence of the Raman intense but fluorescence-free carotenoid in DSM 158 (Fig. 4.7).

The uncertainties decrease significantly with stricter limitation of the spectrum quality (i.e. allowing only a narrower band of S/N into the analysis). However, a stricter limitation of spectrum quality may also dramatically reduce the number of recorded spectra usable for an analysis.

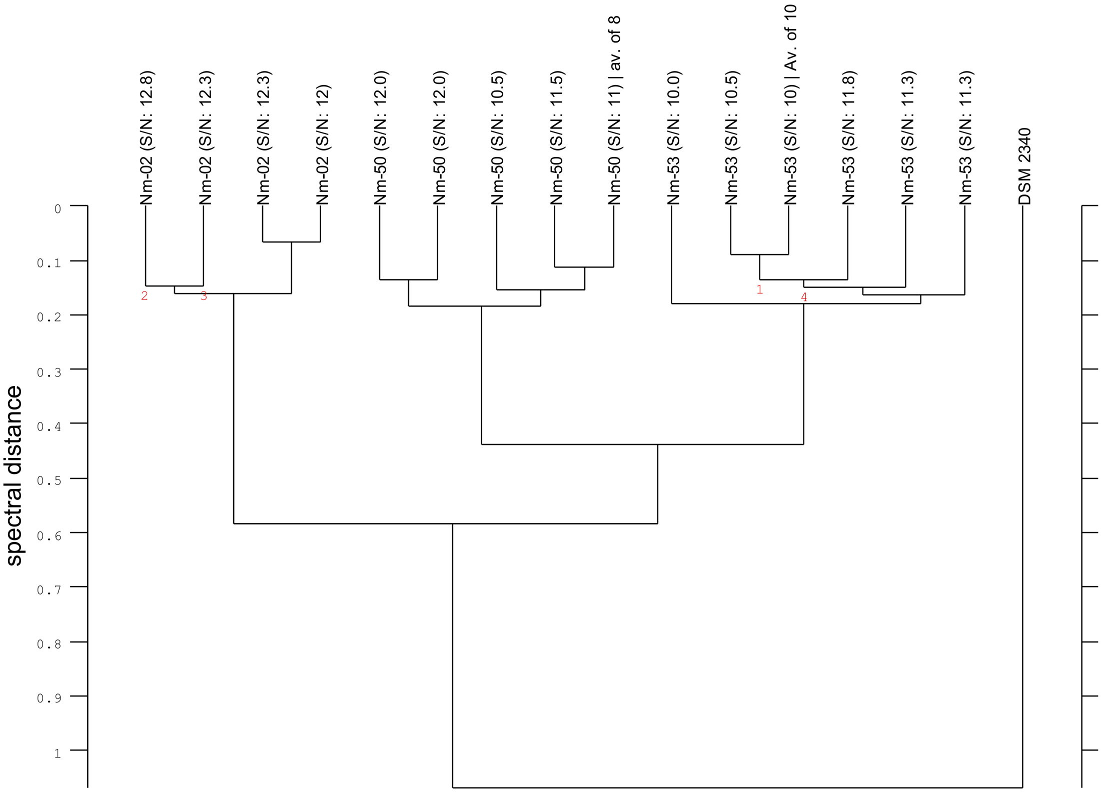

Figure 4.8: HCA of resonant Raman spectra recorded from individual cells of *Nitrosomonas communis* (Nm-02) and *Nitrosomonas europaea* (Nm-50, Nm-53), all of which expressing cyt-c, and the carotenoids-free mutant of *Rhodobacter sphaeroides* DSM 2340^T, expressing cyt-cbb$_3$. Algorithm: Weighted-Average-Linkage. Spectra cut and vector-normalized to 600 – 1800 cm^{-1}.

Fig. 4.8 shows a hierarchical cluster analysis of resonant Raman spectra recorded from individual cells of *Nitrosomonas communis* (Nm-02), two strains of *Nitrosomonas europaea* (Nm-50, Nm-53) and the carotenoids-free mutant of *Rhodobacter sphaeroides* (DSM 2340^T). The dominant chromophore of *Nitrosomonas* is cyt-c, whereas *Rhodobacter* expresses cyt-cbb$_3$ (see 3.2.4). The spectral distances determined in the HCA are given in Tab.4.3.

Spectral distances of up to 0.19 were found between spectra belonging to the same strain, a spectral distance of 0.44 between strains of the same species (*Nitrosomonas europaea*), and a spectral distance of 0.58 between different species holding the same chromophore (*Nitrosomonas communis* and *Nitrosomonas europaea*). The spectral distance to bacteria expressing a chromophore slightly variant from cyt-c – cyt-cbb$_3$ in case of *Rhodobacter sphaeroides* DSM 2340^T – is larger than 1 (1.61) to those of bacteria expressing cyt-c.

This fits well with the results of the spectrum comparison, which typically returns a similarity about 5 % above that determined by HCA: with 95 % or more similarity between spectra recorded from the same strain, 84 % similarity for spectra recorded from the same species but different strains, and 78 % similarity between different species. The unusual high similarity between DSM 2340 and the *Nitrosomonae* (45.77 %) is caused

spectral distances dendrified in Fig. 4.8

Raman spectra	maximum spectral distance	max. spectral distance [%]	corresponding similarity[◊] [%]
same strain:			
Nm-02	0.161	91.95	95.42
Nm-50	0.185	90.75	95.40
Nm-53	0.163	91.85	96.27
DSM 2340			96.55
same species:			
Nm-50, Nm-53	0.439	78.05	83.94
different species:			
Nm-02, (Nm-50, Nm-53)	0.584	70.80	77.55
variant chromophores:			
DSM 2340, Nm	1.608	19.60	45.77[†] 24.33[‡]

◊ averages from Tab. 4.4.

† DSM 2340 expressing cyt-cbb$_3$; similarity based on low quality reference (S/N=11).

‡ result when comparing DSM 2340 (S/N = 11) to spectra with an S/N $\geq$ 20.

by the low quality of the DSM 2340 reference spectrum (S/N = 11), which has a noise level comparable to that of most other single spectra; the figure drops to 24.33 % when only the spectra with an S/N of at least 20 are compared to it.

This is expected, given that HCA works solely with single spectra and thus is subject to their natural lower spectrum quality including all the variability seen in the resonance Raman spectra recorded from different living cells, whereas spectrum comparison compares the single spectra to reference spectra in which the natural variability has been reduced (see 3.2.1). However, not only does spectrum comparison require reference spectra, it is also highly sensitive to variations seen in individual spectra esp. when it comes not to an identification (spectra from the same strain), but to true comparison (spectra from different strains or even different species). In this case, HCA with the Weighted-Average Linkage algorithm returns more stable results, since the clustering procedure reduces the impact of the variations in individual spectra with each step (see 4.1.3).

4.4 Manual for Spectrum Comparison and HCA

Resonance Raman spectra of bacteria allow the identification of bacterial cells at strain level (95 % similarity to references (see 3.2.1) of the same strain, 84 % to different strains) and species level (78 % similarity) in case the main chromophores are strain-specific and do not change drastically due to mutation (see 4.3). Spectrum Comparison (see 2.3.3) and HCA (2.3.4) are valuable tools for identifying bacteria and determining their taxonomic relation. However, both techniques require precise preparations to return reliable results. These are summarized below.

Procedure	Comments
Data Preparation	
1. determine the S/N of the spectrum for the fingerprint region[†] as described in 3.1.2 2. cut the spectrum to the fingerprint region 3. vector-normalize the spectrum to the fingerprint region	† 600 – 1800 cm^{-1} throughout this work.
Spectrum Comparison	
1. select a set of references (see 3.2.1) covering expected matches as well as expected mismatches. Spectrum comparison between ordinary Raman spectra[†] is also possible, but highly sensitive to spectrum quality as a parameter (compare Tab. 4.3 with respect to DSM 2340). 2. spectral similarity of 95 % or more is considered a match (positive identification). If the spectral similarity to one or more of the references is within a 5 % ranger from the best match for the spectrum among the references, the spectrum is excluded as „not clearly identified“. 3. Interpretation of spectral similarity depends on the chromophore and its significance within the sample[‡].	† this is actually identical to the first clustering step in HCA, forming pairs of spectra (see 2.3.4). ‡ see 4.3 for an example of bacteria expressing cytochromes.
Hierarchical Cluster Analysis	
1. best performing algorithm for HCA of (resonance) Raman spectra: Weighted-Average-Linkage[†] (see 4.1.3). 2. determine the range of spectrum quality acceptable within a single analysis without spectrum quality variations exceeding chromophore variations as clustering criterion as described in 4.2.1 and divide the data into subsets if necessary	† HCA with Weighted-Average-Linkage returns more stable, i.e. reliable, results than a spectrum comparison when it comes to not identical spectra (similarity < 95 %); compare 4.3.

5 Mapping the biofilm: spatially resolved information

Microbial biofilms exist in very different forms and sizes, ranging from scarcely connected individual cells on a surface [O'Toole and Koller, 2002] to self-supporting microbial stromatolites large enough to have left fossil records as long as 3.46 billion years ago [Riding, 1999, Virginia Museum of Natural History, 2008].
Even biofilms consisting of a single species contain different micro-habitats, caused by concentration gradients of nutrients and products of the bacterial metabolism. These micro-habitats lead to adaptation of the bacterial cells within the respective micro-habitats, causing distinctive phenotypes of bacteria even within a mono-species biofilm [Steward and Franklin, 2008]. The situation in the much more common multi-species biofilms – for example in biological wastewater treatment – is naturally a lot more complex. Therefore, spatially resolved information about the bacteria associated in a biofilm is essential.
However, the sheer number of spectra contained in a spectral image recorded at the limit of spatial resolution (see 2.1.2) does not allow direct employment of the analytical procedures developed for individual Raman spectra in the previous chapters 3 and 4. Therefore, information about the distribution of Raman spectra and the fluorescent background had to be gained directly from the spectral images prior to subsequent analyses of representative spectra which had to be determined by analyzing the spectral images. In addition, the presentation of the spectral images was optimized to give a vivid and informative image of the analyzed biofilms (5.1).
Finally, the combination of the developed techniques was successfully used for analyzing the outer layer of biofilm granules, sampled from two sequencing batch reactors (SBR: see 2.5.1) for wastewater treatment, including morphological structure, associated bacteria, swaths of EPS, and embedded mineral particles (5.2)

Parts of this chapter were previously published in Kniggendorf et al. [2011a] and Kniggendorf and Meinhardt-Wollweber [accepted for publication w.m.r.].

5.1 Spectral Imaging: Biofilm Filters

Two different sets of filters were created to generate informative images from the recorded spectral images and to extract critical information – i.e. representative spectra – from the

data. The creation of broadband filters (see 5.1.1) can be directly done with the predefined Sum filter routine (see 2.2.3) included in WITec Project (see 2.2.1) for marking intensity over a specific spectral region.
Determining the distribution of a specific Raman spectrum was less straightforward, since the analysis routines of WITec Project are geared towards individual lines as indicators for Raman spectra, which works well as long as the individual spectra are suitably different in their lines. Unfortunately, this is not the case for resonance Raman spectra originating from the same main chromophore (see for example Tab. 3.1).
However, the distribution of a full Raman spectrum (or a predefined part of it, such as the fingerprint region) can be determined utilizing the Basis Analysis routine of WITec Project (see 2.2.4). By supplying only one spectrum $\vec{B}$ to the routine ($N = 1$), the returned image of the calculated weighting factor gives the distribution of that spectrum in the spectral image, given a carefully adjusted contrast between the Raman spectrum not exceeding the defined S/N threshold (black) and the most intense spectrum included in that spectral image (white; or the representative color of choice).
This routine was used for the creation of „fingerprint filters“ developed from Raman spectra frequently found in spectral images of biofilm samples (see 5.1.2).

5.1.1 Broadband image filters

Broadband image filters are independent of whether or not Raman active chromophores are present. They display a sectioned superposition of the always present background and possible Raman spectra, allowing to mark areas of pure fluorescence and/or high water content. For this, the recorded spectrum range was divided into three disjoint regions with region I going from 200 to 1300 cm^{-1} (colored red), region II from 1300 to 2400 cm^{-1} (yellow), and region III from 2400 to 3500 cm^{-1} (blue). The regions below 200 and above 3500 cm^{-1} were discarded. Fig. 5.1(a) gives the spectral sectioning for broadband filters superimposed on an exemplary set of (resonant) Raman spectra. Maximum and minimum intensity were defined per filtered image as the brightest and darkest pixel, with the darkest pixel being set to „black“ (maximum contrast), resulting in a superimposition of the three filtered images („**broadband image**“) giving white in case of plain fluorescence (same intensity in all three regions), blue in case of high water content due to the wide Raman band consisting of unresolved OH-stretching modes above 3000 cm^{-1}, and monochrome, unstructured red in case of glasses with homogenous density (for example microscope slides or cover slips).

Microbial content shows as structured red and purple in a broadband image, due to the main intensity of bacterial spectra being primarily in broadband region I (red) and less in II (yellow). The structures are due to the variant density typically seen in microbial biofilm. The water content of low density biofilm matter gives a low intensity in III (blue), resulting in dark blue coloring (or purple in case of bacteria being present).

Mineral microparticles, having Raman spectra with comparatively low intensity and no fluorescent background do not show in broadband images, except as dark areas with

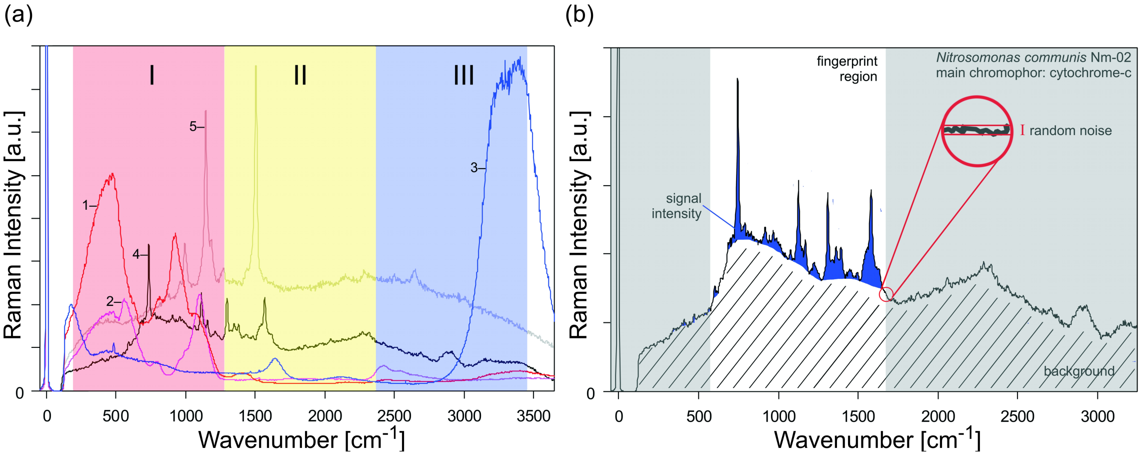

Figure 5.1: Broadband image filters (a), dividing the full spectrum into three equal regions, are independent of a chromophore being detected. Included (resonant) Raman spectra are glass of an uncoated microscope slide (1) and a cover slip (2), water (3), Nitrosomonas communis Nm-02 (chromophore: cyt-c) (4), and Rhodobacter sphaeroides DSM 158^T (chromophore: spheroidene) (5). Fingerprint image filters (b) return the distribution and intensity of a specific (resonance) Raman spectrum within the recorded spectral image. For their construction the shaded parts of the spectrum are cut and the fluorescent background (hatched) is substracted. (Figure first published in Kniggendorf and Meinhardt-Wollweber [accepted for publication w.m.r.].)

little to no intensity.

5.1.2 Fingerprint image filters

Fingerprint image filters give the distribution of a specific Raman spectrum within the recorded spectral image. Fingerprint image filters were constructed from the fingerprint region of Raman spectra found recurrently in the spectral images (including various types of unidentified bacteria and microparticles).

Raman spectra of mineral microparticles were identified via RRUFF™ [Downs, 2006] and used in their entirety due to their negligible background and low number of Raman lines.

Fingerprint image filters for more complex Raman spectra with noticeable intrinsic fluorescent background – as for example seen in spectra of bacteria expressing cytochrome-c as main chromophore – were prepared as follows: The spectra were cut to the fingerprint region (600 – 1800 cm^{-1} throughout this work), followed by a full background reduction (9th order polynomial fit) over the same region (see Fig. 5.1). Intensity of a specific Raman line had to exceed the random noise (see 3.1 and inset in Fig. 5.1(b)) by at least a factor of two to be considered as signal.

Maximum intensity was set for the pixel holding the strongest Raman spectrum with respect to the four most intense Raman lines within the fingerprint region (in accordance with the definition used to quantify spectrum quality (see 3.1.2). Minimum intensity

(„black“) was set for the four strongest Raman lines of the respective filter not exceeding background intensity.

Fingerprint images were constructed by superimposing the fingerprint filtered images of interest in WITec Project (see 2.2.1). In addition, the respective images were exported as monochromes from WITec Project and superimposed with a conventional graphics software (Corel Photopaint™ X3 by Corel, Ottawa, Canada) to validate results obtained with WITec Project. Colors were chosen with respect to visibility. The number of fingerprint filters usable on a recorded spectral image is virtually unlimited, but the number of fingerprint filtered images that can be included in a single superimposition („**fingerprint image**“) is limited by the number of available colors and the limitations of additive color blending. However, an unlimited number of different fingerprint images can be created for a recorded spectral image.

5.2 The acid test: analyzing microbial aggregates

Resonance Raman micro-spectroscopy on cytochrome-c (532 nm excitation) is widely incompatible with the standard techniques for biofilm analysis relying on fluorescent dyes. Therefore, a source of fully characterized and macroscopically monitored biofilm samples was analyzed to demonstrate the effectiveness of the techniques developed in 5.1 and in the previous chapters 3 and 4.
For this, the outer layer of microbial biofilm granules sampled from two sequencing batch reactors (SBR; see 2.5.1) operated at the Institute of Biophysics, were analyzed with confocal resonance Raman micro-spectroscopy. SBR-1 showed nominal anammox operation, whereas no deammonification occured in SBR-0. However, an increasing infestation with not otherwise specified purple bacteria made SBR-0 an interesting source for samples with unknown properties.

Figure 5.2 shows a typical image set for SBR-0 (top) infested with purple bacteria, and SBR-1 (bottom) with anammox activity. Both measurements were made after one month of operation. These two examplary measurements will be used in this chapter to show and discuss the (potential) information contained in confocal resonance Raman micro-spectroscopy images of biofilms.
The image set includes: the spectral image (see 2.1.2) as recorded (full spectral intensity) on the left, broadband images (see 5.1.1) in the center, and fingerprint images (see 5.1.2) on the right. The corresponding Raman spectra for the fingerprint images in Fig. 5.2(c) and (f) are given in Fig. 5.3.

5.2.1 Chromophore identification

The main chromophores found in Raman spectra from the outer layer of granules sampled from SBR-0 were identified as carotenoids with a spheroidene backbone (most intense Raman line at 1519 cm^{-1}; bacterial spectrum given in Fig. 5.3(a), spectrum (a1),

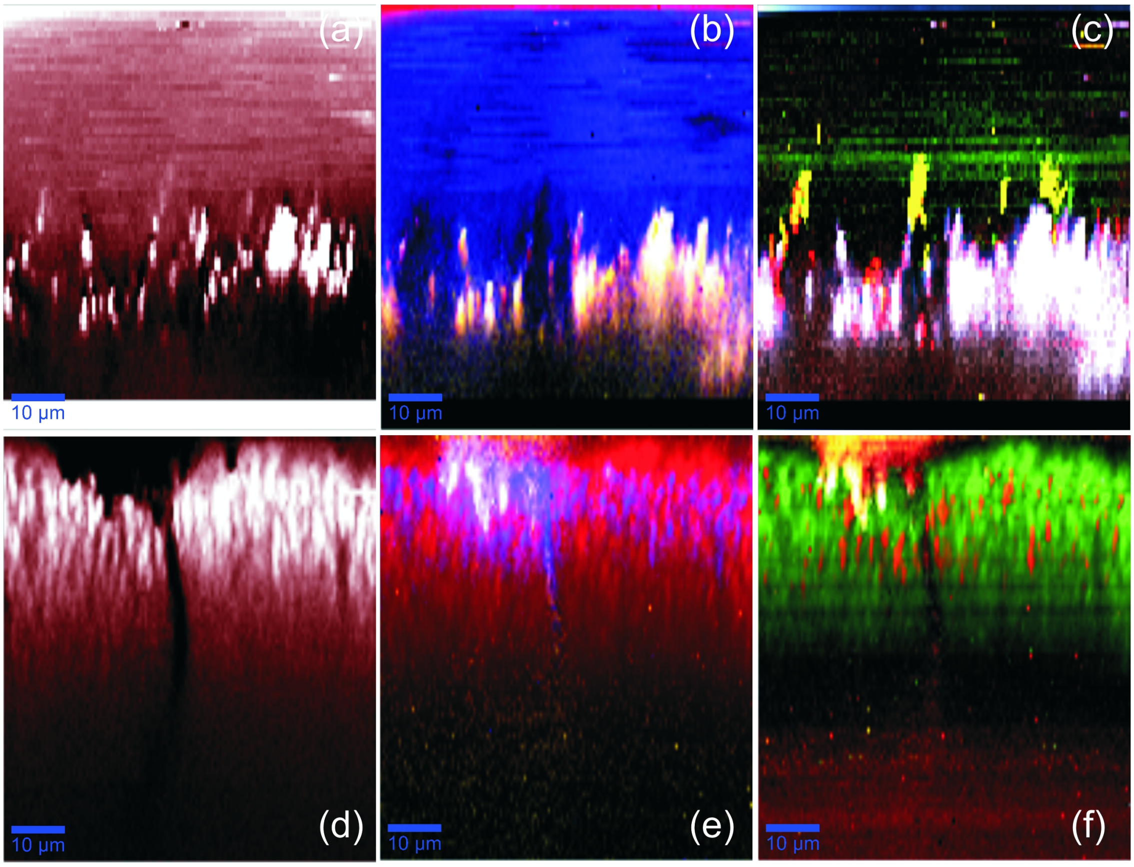

Figure 5.2: Top row – outer layer of a granule sampled from SBR-0 (infected with purple bacteria): full spectrum as recorded (a), broadband image (b) showing wide, water-filled gaps and a cover of low density biomass (dark blue) and intense fluorescence (white) within the single layer of elongated microcolonies, and fingerprint image (c) revealing anatase microparticles (yellow) and purple bacteria holding spheroidene (magenta), growing at and around rutile microparticles (red), covered by neurosporene expressing bacteria (blue) on water exposed surfaces. Bottom row – outer layer of a granule sampled from SBR-1 (anammox operation): full spectral intensity as recorded (d) showing a dense multilayer of microcolonies crossed centrally by a vertical canal (a second canal is touched near the right border of the image), the broadband filtering (e) revealed water (blue) within the canal and the top third of the multilayer as well as weak fluorescence (white) to the left of its bulk water opening, fingerprint filtering (f) showed two types of *Nitrosomonas* microcolonies: *N. communis* (green) and a second species (red). Corresponding (resonance) Raman spectra to (c) and (f) are given in Fig. 5.3 (Figure first published in Kniggendorf and Meinhardt-Wollweber [accepted for publication w.m.r.].)

blue).

Whereas the main chromophore found in the Raman spectra recorded in the outer layer of granules sampled from SBR-1 was cytochrome-c (compare 3.2.3), thus allowing for bacterial tracking (described below in 5.2.3) and identification (5.2.4).

These substances were identified by their Raman spectra as reported by Koyama [1995] and Hu et al. [1993] (cytochrome-c). Spheroidene was additionally confirmed by measureing a culture of *Rhodobacter sphaeroides* DSM 158^T, expressing spheroidene as confirmed by absorption spectroscopy (see 3.2.2). Cytochrome-c was additionally confirmed by comparison to a measurement of the pure substance (see 3.2.3).

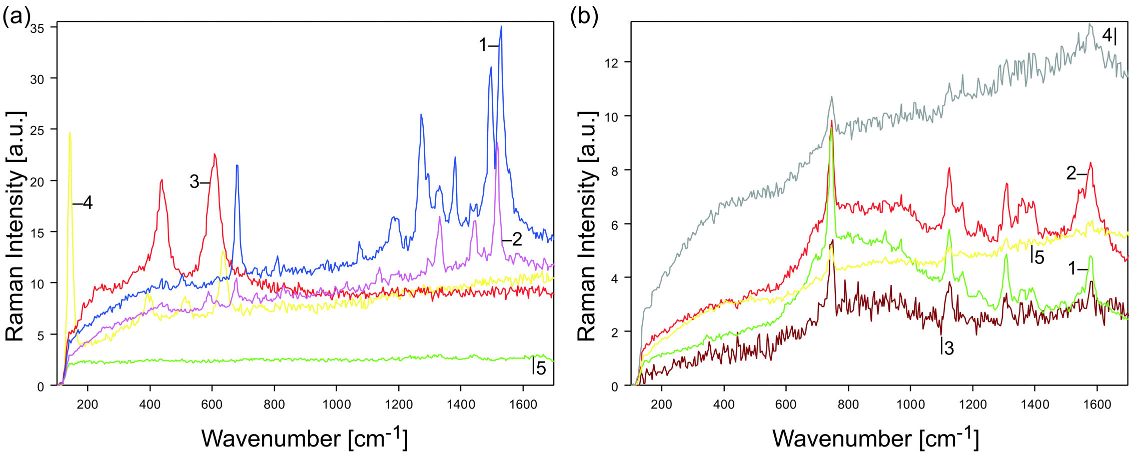

Figure 5.3: (a1) Purple bacteria expressing neurosporene (Fig. 5.2(c) blue), (a2) purple bacteria expressing spheroidene (Fig. 5.2(c) magenta), (a3) rutile (Fig. 5.2(c) red), (a4) anatase (Fig. 5.2(c) yellow), (a5) a bacterial cell containing no chromophores (Fig. 5.2(c) green), (b1) seed fingerprint type I identified as *Nitrosomonas communis* (Fig. 5.2(f) green), (b2) seed fingerprint type II (Fig. 5.2(f) red), (b3) cyt-c spectrum 80 μm below the surface (Fig. 5.2(f) brown), and (b4) fluorescence (Fig. 5.2(f) yellow-white).(Figure first published in Kniggendorf and Meinhardt-Wollweber [accepted for publication w.m.r.].)

In addition, the Raman spectra of two phases of mineral TiO_2 were found recurrently: Rutile (Fig. 5.3(a), spectrum (a3), red) forming acicular or prismatic crystals, is the most common form of TiO_2 used as a white pigment even in foods, and anatase (Fig. 5.3(a), spectrum (a4), yellow) in its typical dipyramidal or planar crystals.
Raman spectra occurring only isolated and in low numbers in the three months of measurements were considered natural impurities and ignored in further analysis.

5.2.2 Spatially resolved information: structure and content

Structure of the outer layer

As can be seen already in the full intensity images (left side of Fig. 5.2), the outer layers of the granules sampled from different SBRs are distinctly different from each other, with the outer layer of the granules from SBR-0 (Fig. 5.2(a)) being less regularly structured and of smaller overall width than that found in anammox granules sampled from SBR-1 (Fig. 5.2(d)).
In SBR-0 granules, microcolonies form a haphazard monolayer with wide, irregular gaps, while the microcolonies seen in SBR-1 granules are ordered in a dense multilayer with well-defined borders and few distinct channels into the depth of the granule. The width of these channels in SBR-1 granules seldom exceeded 3 μm.
3D images, recorded as described in 2.1.2, revealed the distance between adjacent bacterial microcolonies to seldom exceed 0.5 μm (below the average cell size of Nitrosomonae (0.8 – 1.2 μm [Fang et al., 2010]) in granules sampled from SBR-1 (see Fig.

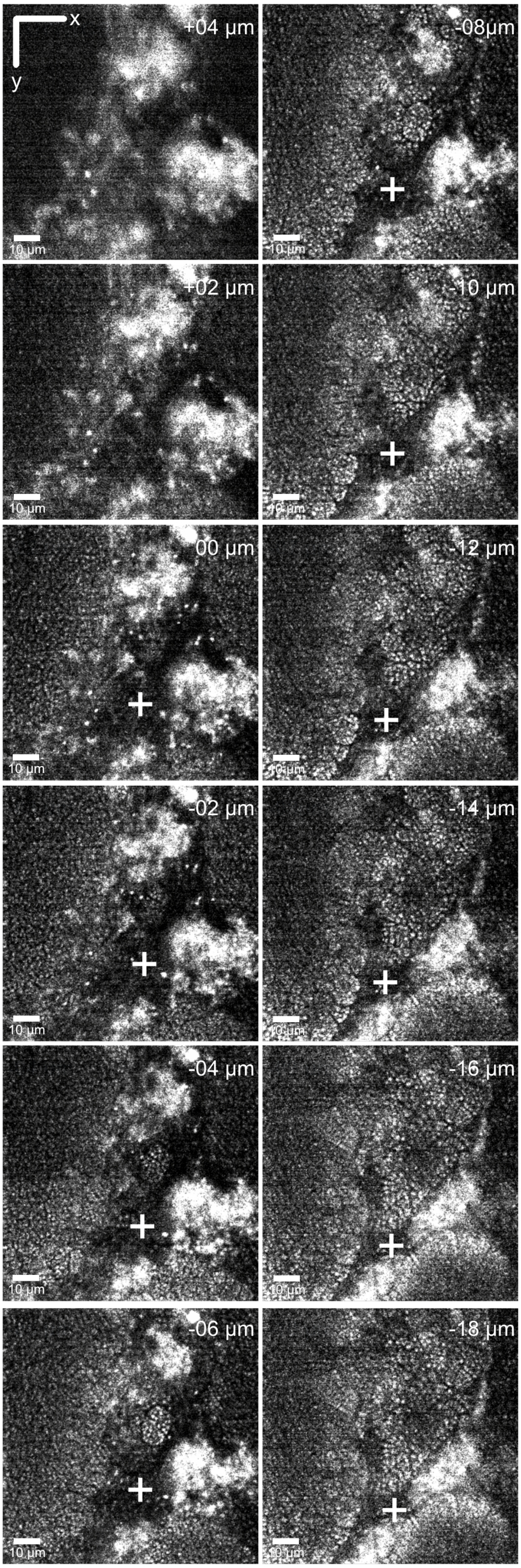
x
y
+04 µm
+02 µm
00 µm
-02 µm
-04 µm
-06 µm
-08µm
-10 µm
-12 µm
-14 µm
-16 µm
-18 µm
10 µm
+

Figure 5.4: Excerpt of an image stack covering 100 x 100 x 20 μm of the outer layer of an anammox granule showing a canal (+). Every second image is shown; images below -20 μm were ignored; altitude was set to 0 for the first focused layer of cells; analyzed wavenumber: 749 cm^{-1} (strongest resonance Raman line of cyt-c); excitation time per pixel: 0.1 s. (Figure first published in Kniggendorf and Meinhardt-Wollweber [accepted for publication w.m.r.].)

5.4), whereas microcolonies in granules from SBR-0 were distanced 1 μm and more from one another (Fig. 5.2(a-c)).

Discriminating fluorescence, water, and biomass

The broadband image of the granule sampled from SBR-0 (Fig. 5.2(b)) revealed strong fluorescence (white) at the core of the microcolonies and large gaps of approx. 8 – 10 μm width in the outer layer, filled with water (blue) and water-saturated, low density biomass (dark blue).

Fig. 5.2(e) shows the broadband image recorded from the nitrification layer of the granule sampled from SBR-1. Only a comparatively small area on the surface shows slight fluorescence (white). The low intensity of the fluorescent area can be seen by comparison with the image of full intensity as recorded (Fig. 5.2(d)). The channels of approx. 3 μm width are filled with water (blue). The outer layer traversed by these channels is formed of microbial colonies (red; purple colonies have a noticeable water content, confirmed via the respective Raman spectra).

Microbial communities – who's where?

The elongated microcolonies seen already in the full intensity images of both SBRs (see 5.2.2) are distinctly different from each other in their resonant Raman signatures.

SBR-0: As seen in Fig. 5.2(c), individual bacterial colonies typically had a width of approx. 2 – 3 μm in the xy-plane and a length of approx. 6 – 15 μm in the z-direction. Only one layer of colonies was typically observed, spanning the whole width of the outer layer. The strong fluorescent background made it impossible to detect Raman signals in the core of these microcolonies. However, on the surfaces of all microcolonies were purple bacteria expressing primarily spheroidene (magenta, spectrum (a2) in Fig. 5.3(a)) and often an additional thin layer of bacteria expressing neurosporene (blue, spectrum (a1) in Fig. 5.3(a)) above them on the surfaces exposed directly to bulk water. The latter were also seen on the walls of the wide, water filled gaps.

Carotenoids like spheroidene and neurosporene are ubiquitous chromophores, which in phototrophic bacteria are mostly associated with the light harvesting complexes [Cogdell et al., 2006]. Since both carotenoids are part of the spheroidene pathway for biosynthesis of carotenoids in phototrophic purple bacteria [Takaichi, 2008a], a decision of whether or not the two different carotenoids are indicative of two different species of purple bacteria [Okubo et al., 2006], or are in fact indicative of an adaptation of the same species to different habitat conditions in the biofilm [Steward and Franklin, 2008], e.g. stopping the carotenoid synthesis at neurosporene when in contact to bulk water, instead of continuing down the synthesis pathway towards spheroidene, is not yet possible.

However, Pudney et al. [2011] successfully traced the molecular status of multiple carotenoids in tomatoes and tomato products with confocal Raman micro-spectroscopy. Given the complexity of the carotenoid composition found in many bacteria [Takaichi, 2008b], a species-sensitive detection based on present carotenoids, carotenoid associations and conformation may well be possible given future research in wavelength-tunable Raman-systems and bacterial carotenoid expression.

SBR-1: In contrast to the results of SBR-0, the nitrification zone of the granules sampled from SBR-1 was formed by multiple, interwoven layers of two types of bacterial colonies of similar appearance (width 2 – 3 μm, length up to 5 μm), distinct only in their resonant Raman fingerprint: Type-I (green, spectrum (b1) in Fig. 5.3(b)) and the much rarer Type-II (red, spectrum (b2) in Fig. 5.3(b)). Bacteria of Type-I formed the main bulk of the micro-colonies (green), while Type-II (red) was much rarer and always surrounded by densely packed Type-I colonies without direct contact to the granule surface or water-filled channels (Fig. 5.2(f)). The main chromophore in both types was cytochrome-c, allowing for species-sensitive tracking and identification of the bacteria (see 5.2.3 and 5.2.4 below). Additional bacterial Raman spectra of cyt-c were detected underneath the nitrification zone (dark red, spectrum (b3) in Fig. 5.3(b)) and could be traced as deep as 80 μm into the granule. However, the quality of these spectra was not sufficient for a reliablel comparison to the bacteria found within the nitrification layer.

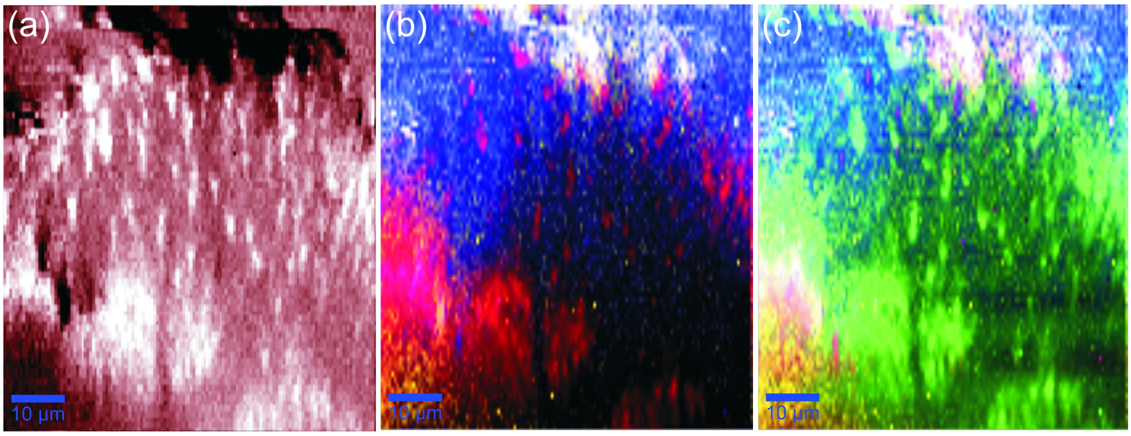

Figure 5.5: Spectral images based on resonance Raman spectra of an anammox granule swollen with water: full intensity as recorded (a), broadband filter image (b) categorizing bacteria (red, magenta), water (blue), low density biomass (dark blue), and fluorescence (white), and fingerprint image (c) showing primarily green microcolonies of the tracked bacteria Type-I (*Nitrosomonas communis*), very few bacteria of Type-II (red), and weak fluorescence (white) at the surface and right beneath the outer layer on the left. Filter spectra are the same as in Fig. 5.2(f) and are given in Fig. 5.3(b). (Figure first published in Kniggendorf and Meinhardt-Wollweber [accepted for publication w.m.r.].)

Variant thickness of the nitrification zone was typically caused by increased distance between the microcolonies of the outer layer, i.e. the space between the microcolonies widened and filled with water and low density biomass (blue and dark blue in Fig. 5.5(b)). This can be seen by comparing Figs. 5.2(d-f), 5.4, and 5.5. Also note that Type-II colonies (red) are virtually absent from the thick, water-rich nitrification zone seen in Fig. 5.5(c).

The existence of such a structured nitrifying layer of approx. 30 μm thickness (up to 100 μm) – as seen in Figs. 5.2(d-f) and 5.5 – on the surface of anammox granules of similar size was already reported by Nielsen et al. [2005], testing indiscriminant for *Nitrosomonas* (*N. europaea*, *N. eutropha*, *N. mobilis*, *N. halophila*) and betaproteobacterial aerobic ammonium oxidizers in general. While Nielsen et al. did not discuss channels and microcolonies present, both are clearly visible in their presented data obtained with FISH of PFA-fixed cryosections of sampled aggregates. In addition, co-existing microcolonies of different nitrifying bacteria (*Nitrosomonas europaea/eutropha*, *Nitrosococcus mobilis*) associated on the microscale were previously reported for example by Gieseke et al. [2003], who employed CLSM in combination with FISH on PFA-fixed thin sections. Interestingly, the *Nitrosomonas* colonies in their orthogonal representations of CLSM image stacks also show the astonishing ellipsoid form seen in Fig. 5.2(f), while colonies of *Nitrosococcus* appeared globular.

Microparticles

The outer layers of granules sampled from SBR-0 infested with purple bacteria contained a noticeable amount of microparticles – TiO_2 in rutile and anatase phase – of a size up to 10 μm (average diameter was approx. 3 μm). It is noteworthy, that these mineral particles have characteristic Raman lines at low wavenumbers, making them easily detectable even against increased fluorescence as seen in the cores of purple bacteria colonies. The Raman spectrum of rutile (spectrum (a3) in Fig. 5.3(a), red) consists of two lines at 447 and 613 cm^{-1}, while the spectrum of anatase (spectrum (a4) in Fig. 5.3(a), yellow) has four lines with the strongest line as low as 144 cm^{-1} (the others being at 394, 514, and 638 cm^{-1} respectively).

As can be seen in Fig. 5.2(c), the location of TiO_2 microparticles with respect to purple bacteria in the outer layer of granules sampled from SBR-0 appears to be dependent on the mineral phase. Microparticles of TiO_2 in anatase phase (yellow) were not in direct contact to bacterial microcolonies and often stuck in thick swaths of low density matter (dark blue in Fig. 5.2(b)), which might be comparable to the gelatinous matrix (probably EPS) seen in mats of phototrophic non-sulfur purple bacteria reported by Okubo et al. [2006]. Rutile microparticles (red in Fig. 5.2(c)) were typically densely populated with purple bacteria appearing almost embedded in large microcolonies of purple bacteria producing primarily spheroidene.

In contrast, the outer layer of granules sampled from SBR-1 held only a few rutile microparticles and virtually no anatase was detected throughout the monitoring (discounting free particles in the bulk water).

To the best of my knowledge, there is not yet a study reporting anything comparative to this for small microparticles in the range of 1 to 10 μm (or larger). However, Fang et al. [2010] reported anatase nanoparticles to cause cell shrinkage and membrane damage in *Nitrosomonas europaea*, independent of particle size (25 nm, 200 nm), while Liu et al. [2010] showed membrane damage caused in *Escherichia coli* by TiO_2, confirming bactericidal properties even in absence of UV irradiation. In addition, Johnston et al. [2009] reviewed the toxicity of TiO_2 in anatase and rutile phase on tissues and eukaryotic cells, finding the toxic potency of anatase considerably larger than that of rutile in most of the studies, some of which covered procaryotic cells as well. This may explain why anatase microparticles embedded in the outer layer were surrounded by low density matter keeping them separated from the purple bacteria microcolonies, while rutile crystals were found overgrown.

Considering the slow growth of *Nitrosomonas* (as identified in 5.2.4) in comparison to most purple bacteria and the aforementioned results of Fang et al., the toxic effects of rutile – and esp. of anatase – microparticles may have a more severe impact on microcolonies of *Nitrosomonas* than on microcolonies of purple bacteria. This may explain why there were few rutile and virtually no anatase microparticles embedded in the nitrifying layer of granules sampled from SBR-1, despite microparticles of both phases being present in the bulk water.

5.2.3 Bacterial Tracking – who stays?

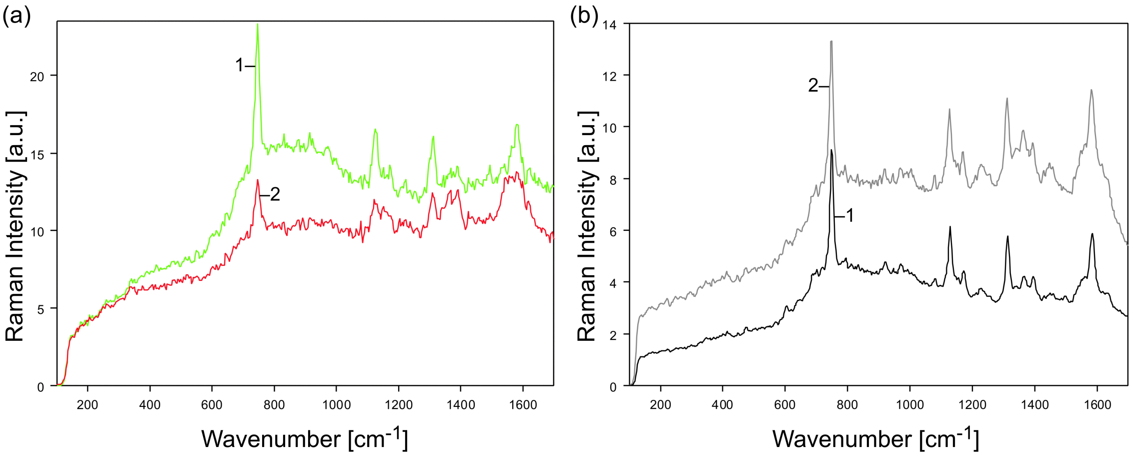

Figure 5.6: Resonant Raman spectra of bacteria containing cyt-c as main chromophore: Type-I (a1) and Type-II (a2) as recorded in the seed granules obtained from Rotterdam and *Nitrosomonas communis* Nm-02 (b1) and *Nitrosomonas europaea* Nm-50 (b2) as recorded from pure planctonic culture. (Figure first published in Kniggendorf and Meinhardt-Wollweber [accepted for publication w.m.r.].)

Two distinct Raman fingerprints of bacteria – Type-I and Type-II – were found in abundance in the anammox seed granules obtained from Rotterdam and tracked successfully throughout operation of SBR-1. As can be seen in 5.2.2, these bacteria formed the majority of microcolonies in the outer layer of granules sampled from SBR-1 (Figs. 5.2(f) and 5.5(c)) and of the seed granules themselves (data not shown).

Bacterial fingerprint Type-I (green) corresponded to spectrum (b1) and Type-II (red) to spectrum (b2) in Fig. 5.3(b). The respective Raman spectra recorded in the seed granules are given in Fig. 5.6.

Fig. 5.7 shows the hierarchical cluster analysis of a typical set of bacterial Raman single spectra extracted from various measurements made at different times during the operation of SBR-1 together with two sample spectra obtained from the seed granules (seed I and II). Resonant Raman spectra were identified with the fingerprint image filters (see 5.1.2) for Types-I and -II and exported from the respective spectral images (see 2.2).

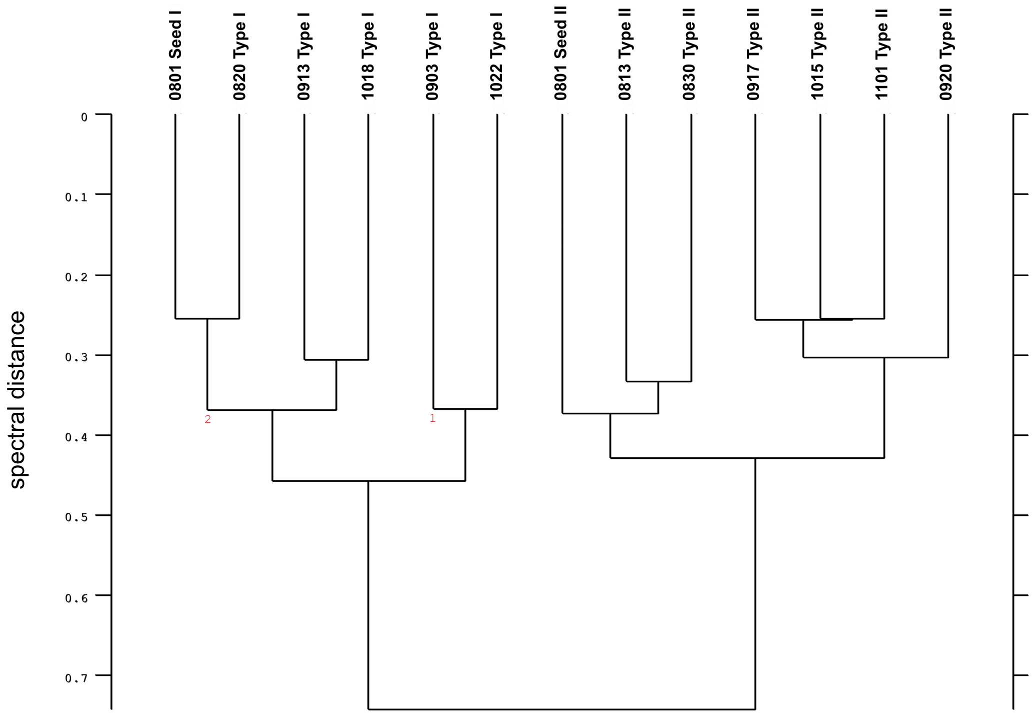

Figure 5.7: Hierarchical cluster analysis of resonant Raman spectra extracted from spectral images of the outer layer of anammox granules. Spectra are marked by date of measurement (month-day) and type as identified by the fingerprint filter. Seed I and II were recorded in the outer layer of seed granules. (Figure first published in Kniggendorf and Meinhardt-Wollweber [accepted for publication w.m.r.].)

Spectra with a suitable signal-to-noise ratio (see 3.1.2) were subsequently subjected to HCA as described in Chap. 4. Spectra were labeled with the date of the measurement (mmdd) and the type as identified by the fingerprint image filters. Type-I was later identified as *Nitrosomonas communis* and Type-II as probably being *Nitrosomonas europaea* (see 5.2.4).

As can be seen in Fig. 5.7, the two types of bacterial Raman spectra, classified as Type-I and -II by the fingerprint filters, were separated properly with a spectral distance larger than 0.7 between the branches I and II. Spectral distances between the components of a branch ranged from 0.25 to 0.46, with branch I forming a homogenous structure (spectrum 0903 has a stronger similarity to the seed 0801 and spectrum 0820 than to 1022, as indicated by the corrective numbers underneath the respective clusters) and branch II being divided into a starting cluster (0801, 0813, 0830) including the seed and spectra recorded within the first month of operation, and a cluster (0917, 0920, 1015, 1101) containing spectra recorded after 45 days of operation and later. This later cluster had a spectral distance of 0.45 from the starting cluster. This may indicate a change in the bacteria of Type-II between the 30th and the 45th day of operation, coinciding with the first time, denitrification exceeded deammonification in SBR-1 according to Wesoly [2009].
Similar time frames for biomass adaptation to changed environmental conditions were reported for example by Tsushima et al. [2007] for the simultaneous removal of ammonium and nitrite being detectable after startup, and Sliekers et al. [2002] for the formation

of biomass containing 45 % aerobic ammonium oxidizers, primarily *Nitrosomonas*, after aeration of a previously strict anoxic SBR.

The observed change in Type-II bacteria may be the result of phenotypic adaptation to the by then established microenvironment [Steward and Franklin, 2008] between the dense colonies of *Nitrosomonas communis* separating them from the bulk water.

5.2.4 Bacterial Identification – who's who?

The first bacterial fingerprint (Type-I) recorded from the seed granules was identified by OPUS Spectrum Comparison (see 2.3.3) with 94 % certainty as *Nitrosomonas communis* Nm-02 grown in planctonic culture. Spectrum comparison between the second bacterial fingerprint (Type-II) and the other available reference spectra found a best match with a spectral similarity of approx. 80 % to several *Nitrosomonas europaea* references (Nm-50, Nm-53, Nm-57), probably indicating a different strain of *Nitrosomonas europaea* or a phenotype variant from the phenotype observed in planctonic culture due to quorum sensing. Bacteria of this type were typically found surrounded by *Nitrosomonas communis* as identified by reference from planctonic culture (Type-I) and seldom or never had contact to water-rich areas of the biofilm.

For comparison, the similarity values found between spectra (S/N $\in$ [10,13]) recorded from pure cultures in 4.3 were 95 ± 4 % when belonging to the same strain and 84 ± 5 % when belonging to the same species, placing the values determined for spectra recorded from the biofilm clearly within the error margin for strain identification (Type-I, *Nitrosomonas communis* Nm-02). However, Type-II is at the lower margin of species identification and close to the similarity seen between different species (78 %), for which the error margin could not be determined due to lack of different species available in pure culture. Therefore, the identification of Type-II as an unreferenced strain of *Nitrosomonas europaea* may not be secure at this stage of knowledge, though the similar similarities of Type-II to the references of multiple *N. europaea* strains gives a strong indication for Type-II belonging to *N. europaea*.

Conclusion and Outlook

The aim of this work was to establish confocal resonance Raman micro-spectroscopy as a fast, non-destructive imaging technique for blind measurements of complex microbial biofilms and to provide precise procedures for its application. This was accomplished.
The project was motivated by the enormous complexity of biofilms and their amazing potential as an invaluable natural resource; a complexity that has primarily been met by slow, labor-intensive and destructive methods so far in standard microbiological analysis. Confocal Raman micro-spectroscopy combines the high spatial resolution of confocal microscopy with the specificity of Raman spectra. In employing molecular resonances of ubiquitous but specific chromophores, most notably cytochromes-c, the required measurement times are severely reduced in comparison to normal Raman spectroscopy (from 100 seconds and more down to 0.5 seconds (0.1 s in case of carotenoid chromophores)) and the spectral information is focused to molecules with known presence and function in the bacteria.

In this work, confocal resonance Raman micro-spectroscopy at 532 nm excitation was examined for its analyzing capabilities of complex multi-species biofilms and bacteria. Target chromophores were cytochromes-c and -cbb$_3$, as well as the carotenoids spheroidene, spirilloxanthin, and neurosporene (Chap. 3 and 5.2.1). Procedures for reliable spectrum comparison, allowing the identification of bacteria at strain level, and hierarchical cluster analysis for identifying bacterial relations even among unknown species, have been developed and tested successfully on pure bacteria cultures (see Chap. 4). The developed techniques were then tested by analyzing the outer layer of biofilm granules sampled from two labscale sequencing batch reactors for experimental biological wastewater treatment, fully characterized in the doctorate thesis of Wesoly [2009] (Chap. 5).

Key features of confocal resonance Raman micro-spectroscopy

Confocal resonance Raman micro-spectroscopy, as established in this work, allows the non-invasive optical analysis of living, undisturbed wet biofilms of up to 80 μm thickness, without requiring sample fixation or treatment with fluorescent probes, labels or stains. A spatial resolution at cell size is combined with excitation times between 0.1 and 0.5 s for a single spectrum. Since Raman spectra – and therefore the chromophores – can be identified after the measurement is completed, measuring fully unknown samples (blind measurements) is possible (5.2).

Confocal resonance Raman micro-spectroscopy does allow the analysis of biological as well as mineral components of the sample in the same measurement. EPS is detected as unspecific „low density matter“ (5.2.2).

The autofluorescent background, seen in most spectra recorded from biofilms, is analyzed with broadband filters, allowing the discrimination of bacteria with unknown Raman spectra, thus preventing false negatives. Background analysis provides information about biofilm morphology even in the absence of resonant Raman chromophores (5.1.1).

The method is partially compatible with two of the three tested soft fixation methods: ethanol- and formaldehyde solution. However, ethanol fixation leads to increasing deterioration of the spectra. Formaldehyde solution reduces signal intensity at higher wavenumbers, thus deforming the spectra, especially when the sample is in contact with adhesive surface coatings (3.3).

Results obtainable with confocal Raman micro-spectroscopy for biofilm analysis are dependent on the taxonomic value of the chromophores present in the bacteria. While bacterial relations can be determined among bacteria strains expressing the same set of chromophores, a mutation causing the production of a different chromophore in one of the strains can not be identified as belonging to the same species (4.3).

In addition, the technique is sensitive to fluorescence, rendering it incompatible with many of the current standard methods for biofilm analysis relying on fluorescent probes.

How does confocal resonance Raman microscopy compare with other methods proposed for biofilm analysis?

To date, very few techniques for blind, label-free imaging of native, undisturbed biofilm have been reported: most notably, **infrared absorption** and **normal Raman** (NR) spectroscopy, often in combination with confocal microscopy, have been employed for several biofilm and bacteria studies [Harz et al., 2008]. However, long exposure times (100 s and more) and high variability of bacterial Raman spectra due to variant environmental conditions and metabolic variants of the cells pose significant challenges for mapping biofilms as well as identifying bacteria [Harz et al., 2008].

In this work, we showed that resonance Raman spectroscopy as presented in this work relies primarily on specific ubiquitous molecules (chromophores) produced naturally by the bacteria. The resonant excitation of these chromophores allows for significantly shorter exposure times (1 s and less) and reduces the variability of the spectra to metabolic changes of the bacterial cell directly affecting the chromophores. The reliance on chromophores restricts specificity to the specificity of the chromophore within the bacteria and also dictates the excitation wavelength, thus affecting the compatibility with methods such as **fluorescence in situ hybridization (FISH)**, which require fluorescent staining [Neu et al., 2010]. Most if not all, available fluorescent stains do not allow for subsequent (resonant) Raman measurements with visible excitation. The only combination of Raman and FISH reported by Huang et al. [2007] relied on the detection of ^{13}C labeled cells, trading most – if not all – of the advantages of Raman micro-spectroscopy in regard of non-invasive measurements of native, undisturbed samples.

Rapid surface enhanced Raman scattering (SERS) was used by Ivleva et al. [2010] in combination with normal Raman for the in situ chemical characterization of complex biofilms grown on marked glass slides, mapping several SERS fingerprints indicative of polysaccharides and proteins. The presented raster maps of 60 x 60 μm^{2} with a spatial resolution of 3 μm were recorded with an excitation time of 1 s per SERS spectrum, bringing this technique in the same range of spatial resolution and recording time as the resonance Raman measurements in this work. However, the requirement of silver nanoparticles as SERS substrate may limit this technique to end-point analyses, given that silver nanoparticles of similar size have been reported by Liang et al. [2010] to have a severe negative impact on nitrifying bacteria in activated sludge, leading to significant nitrification inhibition and changes in the communal composition of the present bacteria.

Optical coherence tomography (OCT) has been reported by Haisch and Niessner [2007] for online, in vivo and in situ visualization of three-dimensional biofilm density structures with a 10 μm resolution and transient processes with an impressive temporal resolution between 1 s and a few minutes for complete images. However, while discrimination between bacterial matter and larger microparticles (diameter > 10 μm) and even different types of microparticles may be possible due to different particle densities, the discrimination between different types of bacteria and thus the subsequent identification of bacteria as shown in this work with resonance Raman micro-spectroscopy is not possible with OCT.

How to continue?

Confocal resonance Raman micro-spectroscopy proved to be a powerful tool for analyzing complex biological samples such as multi-species biofilms, by targeting the ubiquitous cytochromes-c. Other techniques proposed for this task were either more invasive (SERS) or significantly slower (NR). However, the impressive capabilities of OCT for online, three-dimensional visualization of biofilm densities and the observation of transient processes in the biofilm, as reported by Haisch and Niessner [2007] would be a true and fascinating expansion. Biofilms with rapidly changing morphology, sometimes turning from firm granules to floating flocs cause significant problems (overflowing) in some wastewater treatment plants (Dr. Susan Turner, CMI Director, School of Biological Sciences, University of Auckland, private communication). A **combination of OCT and confocal resonance Raman micro-spectroscopy** might allow the analysis of the microbial dynamics underneath such dramatic events in the biofilm.

Further application of resonance Raman spectroscopic analysis of biofilms is especially promising in the biomedical context. Extensive works on the hemes in hemoglobin and myoglobin with excitation wavelengths in the UV give hope for the existence of biomedically relevant chromophores [Asher, 1993b]. Confocal resonance Raman micro-spectroscopy on cytochromes-c proved to be a fast and reliable source of indepth information on structure and bacterial content of the indispensable biofilms for wastewater treatment. However, biofilms of different organisms pose an increasing problem in medical care, due to their unusual high tolerance to antibiotics and the immune system of the patient. **Confocal resonance Raman micro-spectroscopy on chromophores present in critical medical biofilms** may allow a deeper understanding of their properties and how they may be treated. For this, a study on the chromophores present in medically critical biofilms would be a good start. If strain specific analysis proves possible, a faster, more precise treatment of affected patients may be achieved.

In this work, confocal resonance Raman micro-spectroscopy was successfully used for the identification of bacteria and the determination of their taxonomical relation (4.3). However, time and scope of this project did not allow to determine the full range of spectroscopic taxonomy. An indepth **study of a full order of bacteria** would allow **to determine the taxonomic range** in which the method returns reliable information, thus answering the question of whether or not it is possible to determine not only species and strain, but also genus, family or order with confocal resonance Raman micro-spectroscopy. The small order of *Nitrosomonadales*, consisting of few, known and taxonomically described proteobacteria (including *Nitrosomonas*), would be a useful target for such a study.

List of Figures

0.1 Surface of an anaerob ammonium oxidizing (ANAMMOX) biofilm granule. Light microscopic image taken with the CRM 200 (white light illumination; Nikon CFI Fluor water-immersion objective). 1

1.1 Energy-level diagrams of IR, Raman, and absorption/fluorescence events . 6

2.1 Confocal Raman microscopy workstation with the CRM 200 and SDU-1 at the institute of biophysics. 9

2.2 Principal setup used for confocal Raman micro-spectroscopy. 10

2.3 Setup of the spectrometer-detection-units. 12

2.4 SBR 20

2.5 Flasks with cultures of purple non-sulfur bacteria in harvesting condition. . 22

3.1 Structure of a typical bacterial resonance Raman spectrum. 26

3.2 Reference spectrum (average of 100 single spectra of S/N $\geq$ 10) and single spectrum (S/N = 11.5) of *Nitrosomonas communis* Nm-02 in vector normalization. (Figure first published in Kniggendorf et al. [2011a].) 28

3.3 Carbonate crystals in *Nitrosomonas eutropha*. 29

3.4 Phase-contrast micrographs of growing PNS type strain cultures showing different cell shape and size. 29

3.5 Raman and absorption spectra of DSM 123, DSM 158, and DSM 467. . . . 30

3.6 Raman spectrum of DSM 158^T and DSM 2340^T 33

3.7 Raman and absorption spectra of cytochrome-c. 34

3.8 Raman spectrum of *Nitrosomonas communis* Nm-02 and cytochrome-c. . . 34

3.9 Raman spectra of *Nitrosomonas*. 35

3.10 Comparison of the resonant Raman spectra of native and fixed bacteria. . . 39

3.11 Effects of extended fixative exposure on the resonant Raman spectrum of bacteria 40

3.12 Development of fluorescent background intensity in the Raman spectrum of *Rhodobacter sphaeroides* 158 measured at 1,070 cm^{-1} as a function of the time the sample was exposed to the fixative. (Figure first published in Kniggendorf et al. [2011b].) 41

3.13 Comparison of resonant Raman spectra of native or fixed bacteria recorded on microscope slides with or without poly-L-lysine adhesive coating. 42

3.14 Resonant Raman spectra of native and PFA fixed *Rhodobacter sphaeroides* 158 mounted on uncoated (a) and poly-L-lysine coated (b) microscope slides. (Figure first published in Kniggendorf et al. [2011b]) 42

3.15 Resonant Raman spectrum of PFA-fixed *Rhodopseudomonas palustris* 123 (a) and *Rhodospirillum rubrum* 467 (b) mounted on uncoated and poly-L-lysine coated microscope slides. (Figure first published in Kniggendorf et al. [2011b]). 43

4.1 Reference spectra for HCA algorithm comparison. 48

4.2 Reference dendrogram. 48

4.3 Reference spectrum (average of 100 single spectra of S/N $\geq$ 10) and single spectrum (S/N = 11.5) of *Nitrosomonas communis* Nm-02 in vector normalization. (Figure first published in Kniggendorf et al. [2011a].) 50

4.4 Weighted-Average-Linkage dendrogram 52

4.5 Ward dendrogram of Heterogeneity 53

4.6 Influence of spectrum quality on HCA 54

4.7 Raman spectrum of *Rhodobacter sphaeroides* DSM 158^{T} and DSM 2340^{T} 57

4.8 HCA of Raman spectra recorded from *Nitrosomonas* and the carotinoids-free mutant of *Rhodobacter sphaeroides* 58

5.1 Filter concepts for spectral imaging 63

5.2 Spectral imaging based on (Resonance) Raman spectra. 65

5.3 (Resonant) Raman spectra as recorded. 66

5.4 Image stack 67

5.5 Anammox granule swollen with water. 69

5.6 Resonant Raman spectra of bacteria containing cyt-c as main chromophore 71

5.7 Hierarchical cluster analysis of resonant Raman spectra recorded from anammox granules 72

Bibliography

Rudolf I. Amann, Wolfgang Ludwig, and Karl-Heinz Schleifer. Phylogenetic identification and in situ detection of individual microbial cells without cultivation. *Microbiological Reviews*, 59(1):143–169, 1995.

Sanford A. Asher. Uv resonance raman spectroscopy for analytical, physical, and biophysical chemistry. *Analytical Chemistry*, 65(2):59–66, 1993a.

Sanford A. Asher. Uv resonance raman spectroscopy (part 2). *Analytical Chemistry*, 65 (4):201–209, 1993b.

S. A. Ballesteros, J. Chirife, and J. P. Bozzini. Antibacterial effects and cell morphological changes in *Staphylococcus aureus* subjected to low ethanol concentrations. *Journal of Food Science*, 58:435–438, 1993.

Iwona B. Beech and Jan Sunner. Biocorrosion: towards understanding interactions between biofilms and metals. *Current Opinion in Biotechnology*, 15:181–186, 2004.

Gabriel Bitton. *Wastewater Microbiology*. Wiley-Blackwell, 2011. ISBN 9780470630334.

Alois Bonifacio, Sara Finaurini, Christoph Krafft, Silvia Parapini, Donatella Taramelli, and Valter Sergo. Spatial distribution of heme species in erythocytes infected with *Plasmodium falciparum* by use of resonance raman imaging and multivariate analysis. *Analytical Bioanalytical Chemistry*, 392:1277–1282, 10 2008.

G. Britton. Chapter 2: Uv/visible spectroscopy. In G. Britton, S. Liaaen-Jensen, and H. Pfander, editors, *Carotenoids Volume 1B: Spectroscopy*, volume 1B, pages 13–62. Birkhäuser (Basel), 1995.

G. Britton. Overview of carotenoid biosynthesis. In G. Britton, S. Liaaen-Jensen, and H. Pfander, editors, *Carotenoids Volume 3: Biosynthesis and Metabolism*, volume 3, pages 13–147. Birkhäuser (Basel), 1998.

Bruker Bruker GmbH. *OPUS Version 5.5 Referenzhandbuch*. Bruker GmbH, Ettlingen, Germany, 2004.

Germany Bruker GmbH, Ettlingen. *OPUS Version 5.5 IDENT*. Bruker GmbH, Ettlingen, Germany, 2004.

Richard J. Cogdell, Andrew Gall, and Jürgen Köhler. The architecture and function of the light-harvesting apparatus of purple bacteria: from single molecules to *in vivo* membranes. *Quarterly Reviews of Biophysics*, 39(3):227–324, 10 2006.

S. P. Denyer. Mechanisms of action of antibacterial biocides. *International biodeterioration and biodegradation*, 35:227–245, 1995.

S. P. Denyer and G. S. A. B. Steward. Mechanisms of action of disinfectants. *International biodeterioration and biodegradation*, 41:261–268, 1998.

R. T. Downs. The rruff project: an integrated study of the chemistry, crystallography, raman and infrared spectroscopy of minerals. *Program and Abstracts of the 19th General Meeting of the International Mineralogical Association in Kobe, Japan*, 2006.

E. Drenkard and F. M. Ausubel. *Pseudomonas* biofilm formation and antibiotic resistance are linked to phenotypic variation. *Nature*, 416:740–743, 2002.

Daniel D. Eads, Chris Moser, Milton E. Blackwood jr., Ching-Yao Lin, Leslie Dutton, and Thomas G. Spiro. Selective enhancement of resonance raman spectra of separate bacteriopheophytins in *Rb. sphaeroides* reaction centers. *Biopolymers (Biospectroscopy)*, 57:64–74, 2000.

X. Fang, R. Yu, B. Li, P. Somasundaran, and K. Chandran. Stresses exerted by zno, ceo$_2$, and anatase tio$_2$ nanoparticles on the *Nitrosomonas europaea*. *Journal of Colloid and Interface Science*, 348:329–334, 2010.

Hans-Curt Flemming. The perfect slime. *Colloids and Surfaces B: Biointerfaces*, doi:10.1016/j.colsurfb.2011.04.025, 2010.

Cecil H. Fox, Frank B. Johnson, John Whiting, and Peter P. Roller. Formaldehyde fixation. *The Journal of Histochemistry and Cytochemistry*, 33(8):845–853, 1985.

J. M. Friedman and D. L. Rousseau. Simultaneous observation of coherent and incoherent resonant re-emission in the condensed phase. *Chem. Phys. Letters*, 55:488–492, 1978.

A. Gieseke, K. Bjerrum, M. Wagner, and R. Amann. Structure and activity of multiple nitrifying bacterial populations co-existing in a biofilm. *Environmental Microbiology*, 5 (5):355–369, 2003.

C. Haisch and R. Niessner. Visualisation of transient processes in biofilms by optical coherence tomography. *Water Research*, 41:2467–2472, 2007.

Luanne Hall-Stoodley, J. William Costerton, and Paul Stoodley. Bacterial biofilms: From the natural environment to infectious diseases. *Nature Reviews: Microbiology*, 2:95–108, 2004.

M. Harz, P. Rösch, and J. Popp. Vibrational spectroscopy - a powerful tool for the rapid identification of microbial cells at the single-cell level. *Cytometry Part A*, 75A:104–113, 2008.

S. Hu, I. K. Morris, J. P. Singh, K. M. Smith, and T. G. Spiro. Complete assignment of cytochrome c resonance raman spectra via enzymatic reconstitution with isotopically labeled hemes. *Journal of the American Chemical Society*, 115(26):12446–12458, 1993.

W. E. Huang, K. Stoecker, R. Griffiths, L. Newbold, H. Daims, A. S. Whiteley, and M. Wagner. Raman-fish: combining stable-isotope raman spectroscopy and fluorescence in situ hybridization for the single cell analysis of identity and function. *Environmental Microbiology*, 9(8):1878–1889, 2007.

J. F. Imhoff. The phototrophic alpha-proteo bacteria. In M. Dworkin, S. Falkow, E. Rosenberg, K.-H. Schleifer, and E. Stackebrandt, editors, *The procaryotes*, pages 41–64. Springer (New York), 2006.

N. P. Ivleva, M. Wagner, A. Szkola, H. Horn, R. Niessner, and C. Haisch. Label-free in situ sers imaging of biofilms. *Journal of Physical Chemistry B*, 114:10184–10194, 2010.

Algirdas J. Jesaitis, Michael J. Franklin, Deborah Berklung, Maiko Sasaki, Connie I. Lord, Justin B. Bleazard, James E. Duffy, Haluk Beyenal, and Zbigniew Lewandowski. Compromised host defense on *Pseudomonas aeruginosa* biofilms: Characterization of neutrophil and biofilm interactions. *Journal of Immunology*, 171:4329–4339, 2003.

Long Jin and Ricardo V. Lloyd. In situ hybridization: Methods and applications. *Journal of Clinical Laboratory Analysis*, 11:2–9, 1997.

H. J. Johnston, G. R. Hutchinson, F. M. Christensen, S. Peters, S. Hankin, and V. Stone. Identification of the mechanisms that drive the toxicity of tio_2 particulates: the contribution of physicochemical characteristics. *Particle and Fibre Toxicology*, 6(33), 2009.

Ann-Kathrin Kniggendorf and Merve Meinhardt-Wollweber. Of microparticles and bacteria identification - resonance raman micro-spectroscopy as a tool for biofilm analysis. *Water Research*, accepted for publication w.m.r. accepted for publication.

Ann-Kathrin Kniggendorf, Tobias William Gaul, and Merve Meinhardt-Wollweber. Hierarchical cluster analysis of microorganisms: An algorithm assessment for resonance raman spectra. *Applied Spectroscopy*, 65(2):165–173, 2011a.

Ann-Kathrin Kniggendorf, Tobias William Gaul, and Merve Meinhardt-Wollweber. Effects of ethanol, formaldehyde, and gentle heat fixation in confocal resonance raman microscopy of purple nonsulfur bacteria. *Microscopy Research and Technique*, 74:177–183, 2011b.

H.-P. Koops, B. Böttcher, U. C. Möller, A. Pommerening-Röser, and G. Stehr. Classification of eight new species of ammonia-oxidizing bacteria: Nitrosomonas communis sp. nov., nitrosomonas ureae sp. nov., nitrosomonas aestuarii sp. nov., nitrosomonas marina sp. nov., nitrosomonas nitrosa sp. nov., nitrosmonas eutropha sp. nov., nitrosomonas oligotropha sp. nov., and nitrosomonas halophila sp. nov. *Journal of General Microbiology*, 137:1689–1699, 1991.

Y. Koyama. Resonance raman spectroscopy. In G. Britton, S. Liaaen-Jensen, and H. Pfander, editors, *Carotenoids Volume 1B: Spectroscopy*, volume 1B, pages 135–146. Birkhäuser (Basel), 1995.

E. L. Larson and H. E. Morton. Alcohols. In S. Block, editor, *Disinfection, sterilization, and preservation*, pages 191–203. Lea and Febinger (Philadelphia), 1991.

Z. Liang, A. Das, and Z. Hu. Bacterial response to a shock load of nanosilver in an activted sludge treatment system. *Water Research*, 44:5432–5438, 2010.

P. Liu, W. Duan, Q. Wang, and X. Li. The damage of outer membrane of escherichia coli in the presence of tio$_2$ combined with uv light. *Colloids and Surfaces B*, 78:171–176, 2010.

Derek A. Long. *The Raman Effect*. John Wiley and Sons Ltd. (Chichester), 2002. ISBN 0-471-49028-8.

Chris Mackenzie, Jesus M. Eraso, Madhusudan Choudhary, Jung Hyeob Roh, Xiaohua Zeng, Patrice Bruscella, Ágnes Puskás, and Samuel Kaplan. Postgenomic adventures with *Rhodobacter sphaeroides*. *Annual Review of Microbiology*, 61:283–307, 6 2007.

W. Manz, R. Amann, W. Ludwig, M. Wagner, and K.-H. Schleifer. Phylogenetic oligodeoxynucleotide probes for the major subclasses of proteobacteria: problems and solutions. *Systematic Applied Microbiology*, 15:593–600, 1992.

Daniel Mazia, Gerald Schatten, and Winfield Sale. Adhesion of cells to surfaces coated with polylysine. *Journal of Cell Biology*, 66:198–200, 7 1975.

Bernhard Metz, Gideon F. A. Kersten, Peter Hoogerhout, Humphrey F. Brugghe, Hans A. M. Timmermans, Ad de Jong, Hugo Meiring, Jan ten Hove, Wim E. Hennink, Daan J. A. Crommelin, and Wim Jiskoot. Identification of formaldehyde-induced modifications in proteins. *The Journal of Biological Chemistry*, 279(8):6235–6243, 2 2004.

Geoffrey R. Moore and Graham W. Pettigrew. *Cytochromes c: Evolutionary, Structural and Physicochemical Aspects*. Springer Series in Molecular Biology. Springer Verlag, New York, 1990. ISBN 0-387-50852-X.

T. R. Neu, B. Manz, F. Volke, J. J. Dynes, A. P. Hitchcock, and J. R. Lawrence. Advanced imaging techniques for assessment of structure composition and function in biofilm systems. *FEMS Microbiology Ecology*, 72:1–21, 2010.

M. Nielsen, A. Bollmann, O. Sliekers, M. Jetten, M. Schmid, M. Strous, I. Schmidt, L. Hauer Larsen, L. P. Nielsen, and N. P. Revsbach. Kinetics, diffusional limitation and microscale distribution of chemistry and organisms in a canon reactor. *FEMS Microbiology Ecology*, 51:247–256, 2005.

Y. Okubo, H. Furamata, and A. Hiraishi. Characterization of phototrophic purple nonsulfur bacteria forming colored microbial mats in a swine wastewater ditch. *Applied and Environmental Microbiology*, 72(9):6225–6233, 2006.

George A. O'Toole and Roberto Koller. Flagellar and twitching motility are necessary for pseudomonas aeruginosa biofilm development. *Molecular Microbiology*, 30(2):295–304, 2002.

James Pawley. *Handbook of Biological Confocal Microscopy*. Springer Science+Business Media, LLC (New York), 3 edition, 2006.

Graham W. Pettigrew and Geoffrey R. Moore. *Cytochromes c: Biological Aspects*. Springer Series in Molecular Biology. Springer Verlag, New York, 1987. ISBN 0-387-17843-0.

I. Primpas, M. Karydis, and G. Tsirtsis. Assessment of clustering algorithms in discriminating eutrophic levels in coastal waters. *Global NEST Journal*, 10(3):359–365, 2008.

P. D. A. Pudney, L. Gambelli, and M. J. Gidley. Confocal raman microspectroscopic study of the molecular status of carotenoids in tomato fruits and foods. *Applied Spectroscopy*, 65(2):127–134, 2011.

Robert Riding. The term stromatolite: towards an essential definition. *Lethaia*, 32:321–330, 1999.

A. D. Russel. Principles of antimicrobial activity. In S. Block, editor, *Disinfection, sterilization, and preservation*, pages 27–58. Lea and Febinger (Philadelphia), 1991.

A. D. Rutala. Draft guideline for selection and use of disinfectants. *American Journal of Infection Control*, 17:24–38, 1989.

Daniela Santos Pontes, Claudia Iracema Lima-Bittencourt, Edmar Chartone-Souza, and Andrea Maria Amaral Nascimento. Molecular approaches: advantages and artifacts in assessing bacterial diversity. *Journal for Industrial Microbiology and Biotechnology*, 34:463–473, 2007.

K. Sauer, A. K. Camper, G. D. Ehrlich, J. W. Costerton, and D. G. Davies. Pseudomonas aeruginosa displays multiple phenotypes during development as a biofilm. *Journal of Bacteriology*, 184:1140–1154, 2002.

T. Schwartz, C. Jungfer, S. Heißler, F. Friedrich, W. Faubel, and U. Obst. Combined use of molecular biology taxonomy, raman spectrometry, and esem imaging to study natural biofilm grown on filter materials at waterworks. *Chemosphere*, 77:249–257, 2009.

Carsten U. Schwermer, Gaute Lavik, Raeid M. M. Abed, Braden Dunsmore, Timothy G. Ferdelman, Paul Stoodley, Armin Gieseke, and Dierk de Beer. Impact of nitrate on the structure and function of bacterial biofilm communities in pipelines used for injection of seawater into oil fields. *Applied Environmental Microbiology*, 74(9):2841–2851, 2008.

Robert A. Scott and A. Grant Mauk. *Cytochrome c - A Multidisciplinary Approach*. University Science Books (Sausalito, California), 1996. ISBN 0-935702-33-4.

S. Sharma. *Applied Multivariate Techniques*. John Wiley and Sons (New York), 2006.

J. A. Shelnutt, D. L. Rousseau, Judy K. Dethmers, and E. Margoliash. Protein influence on the heme in cytochrome c: Evidence from raman difference spectroscopy. *Proc. Natl. Acad. Sci. USA: Biophysics*, 76(8):3865–3869, August 1979.

Elie A. Shneour. Carotenoid pigment conversion in *Rhodopseudomonas spheroides*. *Biochimica et Biophysica Acta*, 62:534–540, 1962.

A. O. Sliekers, N. Derwort, J. L. Campos Gomez, M. Strous, J. G. Kuenen, and M. S. M. Jetten. Completely autotrophic nitrogen removal over nitrite in one single reactor. *Water Research*, 36:2475–2482, 2002.

James T. Staley. The bacterial species dilemma and the genomic-phylogenetic species concept. *Philosophical Transactions of the Royal Society B*, 361:1899–1909, 2006.

P. S. Steward and M. J. Franklin. Physiological heterogeneity in biofilms. *Nature Reviews Microbiology*, 6:199–210, 2008.

S. Takaichi. Carotenogenesis. In C. N. Hunter, F. Daldal, M. C. Thurnauer, and J. T. Beatty, editors, *Advances in Photosynthesis and Respiration Vol. 28: The Purple Phototrophic Bacteria*, volume 28, pages 101–111. Springer(Dordrecht), 2008a.

S. Takaichi. Carotinoids in purple bacteria. In C. N. Hunter, F. Daldal, M. C. Thurnauer, and J. T. Beatty, editors, *Advances in Photosynthesis and Respiration Vol. 28: The Purple Phototrophic Bacteria*, volume 28, pages 111–117. Springer(Dordrecht), 2008b.

I. Tsushima, Y. Ogasawara, T. Kindaichi, H. Satoh, and S. Okabe. Development of high-rate anaerobic ammonium-oxidizing (anammox) biofilm reactors. *Water Research*, 41: 1623–1634, 2007.

H. C. Tung, N. E. Bramall, and P. B. Price. Microbial origin of excess methane in glacial ice and implications for life on mars. *Proceedings of the National Academy of Sciences of the United States of America*, 102(51):18292–18296, 2005.

W. R. L. van der Star, A. I. Miclea, U. G. J. M. van Dongen, G. Muyzer, C. Picioreanu, and M. C. M. van Loosdrecht. The membrane bioreactor: a novel tool to grow anammox bacteria as free cells. *Biotechnology Bioengineering*, 101:286–294, 2008.

Constantinos Varotsis, Gerald T. Babcock, J. Arturo Garcia-Horseman, and Robert B. Gennis. Resonance raman spectroscopy of the heme groups of cytochrome cbb_3 in *Rhodobacter sphaeroides*. *The Journal of Physical Chemistry*, 99(46):16817–16820, 1995.

Virginia Museum of Natural History. Two-ton, 500 million-year-old fossil of stromatolite discovered in virginia, u.s.. *ScienceDaily*, Retrieved May 6, 2011, 2008.

M. Wagner, N. P. Ivleva, C. Haisch, R. Niessner, and H. Horn. Combined use of confocal laser scanning microscopy (clsm) and raman microscopy (rm): investigation on eps-matrix. *Water Research*, 43:63–76, 2009.

Joe H. Ward, jr. Hierarchical grouping to optimize an objective function. *Journal of the American Statistical Association*, 58(301):236–244, 3 1963.

Ilona Wesoly. *Betriebsstrategien für den Anammox-Prozess in Sequencing Batch Reaktoren*. PhD thesis, Technische Universität Berlin, 2009.

T. Wilson. *Confocal Microscopy*. Academic Press, 1990.

WITec WITec GmbH. *WITec Project User Manual*. WITec GmbH, Ulm, Germany, 2005.

S. Wuertz, S. Okabe, and M. Hausner. Microbial communities and their interactions in biofilm systems: an overview. *Water Science and Technology*, 49(11-12):327–336, 2004.

Curriculum Vitae

name	Ann-Kathrin Kniggendorf
place, date of birth	Hannover, Germany, January 27, 1972
school career	1979 – 1983: primary school in Hildesheim 1983 – 1985: Orientierungsstufe in Hildesheim 1985 – 1993: Scharnhorst Gymnasium Hildesheim
school qualifications	Abitur
university career	1993 – 2005: study of physics at the university of Hannover subjects: quantum- and non-linear optics, optics, biophysics, (elementary study in chemistry) 2005 – 2007: dissertation project „Aufbau und Optimierung eines gepulsten Festkörperlasersystems zur multimethodigen optischen Spektroskopie an biologischen Proben in situ und in vivo zwischen 210 nm und 2,1 μm“. Change of dissertation project due to lack of funding in Autumn 2007 2007 – 2010: doctorate studies “Resonance Raman Micro-Spectroscopy for Analyzing Bacterial Biofilms“ as part of DFG-Projekt AN 712/1-5 „In situ Identifikation und Aktivitätsmessung von mikrobiellen Aggregaten in der biologischen Abwasserreinigung“ 2011 (until June): Promotionsabschlussförderung
university qualifications	diploma in physics

Publications and Presentations

Publications

REVIEWED

A.-K. Kniggendorf, Merve Meinhardt-Wollweber. „Of Microparticles and Bacteria Identification – Resonance Raman Micro-Spectroscopy as a Tool for Biofilm Analysis“ accepted for publication with minor revisions in Water Research, May 2011 [Kniggendorf and Meinhardt-Wollweber, accepted for publication w.m.r.]

A.-K. Kniggendorf, Tobias W. Gaul, Merve Meinhardt-Wollweber. „Hierarchical Cluster Analysis of Microorganisms: an algorithm assessment for Resonance Raman Spectra“ in Applied Spectroscopy 65(2), pp. 165-172, 2011 [Kniggendorf et al., 2011a]

A.-K. Kniggendorf, Tobias W. Gaul, Merve Meinhardt-Wollweber. „Effects of Ethanol, Formaldehyde, and Gentle Heat Fixation in Confocal Resonance Raman Microscopy of Purple NonSulfur Bacteria“ in Microscopy Research and Technique 74, pp. 177-183, 2011 [Kniggendorf et al., 2011b] (earlier published online as DOI 10.1002/jemt.20889, 2010)

A.-K. Kniggendorf, Diplomarbeit

INVITED

A.-K. Kniggendorf, Angelika Anders-von Ahlften. „Konfokale Resonanz-Raman-Mikroskopie. Präparationsfreie in situ Analyse von Bakterien in komplexen mikrobiellen Aggregaten“ in BIOforum 4/2008, pp. 39-41, GIT Verlag GmbH & Co. KG, Darmstadt

NON-REVIEWED (ABSTRACTS, ETC.)

K. Hauer, D. B. Meisinger, M. Pavlekovic, S. H. Thomas, A.-K. Kniggendorf, J. Chee-Sanford, R. Sandford, C. A. Lebrón, W. Liebl, F. E. Loeffler, N. M. Lee. „Novel tools for in situ detection of biodiversity and function of dechlorinating and uranium-reducing bacteria in contaminated environments“ in GCA (Geochimica et Cosmochimica Acta), Volume 73, Issue 13 Supplement 1 (June 2009). p. A502

A.-K. Kniggendorf, J. Haneke, I. Wesoly, T. Gaul, Angelika Anders. „Analyzing Bacterial Adhesion Forcess Within Anaerobic Granules by Confocal Resonance Raman Microscopy" in Abstract Handbook of Biofilm Technologies Conference, 8 - 10 January 2008, Singapore.

T. Gaul, A.-K. Kniggendorf, I. Wesoly, J. Haneke, M. Steffens, S. Kunst, R. Pätzold, A. Anders. „Starting up Anammox reactors: How Anammox organisms may be purposefully enriched and detected" in Abstract Handbook of Biofilm Technologies Conference, 8 - 10 January 2008, Singapore.

conference presentations

(* indicates speaker)

2009: K. Hauer, D. B. Meisinger, M. Pavlekovic, S. H. Thomas, A.-K. Kniggendorf, J. Chee-Sanford, R. Sandford, C. A. Lebrón, W. Liebl, F. E. Loeffler, N. M. Lee*. „Novel tools for in situ detection of biodiversity and function of dechlorinating and uranium-reducing bacteria in contaminated environments" at Goldschmidt Conference 2009

2008: A.-K. Kniggendorf*, J. Haneke, I. Wesoly, T. Gaul, Angelika Anders. „Analyzing Bacterial Adhesion Forcess Within Anaerobic Granules by Confocal Resonance Raman Microscopy" at Biofilm Technologies Conference, 8 - 10 January 2008, Singapore.

2008: T. Gaul*, A.-K. Kniggendorf, I. Wesoly, J. Haneke, M. Steffens, S. Kunst, R. Pätzold, A. Anders. „Starting up Anammox reactors: How Anammox organisms may be purposefully enriched and detected" at Biofilm Technologies Conference, 8 - 10 January 2008, Singapore.

2008: Wiebke Berndt*, Ann-Kathrin Kniggendorf, Ilona Wesoly, Angelika Anders-von Ahlften. „Computergestützte Auswertung von Messungen mit lasergestützter konfokaler Raman-Mikroskopie von Proben aus dem Life Science-Bereich". DPG Tagung Regensburg 2008, UP 10: Neuartige Verfahren in der Umweltphysik

2004: Ann-Kathrin Kniggendorf*, Merve Meinhardt, Ronald Krebs, Holger Lubatschowski, Angelika Anders. „Erzeugung von Nanosekundenpulsen im UV-A Regime mit einem bei 266 nm gepumpten optisch parametrischen Oszillator". DPG Tagung München 2004, Vortrag Q8.4

Further information: http://www.researchgate.net/profile/Ann-Kathrin_Kniggendorf/

Acknowledgments

The number of people deserving acknowledgment at the end of such a long work is sheer overwhelming. With respect to limited time and space, I would like to specially acknowledge

Dr. Merve Meinhardt-Wollweber
We’ve come a long way since that initial „Willst Du das bauen?“, haven’t we?

Dipl.-Biol. Tobias Gaul
for answering my question about detonating Anammox.

Prof. Uwe Morgner
for „adopting“ me and my project.

Prof. Angelika Anders-von Ahlften†
who believed in me, even when I did not.

Elizabeth Bales-Stutes and Sonja Cameron
for hyphenation, a neuron, and a place in the cold.

my mother and grandmother
Doris Menneking and Franziska Marie Luise Reuter
fürs Träumen und Fliegen und dafür, dass sie noch da sind, um zu sehen was dabei herausgekommen ist!

Sincere thanks are given to all the people at the Institute of Biophysics and across the world, who made the last years an incredible experience. I wish there were twenty more pages to list you all.

...und nach nunmehr 36 Jahren,
Prof. Menger, Sie haben recht.
Danke schön.